Enhancement of Photoinduced Processes on Supported Ag Nanoparticles Compared to a Flat Ag Surface

Im Fachbereich Physik der
Freien Universität Berlin
eingereichte Dissertation

M.S. Ki Hyun Kim

March 2009

This work was done between March 2005 and March 2009 in the group of Professor Hans-Joachim Freund at the Chemical Physics Department of the Fritz-Haber-Institut der Max-Planck-Gesellschaft.

Berlin, in March 2009

1st referee:	Prof. Dr. Hans-Joachim Freund Fritz-Haber-Institut der Max-Planck-Gesellschaft
2nd referee:	Prof. Dr. Martin Wolf Freie Universität Berlin Fritz-Haber-Institut der Max-Planck-Gesellschaft

Day of defense: May 4, 2009

Abstract

Thermal and photoinduced processes on Ag(111) and supported Ag nanoparticles (NPs) are investigated by temperature programmed desorption (TPD), mass-selected photoinduced desorption (PID) and time-of-flight (TOF) measurements by using nano- and femto-second laser pulses. The Ag NPs were formed by depositing Ag atoms from an electron beam evaporator on an Al_2O_3/NiAl(110) substrate.

The photoreactivities and photodesorption dynamics of individual NO species are investigated selectively by controlling their adsorption states. Interestingly, the direct photochemical formation of N_2 with a very high translational temperature has been observed for the first time as a result of strong repulsion by the surface upon its formation as well as N_2O in photoreactions of NO dimers on Ag(111) induced by irradiating photon energy $\geq$ 2.3 eV. To elucidate the formation mechanism of N_2, the incident angle and polarization dependences as well as the photon energy dependence of N_2O on Ag(111) have been investigated. However, N_2O on Ag(111) shows its own peculiar photodesorption dynamics. These results lead us to propose that the N_2 forms via simultaneous cleavage of the two N-O bonds followed by the formation of an N-N triple bond of N_2, and can be regarded as mutual abstraction of the N atom from each nitrosyl in $(NO)_2$ on Ag(111).

The thermal- and photoreactions of NO on Ag NPs are compared to those on Ag(111) by means of the same experimental setup and procedures adopted in the study of NO on Ag(111). The nanosecond laser irradiation shows that the photodesorption yield of NO on supported Ag NPs are enhanced off plasmon resonance as well as at on plasmon resonance of the (1,0) mode. The photodesorption yield from Ag NPs is further dramatically enhanced by the femtosecond laser irradiation whereas that from Ag(111) is almost unchanged. The overall enhancements are dealt with confinement effect, plasmon excitation, and desorption models by calculating the number of hot electrons and desorbates.

The unique photodesorption of Xe with hyperthermal energy and chaotic time structure is observed from Xe monolayers on the Ag NPs by the nanosecond laser pulses in the (1,0) Mie plasmon resonance. The chaotic behavior is most likely due to coupling between the plasmon fields of suitably distributed AgNPs. To explain the results, it is argued that the desorption is induced by direct energy transfer to the adsorbate from the Pauli repulsion of the collectively oscillating electrons of the plasmon at the surface. A simple model calculation shows that this is possible.

Abbreviations

2PPE	Two photon photoemission
3D	3 dimensional
AES	Auger spectrometer
BBO	Beta Barium Borate
CFD	Constant Fraction Discriminator
DIET	Desorption (or more generally dynamics) induced by electronic transitions
DIMET	Desorption (or more generally dynamics) induced by multiple electronic transitions
E_a	Affinity level
e-e	Electron-electron
e-h	Electron-hole
FID	Femtosecond laser induced desorption
fs	Femtosecond
HOMO	Highest occupied molecular orbital
HREELS	High Resolution Electron Energy Loss Spectroscopy
IR	Infrared
LEED	Low energy electron diffraction
LIF	Laser-induced fluorescence
LITD	Laser-induced thermal desorption
LUMO	Lowest unoccupied molecular orbital
MC	Metal cluster
MCS	Multichannel scaler
MGR	Menzel-Gomer-Redhead
ML	Monolayer
MNP	Metal nanoparticle
N_e	The number of hot electrons per nanoparticle per laser shot
NID	Nanosecond laser induced desorption
N_m	The number of desorbed or rather the removed NO dimers per nanoparticle per laser shot
NO-α	NO from NO dimers
NO-β	NO from NO monomers
NP	Nanoparticle

N_{ph}	The number of photons
ns	Nanosecond
PCS	Photodepletion cross section
PES	Potential energy surface
PID	Photoinduced desorption
PMT	Photomultiply tube
QMS	Quadrupole mass spectrometer
REMPI	Resonance-enhanced multiphoton ionization
SEM	Secondary electron multiplier
SERS	Surface enhanced Raman spectroscopy
SFG	Sum frequency generation
STM	Scanning tunneling microscopy
T_{el}	Electronic temperature
TNI	Transient negative ions
TOF	Time-of-flight
TPD	Temperature programmed desorption
T_{ph}	Phonon temperature
T_t	Translational temperature
UHV	Ultra high vacuum
UV	Ultraviolet
vdW	Van der Waals
XPS	X-ray photoelectron spectroscopy

Table of Contents

Chapter 1. Introduction

1.1. Motivation

Photoinduced processes of molecules on solid surfaces have long been actively investigated due to not only fundamental interest in physics and chemistry but also their vast application potential in industry [1, 2]. Irradiation of photons brings sudden electronic transitions of adsorbates, so called Frank-Condon transitions, from the ground state potential energy surface (PES) to the excited state PES. Since the excited PES is generally very different from the ground state PES, the adsorbates undergo strong distortion on the excited PES and then are deexcited to the ground state PES after a lifetime. This is a unique process in photoreactions, thus, it may open new reaction channels which are not accessible by thermal reactions.

One immediately realizes that surfaces are very important in the electronic transitions of adsorbates. The surface not only modifies the electronic structure of the adsorbate but also offers electrons to the adsorbate if it is metal. This suggests that we can control and enhance surface photoreactions by adopting proper surfaces. Therefore, photoreactions on well-defined solid surfaces have been investigated extensively [2-9].

Recently, clusters (diameter $d < 1$ nm) or nanoparticles (NPs, $1 \leq d \leq 100$ nm) fabrication techniques have been developed aggressively [10-12]. Clusters are an intermediate state of matter between atomic or molecular structure and corresponding bulk material, which often show, however, significantly modified physical and chemical properties which are size dependent [1, 13-16]. Therefore a very intriguing question is how photochemistry of molecules adsorbed on metal clusters/NPs are modified by their unique electronic/geometric properties compared to bulk metal surfaces. However, there have been only few studies that address those questions so far.

In the last two decades, the technique to fabricate and characterize metal clusters (MCs) or metal nanoparticles (MNPs) supported on solid surfaces have been developed and established. In these systems, surface analytical methods such as XPS (X-ray photoelectron spectroscopy) [17] and STM (scanning tunneling microscopy) [18, 19]

under ultra high vacuum (UHV) conditions can be employed. Especially, well-defined MCs and MNPs grown on inert substrates such as thin oxide films have been utilized as model systems of real catalysts. Such model systems are also very suitable for the study of photochemistry on the surfaces of MNPs; one can benefit from the full capability of surface analytic methods and compare photochemistry as well as adsorption states of adsorbates between MNPs and bulk metals.

Furthermore, the use of supporting thin dielectric layers such as alumina has several advantages in photochemistry. They are transparent in visible and ultraviolet (UV) ranges, but the transport of hot electrons through the layer is strongly suppressed, though tunneling of electron is still possible. Thus the MNPs supported on a thin oxide layer can be electronically decoupled from the underlying metal substrate, whereas the energy exchange by phonons are still efficient. This means the decay of electronic excitations within the MNP can be significantly suppressed. Since the interaction of the nonthermal and thermalized electrons to the adsorbate induces exclusively photochemistry on metal surfaces [2], the elongation of lifetimes of hot electrons in the MNPs can result in enhancement of photoreaction cross sections.

The optical properties of MCs and MNPs play a crucial role in photochemistry. Above all, excitation of the Mie plasmon, the collective motion of free electrons in MNPs can enhance the electric field near the surface. Plasmon have been addressed for various MNPs [20], and their spectral resonance positions are strongly influenced by their size [18, 21], shape [22-25], dielectric surrounding, structure, and composition of the NPs [26]. In the presence of surface plasmon excitations which do not exist in bulk metal, overall photoexcitation of the MNP is enhanced by the increased surface electric field. The plasmons decay via dephasing and Landau damping into electron-hole pairs increasing non-thermal electrons, radiation damping into photons, and scattering by adsorbates (Chemical interface damping, CID). The plasmons can couple among the MNPs, which may lead to collective nonlinear response of the MNPs system [27-30].

The peculiar electronic and optical properties of MNPs mentioned above suggest that photoinduced processes of molecules on MNPs are very different from those on corresponding bulk material. Therefore, this thesis is intended to compare photoinduced processes of molecules on Ag(111) and Ag NPs grown on an Al_2O_3/NiAl(110) substrate. Ag NP is good candidate for the study of surface plasmon effects because the interband transition from the fully occupied d-bands below the Fermi energy to the *s-p* band in Ag is near 4 eV, which is well above the surface plasmon resonance of Ag [31]. Also, the thin alumina oxide film on NiAl(110) has several advantages as a support. It can be easily prepared with good reproducibility, and its structure and related properties such as defect density are well documented [14]. Furthermore, it is chemically inert [32], which enables the study of pure interactions between adsorbed molecules and MNPs supported on its surface.

We have chosen three kinds of reactants, namely, NO, N_2O and Xe. NO is the prototypical molecule in the studies of surface photochemistry, for which state-resolved methods such as LIF (laser-induced fluorescence) [33] and REMPI (resonance-enhanced multiphoton ionization) [34, 35] can be applied to study desorption dynamics. Photoreactions of N_2O on Ag(111) were investigated in this thesis work because it is one of the products and intermediates of photo/thermal reactions of NO, and its photoreactions had to be studied separately from those of NO. Xe is one of the rare gases and chemically inert. It is sensitive to the local change of the electronic states on metal surfaces as demonstrated in PAX (photoelectronspectroscopy of adsorbed xenon) [36], for example.

The structure of the present thesis is the following. After the motivation of the studies, properties of Ag NPs on Al_2O_3/NiAl(111) surfaces and photoinduced processes related to photoreactions on their surfaces are summarized in the Introduction. In Chapter 2, the experimental methods and the procedures of data analyses used commonly in this thesis work are described. The early part of Chapter 3 deals with the studies of adsorption states and photochemistry of NO dimers and monomers on Ag(111) using mass selected time-of-flight (TOF) and temperature programmed desorption (TPD) measurements. The direct photochemical formation of N_2 from NO dimers is also discussed. In the later part, results of N_2O on Ag(111) by using the same methods will be presented, which are supplemental to elucidate the formation mechanism of N_2 from NO dimers on Ag(111). Also, measurements of incident angle and polarization dependences as well as photon energy dependence are detected. However, N_2O on Ag(111) also shows its own peculiar photodesorption dynamics. Based on the results from the NO on Ag(111) system, Chapter 4 presents photoreactions on NO on Ag NPs. Especially, the effects of the Mie plasmon of Ag NPs on photoreactions of NO will be contrasted by comparing with the results from Ag(111) surfaces without plasmon excitation. In Chapter 5, the effects of excitation by femtosecond laser pulses are compared between Ag NPs and Ag(111). Very exotic phenomena, hyperthermal and chaotic photodesorption of Xe from Ag NPs where plasmon excitations play a major role, are presented in Chapter 6. Finally, In Chapter 7 the results are summaried and the conclusions of this thesis are given.

1.2. Properties of nanoparticles

Any change in the geometric and electronic properties of MNPs from bulk metals may lead to changes in surface photochemistry. Adsorption states of molecules will be influenced by these factors, and this will modify photochemical processes. These situations have been thoroughly discussed in ref [1]. Here we focus on the electronic and optical properties of MNPs, which decisively distinguishe photochemistry on MNPs from that on bulk metal surfaces.

1.2.1. Electronic properties

The electronic structure and the electron dynamics of MNPs have considerable implications for their photochemical performance especially in the case where chemical reactions are initiated by electrons from MNPs. Here we discuss how they evolve with particle size.

Fig. 1.1 shows the change in the energy levels from a single atom to a bulk metal [1, 14]. The gradual development of metallic bands from single atomic orbitals is observed in the valance band region with increasing particle size [37]. The metallic properties appear at about 1 nm and a bulk-like band structure is formed at ~ 3 nm in diameter [38]. The average size of the Ag NPs used in the present thesis was set above 3 nm, thus the bulk-like band structure can be assumed.

Thanks to the presence of the thin alumina film, which is an insulator, the Ag NPs can be regarded as being electronically decoupled from the NiAl(110) substrate in a static picture. However, charge transport through the film is possible by tunneling, which prevents permanent charging of the NP. Electrons in the metal substrate will affect those in the supported NPs dynamically via image charge interactions, especially when they interact with electromagnetic waves. This will be mentioned in the subsequent section.

The dynamics of the hot carriers (electrons/holes) photogenerated in the MNPs can excite adsorbates, leading to chemical reactions. This is of central importance in photochemistry on MNPs. The time sequence of the elementary processes can be classified into 4 steps [1].

1: Absorption of a photon by a MNP and creation of an electron-hole (e-h) pair.

2: Development of athermal e-h distribution by electron-electron (e-e) scattering (within tens of femtoseconds)

3: Thermalization of electrons and establishment of electronic temperature (some 100 fs to 1 ps)

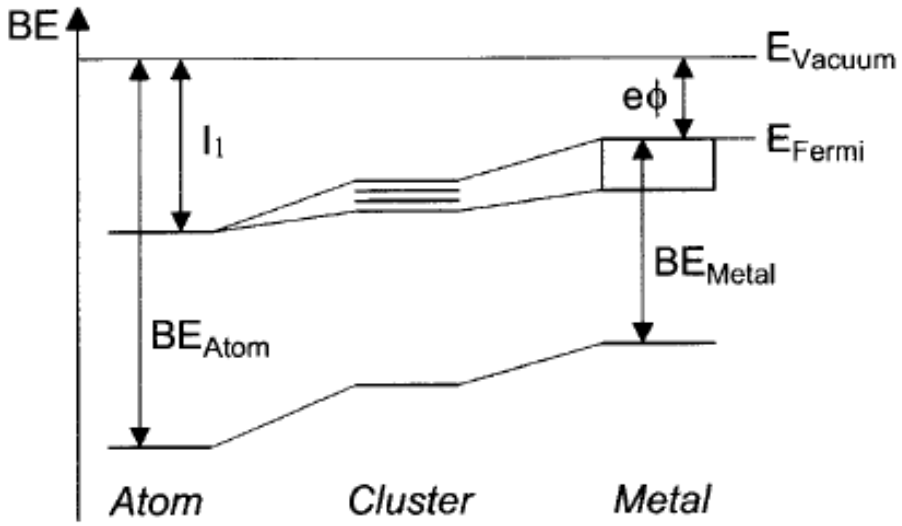

Fig. 1.1. Diagram illustrating the evolution of electronic states from a single atom to a metal (BE: binding energy; I_1: first ionization energy; e: electron charge; φ: work function). Reprinted from ref. [14], Copyright (1999), with permission from Elsevier.

4: Cooling of electronic temperature by electron-phonon interactions (several to some hundred picoseconds)

In contrast to extended bulk metals, the confinement within the MNPs can influence e-e scattering. First, the confinement of electrons could act positively on e-e scattering, since the wave functions of the hot electrons should become standing wave states. Second, e-e scattering can be increased by reduced screening at the surface of the MNP. These aspects may strongly affect the relaxation of hot electrons. Needless to say, such electron dynamics are decisive for hot electron-driven surface photochemistry.

The particle size effects on the electron dynamics have been discussed previously [1]. The electron thermalization time will decrease with decreasing particle size, i.e., with increasing the surface to volume ratio. This is due to the reduction of Coulombic screening of *sp* electrons spilling out to the vacuum by *d* electrons localized inside the MNP [39] especially of noble metals [18, 39, 40]. This aspect becomes significant for a particle size ≤ 5 nm [39].

1.2.2. Optical properties

Optical properties of MNPs are of primary importance concerning photochemistry on their surfaces. For MNPs of noble metal (Cu, Ag, Au) and alkali metal (Na, K, etc.), their

optical spectra are dominated by pronounced resonant features induced by surface plasmon excitation. A plasmon is the collective oscillation of free electrons in a conduction band against the positive ion cores. The plasmon itself is sometimes considered as a quasiparticle. The surface plasmon is the plasmon which is confined at the surface and interacts strongly with light.

The optical properties induced by plasmon excitation can be derived directly from Maxwell's equations. The analytical solution of Maxwell's equation for the scattering of electromagnetic radiation by spherical boundary conditions was derived by Gustav Mie in 1908 to explain the color of stained glass and solutions of metal colloids. If the particle size is much smaller than the incident light wavelength, the so called quasi-static regime, the incident electro-magnetic field is spatially uniform over the particle. Thus, retardation effects are neglected. In this regime, the resonance frequency ω_s for a sphere and ω_e for a ellipsoid are

$$\omega_s = \frac{\omega_p}{\sqrt{3}}, \ \omega_p = \sqrt{\frac{ne^2}{\varepsilon_0 m_e}} \tag{1.1}$$

$$\omega_e = \omega_p L_m \tag{1.2}$$

where n denotes the electron density, m_e the electron mass, and L_m the geometrical depolarization factors.

The plasmon mode is expressed by (L, m), where L denotes the multipole order, *i.e.* a dipole mode for L = 1, quadrupole mode for L = 2, octupole mode for L = 3, and so on.

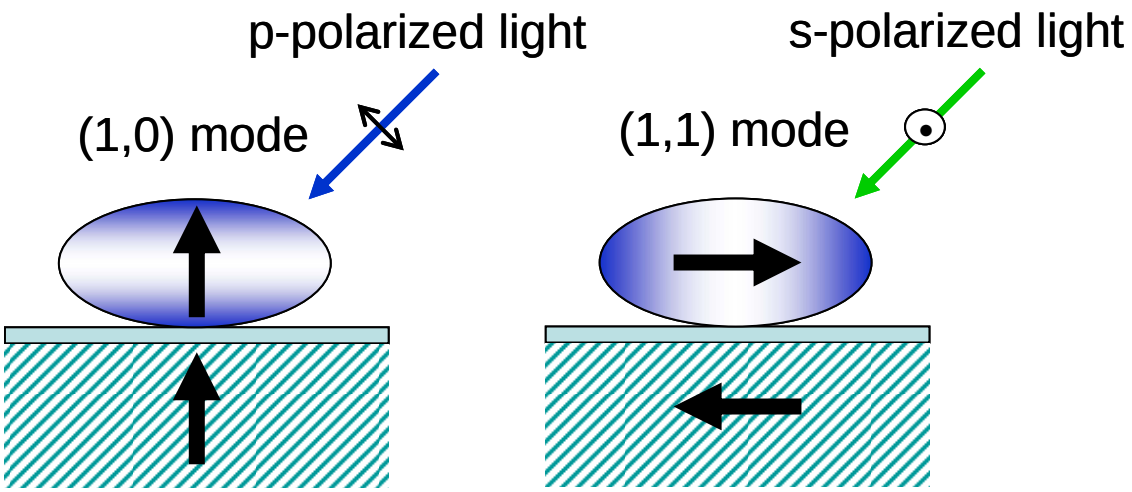

Fig. 1.2. Schematic representation of the surface plasmon excitation for oblate ellipsoidal NP/ Al_2O_3/ NiAl(110). Left: (1,0) mode excited by p-polarized light. Free electrons in the NP oscillate along the short axis. Image dipole in the NiAl superposes constructively. Right: (1,1) mode excited by s-polarized light. Free electrons in the NP oscillate along the long axis. Image dipole in the NiAl superimposes destructively.

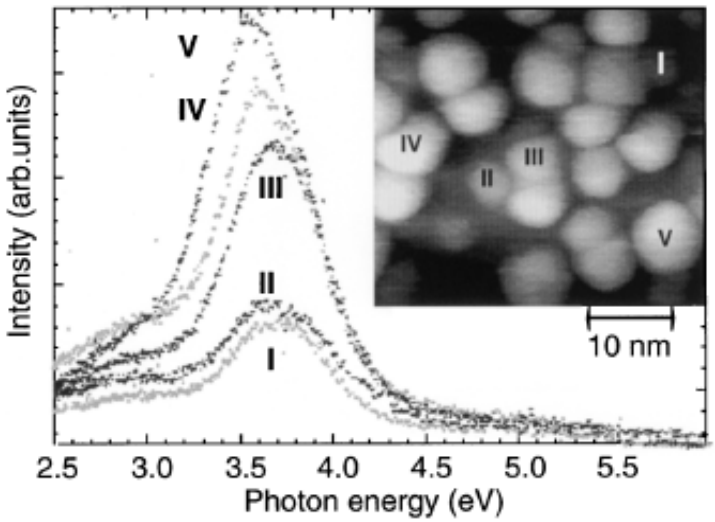

Fig. 1.3. Photon emission spectra of differently sized Ag NPs (accumulation time 500 s, U_{tip} = -10 V, I_{gap} = 10 nA). The inset shows the corresponding STM image. Reprinted with permission from ref. [18]. Copyright 2000 by the American Physical Society.

There are L+1 eigenmodes, m, for each L. For oblate ellipsoidal particles which are typical for supported particles the resonance splits into two modes, the (1,0) mode along the short axis and the (1,1) modes along the long axes. Fig. 1.2 presents two plasmon modes for a NP supported on Al_2O_3/NiAl(110). The orientation of the (1,0) mode dipole and induced image dipole in the substrate is collinear, and they superimpose constructively, whereas the (1,1) mode plasmon excitation is weakened by the induced image dipole.

Fig. 1.3 shows photon emission spectra from Ag NPs of different sizes deposited on a thin Al_2O_3 film on NiAl(110) excited by electron injection through a STM tip. The inset shows the STM image for corresponding Ag NPs. A clear resonant peak was observed around 3.6 eV in all the spectra. This peak corresponds to the resonant excitation of the (1,0) mode of the Mie plasmon of the Ag NPs. The peak intensity becomes stronger with increasing Ag NP size because the number of electrons in the NPs is increased. The red shift of the peak position with increasing the size can be explained in terms of Mie theory. Similar resonant features have also been observed by 2PPE measurement [41].

In the present thesis work, the same recipe as used for the experiments shown in Fig. 1.3 has been employed for the preparation of the Ag NPs. Thus, it can be assumed that the Ag NPs used in the thesis work had similar optical properties as shown Fig. 1.3.

1.3. Excitation mechanisms

Photon irradiation of adsorbates on surfaces opens up at least three different pathways: (1) adsorbate localized excitation (often called direct excitation): direct electronic excitation localized in the adsorbate or photoexcitation of the adsorbate-substrate bond by absorbing photons; (2) substrate mediated excitation (often called indirect excitation): the photon is absorbed by the substrate, resulting in electron-hole pair creation. The created hot electrons or holes are then transferred to an adsorbed molecule to form a transient negative ion state or transient positive ion state that undergoes photochemical processes; (3) thermal reaction: relaxation of the initial excitation energy results in surface heating, leading to surface reactions.

Generally, the reactions induced by an adsorbate localized excitation or a substrate mediated excitation before energy thermalization are considered as photochemical mechanisms. In this study, laser irradiance was kept below ~ 2 mJ/cm^2/shot, for which renders thermal reaction negligible. Therefore, an overview of non-thermal photochemical processes will be presented in this section.

1.3.1. Adsorbate localized excitation (direct excitation)

If photochemistry on the surface is initiated by direct electronic excitation from an occupied electronic state to an unoccupied state, which is localized in the adsorbate, such as $Mo(CO)_6$ on graphite and Ag(111) [42], CO on Pt(001) [43], Methane on Pt(111) [44], it is called adsorbate localized excitation or direct excitation, as illustrated in Fig. 1.4. This excitation is qualitatively similar to the excitation of isolated molecules. The geometric and electronic structure of molecules adsorbed on the surface are, however, different from those in the gas phase due to interaction with the surface and reduced symmetry, e.g., broadening and shifts in the energetic

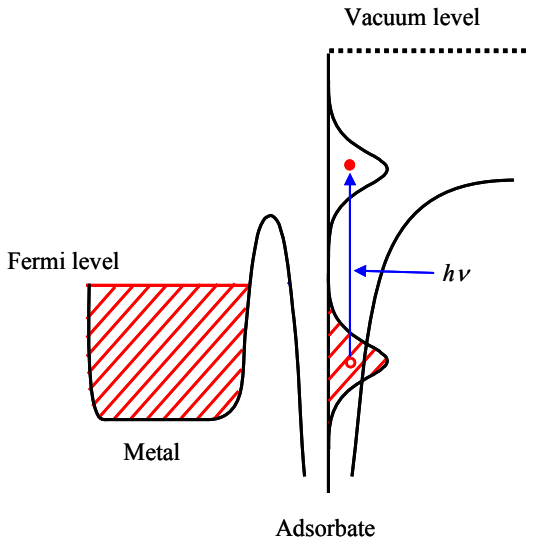

Fig. 1.4. Adsorbate localized excitation or direct excitation. Photoexcitation takes place within the adsorbate substrate complex. Adopted from ref. [45].

position of the molecular orbital, and reduced degeneracy. Therefore, the direct excitation mechanism is conceivable, even though excitation of molecules in the gas phase would be inaccessible with a given photon energy.

For laser power densities < 10^{10} W/cm^2, the transition rate between the initial (φ_i) and final state (φ_f) is given by Fermi's Golden rule [8, 46]:

$$\Gamma_{if} = (\pi e / imh\nu)\left|\langle \varphi_f | E \cdot \mu | \varphi_i \rangle\right|^2 \delta(\Delta E_{if} - h\nu) \tag{1.3}$$

where E is the electric field vector, μ the electronic transition dipole moment vector, ΔE_{if} the energy difference between the initial and final states, $h\nu$ the photon energy, e and m are the elementary charge and mass, respectively.

If only the adsorbate localized excitation is involved in a photoreaction, the cross section is scaled as

$$\sigma_j \sim \left|\langle E \cdot \mu \rangle\right|^2 \tag{1.4}$$

where j denotes polarization. A schematic diagram of the geometry during optical excitations and the orientation of dipole moment of the electronic transition μ is illustrated in Fig. 1.5.

In the calculation of equation (1.4), the mixed term, $< E_x \cdot E_z >$, can be solved by considering rotational symmetry. It can be assumed that transition dipoles of the adsorbate or the adsorbate-substrate complex are not distributed isotropically, but rather

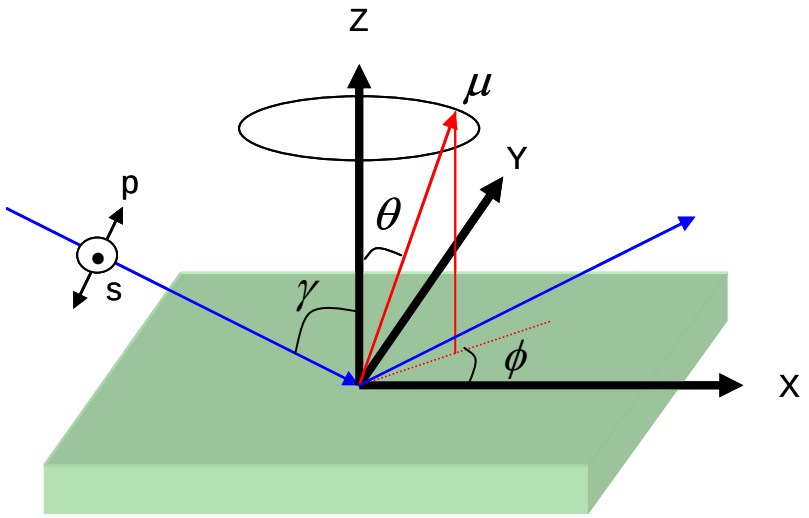

Fig. 1.5. Schematic drawing of incident light and the orientation of the transition dipole moment μ at the surface.

oriented to give the same or higher rotational symmetry. For surfaces with ≥ C_3 rotational symmetry, e.g., fcc(111) and fcc(100) surfaces, the cross sections are given by [44, 46]

$$\sigma_p \sim (0.5\sin^2\theta < E_x^2 > + \cos^2\theta < E_z^2 >)/\cos\gamma \quad (1.5)$$

$$\sigma_s \sim (0.5\sin^2\theta < E_y^2 >)/\cos\gamma \quad (1.6)$$

where θ is the angle of the transition dipole moment with respect to the surface normal, $0^o \leq \theta \leq 180^o$ and γ is the incident angle of light.

In the case of a surface with ≥ C_2 rotational symmetry, e.g., the fcc(110) surface, the cross sections are given by

$$\sigma_p \sim (\cos^2\phi\sin^2\theta < E_x^2 > + \cos^2\theta < E_z^2 >)/\cos\gamma \quad (1.7)$$

$$\sigma_s \sim (\sin^2\phi\sin^2\theta < E_y^2 >)/\cos\gamma \quad (1.8)$$

where ϕ is the azimuthal angle, $0^o \leq \phi \leq 180^o$. The factor of $1/\cos\gamma$ is included to compare the experimental data normalized to the intercepted irradiance at the surface [44, 47]. Fig. 1.6 displays the calculated surface electric field strengths and substrate absorbance as a function of incident light angle on Ag at 4.7 eV. A_p and A_s denote the absorbance for *p*- and *s*-polarization, respectively. The curves are calculated from Fresnel's equations with the optical constants for Ag tabulated in ref. [48]. In the case of *s*-polarized light, the electric field has only a E_y component. The A_s and

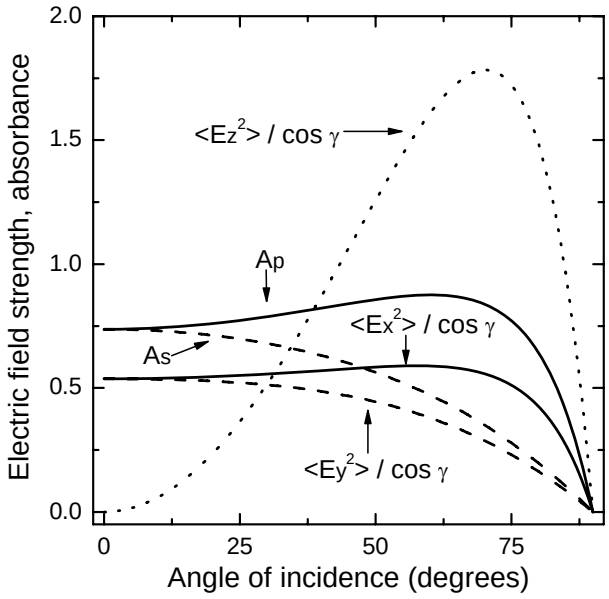

Fig. 1.6. Angular dependence of the electric field strengths and substrate absorbance for *p*- and *s*-polarized light, A_p and A_s, respectively, on Ag at 4.7 eV. The results are calculated from Fresnel's equations and Ag optical constants.

$< E_y^2 > / \cos\gamma$ decrease monotonically to zero with increasing angle of incidence, whereas *p*-polarized light has two components, E_x and E_z. A_p has the same value as A_s at normal incidence, rises slowly to 60°, and then decreases to zero. $< E_x^2 > / \cos\gamma$ decreases monotonically to zero, whereas $< E_z^2 > / \cos\gamma$ starts from zero at normal incidence, maximizes at 70°, and declines towards zero rapidly. The differences illustrated in Fig. 1.6 can be used to distinguish excitation mechanisms. For substrate mediated excitation, the photoreaction cross section scales with the absorbance of the substrate. In contrast, the photoreaction cross section in the case of adsorbate localized excitation should be proportional to the electric field intensity.

Fig. 1.7 plots photoexcitation cross sections for the transition dipole moments with θ = 0°, 30°, and 60° on Ag at 4.7 eV as a function of the incidence angle. Equations (1.5) and (1.6) were used for the calculations. The rise of the curve with increasing angle of incidence becomes more obvious for smaller θ.

Comparison of measured angle- and polarization dependences of the photoreaction cross section with calculated surface electric field strength and surface light absorbance can be used to determine the photoexcitation mechanism, if the transition dipole moment has a component perpendicular to the surface, i.e., along the Z-direction. When θ is close to 90°, the calculated cross section is indistinguishable from that for the surface absorbance.

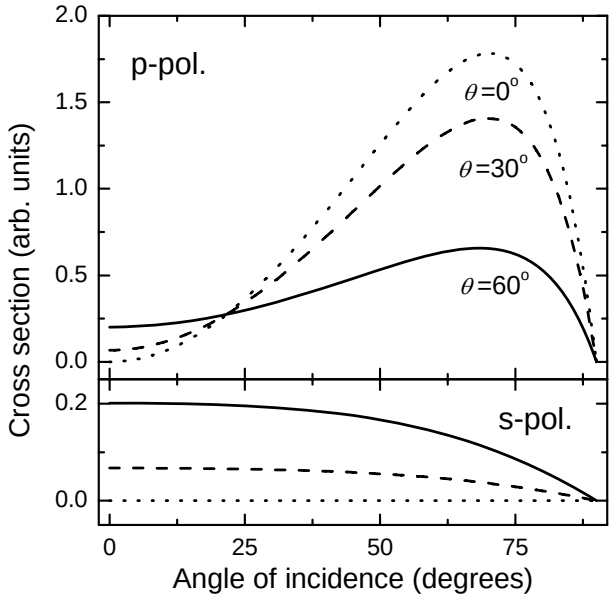

Fig. 1.7. Incident angle dependence of cross sections in adsorbate localized excitation on Ag at 4.7 eV for *p*- (upper) and *s*-polarized (lower panel) light. The curves are calculated from equations (1.5) and (1.6) using μ = 0°, 30°, and 60°.

1.3.2. Substrate mediated excitation (indirect excitation)

When photochemistry is mediated by hot carriers at a surface, such as NO on Ag(111) [49] or Pt surfaces [50-53] and O_2 on Pd(111) [54, 55], it is called substrate mediated excitation or indirect excitation. The excitation process at a metal surface is shown in Fig. 1.8. The first step in the substrate mediated excitation is electron-hole pair creation by photon absorption within the substrate. The second step is propagation of the generated hot carriers to the surface, and the third step is tunneling of the generated hot carriers through the surface potential barrier to resonant states of the adsorbate. The photoreaction cross section, therefore, strongly depends on the hot carrier dynamics. The longer the life time of the hot carriers involved in the photoreaction, the higher the photoreaction cross section, because the rate of charge transfer to the adsorbate increases. Since an understanding of the hot carrier dynamics is essential in photoreactions on the surface when substrate mediated excitation is the active mechanism, femtosecond time resolved 2PPE and pump-probe measurements have been intensively employed to observe the hot carrier relaxation dynamics [56-59].

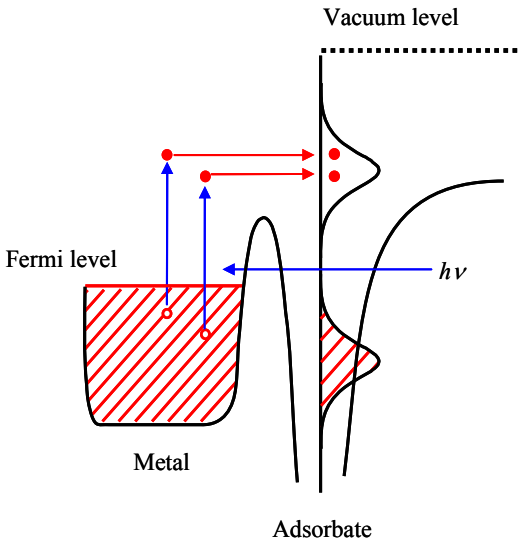

Fig. 1.8. Substrate mediated excitation. Photochemistry is mediated by hot carriers at the surface. Adopted from ref. [45].

If only the substrate mediated excitation is involved in the photoreaction, the cross section is determined by the number of hot carriers reaching the surface. The absorption of the substrate is proportional to $(1-R(\lambda))$, where $R(\lambda)$ is the polarization and wavelength dependent reflectivity of the substrate. The ratio of produced hot carriers from the surface to the distance z is

$$A \sim \int_0^z e^{-\alpha(\lambda)z} dz \tag{1.9}$$

where the wavelength dependent absorption coefficient is [60]

$$\alpha(\lambda) = \frac{8\pi^2}{\lambda^2}\left\{\left[\left(\kappa^2 + \sin^2\gamma - n^2\right)^2 + 4\kappa^2 n^2\right]^{1/2} + \left(\kappa^2 + \sin^2\gamma - n^2\right)^2\right\} \tag{1.10}$$

and the complex dielectric constant ε is related to the refractive index n and the extinction coefficient κ by $\sqrt{\varepsilon} = n + i\kappa$.

Since only the hot carriers reaching the surface are expected to participate in the photoexcitation, the ratio of the effective number of the hot carriers is $\left(1 - e^{-\alpha(\lambda)\Lambda}\right)$, where Λ is the mean free path of the carriers. Thus, the wavelength dependent effective absorbance is given by [8, 61, 62]

$$\sigma^{eff.} \sim (1 - R(\lambda))(1 - e^{-\alpha(\lambda)\Lambda}) \tag{1.11}$$

Fig. 1.9 displays the dependences of the absorbance and absorption coefficient on the incident light wavelength for *p*- and *s*-polarization. The refractive index n and extinction coefficient κ is from ref. [48] at 45° incidence angle. A_p and A_s are the absorbance of Ag for *p*- and *s*-polarized light, respectively. $A_p^{eff.}$ and $A_s^{eff.}$ are the effective absorbances at Λ = 10 nm for *p*- and *s*-polarization, respectively. The absorption coefficient $\alpha(\lambda)$ is calculated from equation (1.11). A_p and A_s rapidly increase and are maximized at ~ 4 eV, whereas $\alpha(\lambda)$ steeply decreases and is minimized at ~ 4 eV.

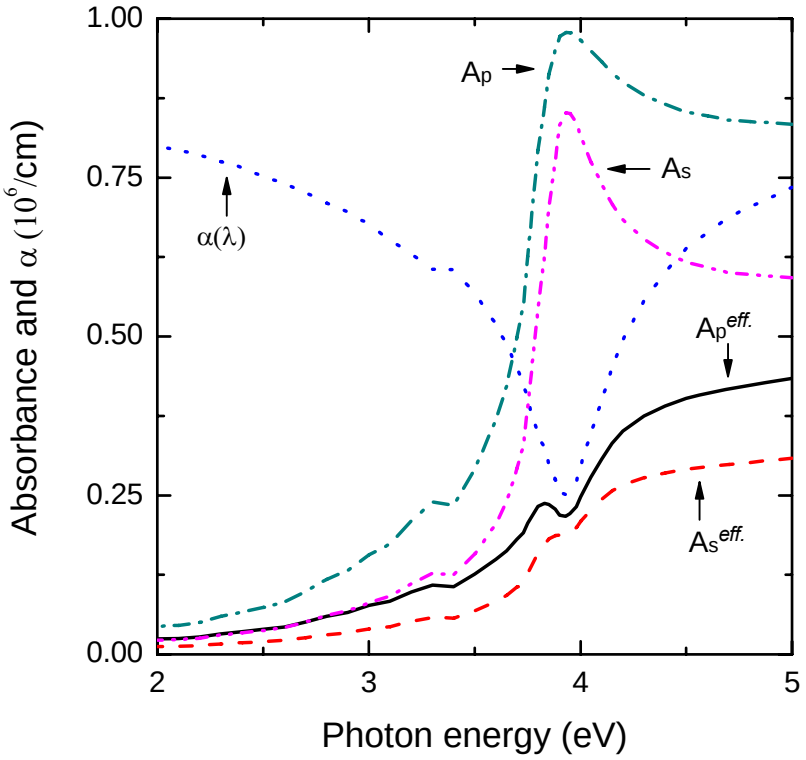

Fig. 1.9. The incident photon energy dependences of absorbance and absorption coefficient for *p*- and *s*-polarization.

1.4. Photodesorption Mechanisms

1.4.1. Photodesorption in the linear regime

Photodesorption has been widely explained by the Menzel-Gomer-Redhead (MGR) model [4, 63] proposed in 1964. A schematic of the MGR model for desorption induced by electronic transitions (DIET) is represented in Fig. 1.10. The important constituents in this model are a ground state PES, a Frank-Condon type electronic transition, and an excited state PES. The ground state PES is determined by an adsorption state on the surface, which is influenced by several conditions such as adsorption sites, adsorption structures, coverage, etc. The absorbed photon transfers the adsorbate via a Frank-Condon type electronic transition from the ground state PES to the excited state PES, which is repulsive in the MGR model. Since the excited state PES depends on the nature of the excited state, e.g., the excitation level of intermolecule or adsorbate-substrate, electron or hole attachment, and so forth, the motion of the molecule on the excited PES depends on the excitation processes. During residence time on the excited state PES, the adsorbate is accelerated and gains kinetic energy E_k'. After quenching to the ground state PES, it has gained potential energy, since the position of the adsorbate with respect to the surface is different from the situation before excitation due to the motion of nuclei on the excited state PES [2]. If the sum of the gained potential and kinetic energies in the reaction coordinate are sufficient to overcome the desorption barrier E_b, the adsorbate desorbs with kinetic energy E_k. As a result, different adsorption states and excitation processes are reflected by different translational temperatures ($T_t = \langle E_k \rangle / 2k_B$) and photodesorption cross sections. Although the MGR model was developed to describe desorption of adsorbates, it can be generally used for photoinduced dynamics by choosing the appropriate reaction coordinate.

A similar scenario of photodesorption, in which an ionic excited state of the adsorbate is involved, was proposed by Antoniewicz in 1980 [9]. The Antoniewicz model created in Fig. 1.11 describes the transient negative (positive) ion state on the excited PES by electron (hole) transfer from the metal substrate to the adsorbate. Therefore, in contrast to the MGR model, the excited state PES is attractive due to the image potential by the metal substrate. In the transient negative (positive) ion state of adsorbate, the adsorbate is accelerated to the surface and gains kinetic energy E_k'. After a residence time on the excited state PES, the electron (hole) attached to the adsorbate hops back into the metal substrate, and the adsorbate experiences a repulsive force due to a different adsorbate-surface distance. Similar to the MGR model, when the sum of gained potential

and kinetic energies in the reaction coordinate are sufficient to overcome the desorption barrier E_b, desorption occurs with kinetic energy E_k.

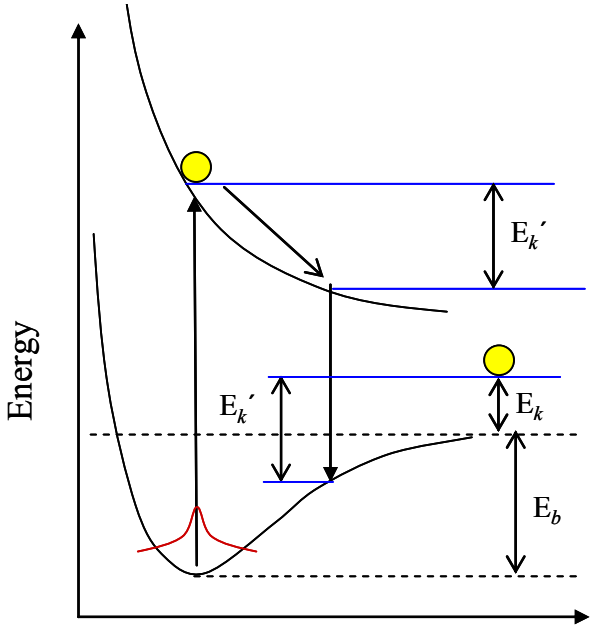

Fig. 1.10. Schematic drawing of MGR model. The excited state PES is repulsive.

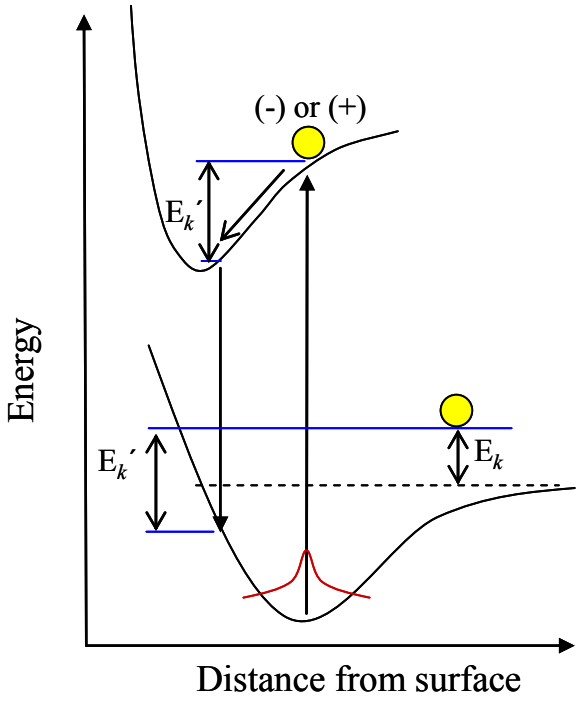

Fig. 1.11. Schematic drawing of Antoniewicz model. The excited state PES is attractive due to image charge on the metal substrate.

1.4.2. Photodesorption in the nonlinear regime (Femtosecond laser excitation)

Femtosecond (fs) laser irradiation can create many hot electrons in a short time, opening up new desorption channels. The most peculiar features in fs laser induced desorption (FID) are as following: (1) highly enhanced photodesorption yield; (2) laser fluence dependence of photodesorption yield, T_l, and branching ratio; (3) high vibrational excitation of desorbates [64-67]. To quantitatively describe FID dynamics, two conceptually different models have been proposed. First, the desorption induced by multiple electronic transitions (DIMET) [68, 69] process is illustrated in Fig. 1.12 (a). The adsorbate which gained insufficient energy to overcome a potential barrier is vibrationally excited after a single DIET process. If that adsorbate is excited several times, however, before adsorbate-surface vibrational energy relaxation, the desorption probability will be significantly increased. This model is generally applied for high lying adsorbate resonance states from the Fermi level.

The other approach, the so called friction model, is illustrated in Fig. 1.12 (b). It is rationalized in terms of electronic frictional coupling between an adsorbate and thermalized substrate hot electrons [70-72]. This frictional coupling has been proposed as a mechanism for excitation of intramolecular vibration in low energy scattering of adsorbates from substrate hot electrons [73-75] and further extended for coupling to the adsorbate center of mass degree of freedom, leading to a desorption mechanism [76]. The adsorbate resonance is broad near the surface due to strong interaction with the substrate. Thus, once the adsorbate is vibrationally excited, the adsorbate resonance is shifted and intrinsically affected by damping. In contrast to the DIMET model, the Friction model is

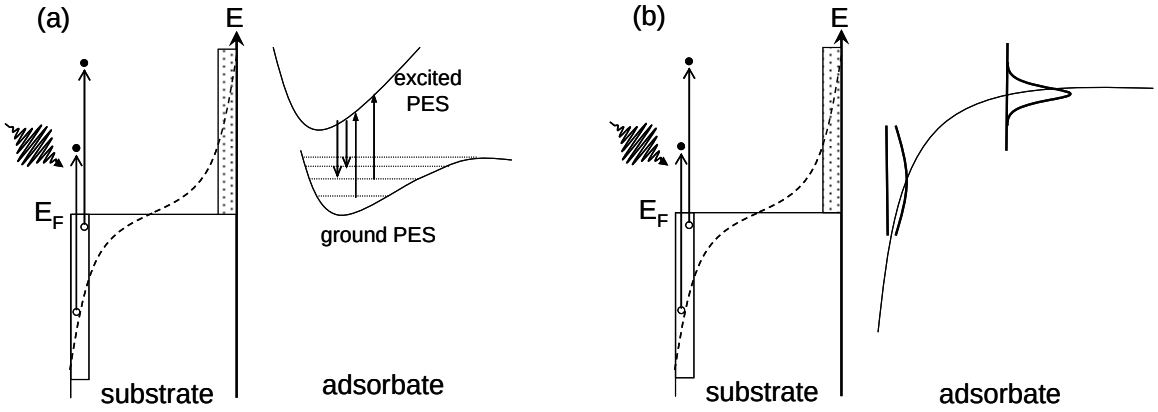

Fig. 1.12. FID mechanism. (a) DIMET process: iteration of DIET process before adsorbate-surface vibrational energy relaxation leads to desorption. (b) Friction process: the coupling between substrate hot electrons and vibrational excitation of the adsorbate and/or adsorbate-substrate bond leads to desorption.

usually applicable for low lying adsorbate resonances with respect to the Fermi level [77].

In both models, hot electrons whose energies are resonant to the adsorbate play a critical role in FID. When the hot electronic temperature is denoted as T_{el}, the desorption probability should depend on T_{el}. The temporal evolution of T_{el} and T_{ph} have been evaluated by a two-temperature model [77-79], described by:

$$C_{el}\frac{\partial}{\partial t}T_{el} = \nabla_z \kappa \nabla_z T_{el} - g(T_{el} - T_{ph}) + S(z,t) \tag{1.12}$$

$$C_{ph}\frac{\partial}{\partial t}T_{ph} = g(T_{el} - T_{ph}) \tag{1.13}$$

where $C_{el} = \gamma T_{el}$ and C_{ph} are the electron and lattice heat capacities, respectively, with the electron specific heat γ. κ and g denoting the thermal conductivity and the electron–phonon coupling constant, respectively. T_{ph} is the phonon temperature. Generally, the laser beam diameter is much larger than the electron diffusion length. Thus, lateral diffusion can be neglected, resulting in reducing the dimensionality to the distance z along the surface normal. The laser source term is given by,

$$S(z,t) = (1-R)I(t)\frac{Exp[-z/\alpha]}{\alpha} \tag{1.14}$$

where R is the reflectivity, α the optical penetration depth, and $I(t)$ the temporal laser beam profile. The lattice heat capacity is given by the Debye model,

$$C_{ph} = 9nk_B\left(\frac{T_{ph}}{\theta_D}\right)^3 \int_0^{\theta_D/T_{ph}} \frac{x^4 e^x}{\left(e^x - 1\right)^2} \tag{1.15}$$

where n is the atomic density, k_B the Boltzmann constant, and θ_D the Debye temperature.

In the Friction model, the coupling of electron and phonon baths to the adsorbate can be described by the harmonic oscillator master equation [70]. Within fs laser excitation T_{el} and T_{ph} are not equilibrated, therefore the friction coefficient η_{el} and η_{ph} should be considered separately. In such a case, the temporal evolution of the average vibrational energy U_{ads} is represented by [66],

$$\frac{d}{dt}U_{ads} = \eta_{el}\left(U_{el} - U_{ads}\right) + \eta_{ph}\left(U_{ph} - U_{ads}\right) \tag{1.16}$$

where the vibrational energy $U_x = \frac{h\nu_{ads}}{Exp[h\nu_{ads}/k_B T_x]-1}$, T_x is the temperature of the desiginated heat bath, and ν_{ads} the vibrational frequency of the adsorbate along the reaction coordinate. T_{ads} can be obtained from equation (1.16) with equation (1.12) and (1.13). The desorption rate *R*, the so called empirical Friction model, is given by an Arrhenius–type expression

$$R(t) = -\frac{d}{dt}\theta = \theta^n k_0 Exp[-\frac{E_a}{k_B T_{ads}}] \tag{1.17}$$

where θ is the coverage, n the order of desorption, and k_0 is the attempt frequency. Finally, the desorption yield measured in experiment, *Y*, can be obtained by

$$Y = \int R(t)dt \tag{1.18}$$

It is worth mentioning that equations (1.16) - (1.18) are originally proposed for the Friction model because they are based on the coupling of a thermalized electron bath to the adsorbate. However, the derived equations might be still applicable for the DIMET model. In this case, the friction coefficient η_{el} can be understood as the energy gained by a single DIET process, and T_{el} is the parameter for the iteration of the DIET process in the DIMET model.

Chapter 2. Experimental

This chapter outlines experimental details of the apparatus used in this work, principles of measurements, and data analyses. The UHV system is described in section 2.1. Then, the sample preparation for Ag(111) and the formation of Ag NPs are mentioned in section 2.2. Section 2.3 and 2.4 describe the principle, experimental setup, and data analysis of TPD, mass selected TOF, and PID measurements.

2.1. UHV system

To study photochemical processes on the clean solid surfaces at the atomic scale, the use of a UHV system was required. Thus, a UHV chamber was used in this study. It consists of two chambers with cylindrical shape (diameter = 40 cm), which are vertically separated by a gate valve. Both chambers are pumped independently by single turbo molecular pumps. Both turbo molecular pumps are connected with a rotary pump which achieves 10^{-3} mbar. The lower chamber is also equipped with an ion pump and a Ti-sublimation pump. Base pressures in the upper and the lower chambers are below 1×10^{-10} and 5×10^{-11} mbar, respectively. The arrangements of the UHV devices in the two chambers are displayed in Fig. 2.1. The upper chamber is equipped with an ion sputtering gun, LEED/AES optics, a differentially pumped, multiplex QMS (HIDEN HAL/3F PIC) with a skimmer (2 mm entrance) for TPD measurements, a Ag evaporator, and a quartz micro balance. The lower chamber consists of a QMS (Balzers QMS311) with a liquid nitrogen cooled shield for the ionizer for mass selected TOF. It also includes detectors for 2PPE and REMPI [80] which were not used and not shown here. On top of the upper chamber, a sample manipulator consisting of a rotation stage, a Z-translator, and an x-y stage was attached. Sample preparation and TPD measurements were performed in the upper chamber and mass selected TOF was measured in the lower chamber.

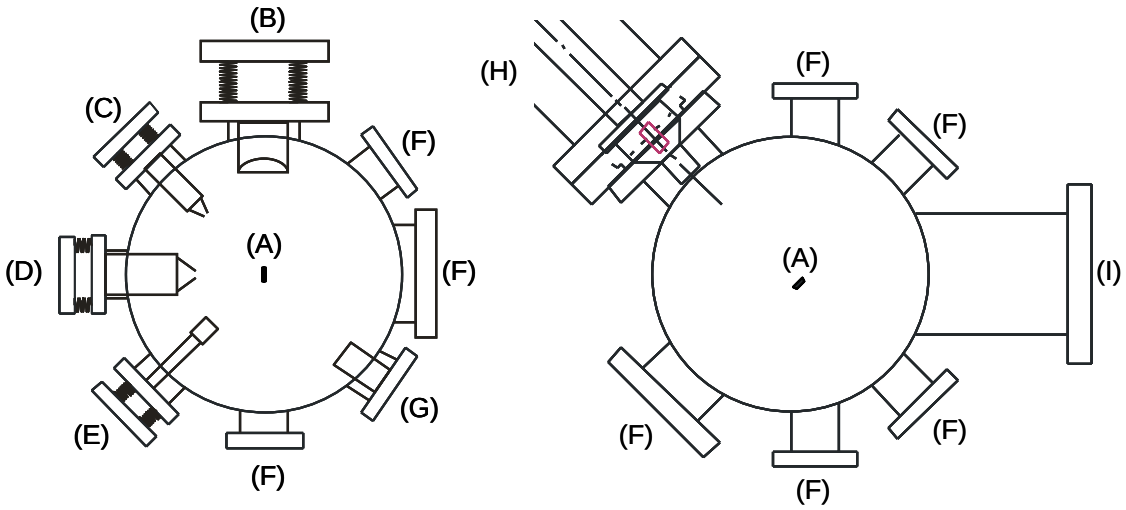

Fig. 2.1. Schematic drawing of the UHV chamber. Left: preparation (upper) chamber, Right: measurement (lower) chamber. (A) sample, (B) LEED/AES, (C) Ag evaporator, (D) QMS for TPD, (E) micro balance, (F) window, (G) Sputter gun, (H) QMS for mass selected TOF, (I) detector for 2PPE.

2.2. Sample manipulation and preparation

A single crystal Ag(111) and NiAl(110) disks (10 mm in diameter, 2 mm thick) were used in this study. The samples were mounted at the bottom of the cold head, coolable with both liquid nitrogen and helium. Two crystals were supported in opposite surface directions. Thus, the crystal for preparation or measurement can be chosen by rotating the manipulator. The detailed sample installation, cleaning procedures, and Ag nanoparticles growing method on alumina oxide are given in this section.

2.2.1. Ag(111)

The Ag(111) crystal was supported by a pair of tantalum wires (0.25 mm in diameter) connected to the cold head. To enable spotwelding of the supporting wires with the Ag sample, the edge of the Ag(111) crystal was tightly wrapped with a 2 mm wide tantalum ribbon (0.1 mm thick) on which the wires were spotwelded. This is because a Ta wire cannot be spotwelded directly on the edge of the Ag sample whose thermal conductivity is too high. The sample temperature was measured by a Chromel-Constantan thermocouple (type *E*, 0.08 mm in diameter) spotwelded to the Ta ribbon around the crystal edge. The sample was heated by electron bombardment from a tantalum filament (0.19 mm in diameter) near its back and could be cooled to below 30 K by liquid helium. The sample surface was cleaned by repeated cycles of Ar^+ sputtering (500 V, 3 μA, 20 minutes) at 527 K and annealing to 723 K for 20 minutes. To obtain a mirror surface of a newly polished Ag(111) crystal, it was crucial to sputter right after its first installation into the vacuum (~10^{-8} mbar), before any heating or baking of the UHV chamber. Otherwise, the surface turned milky and never became clear even after prolonged cleaning cycles. The crystal structure was checked by LEED and the surface purity was measured by AES and TPD of NO.

2.2.2. Ag Nanoparticles on thin alumina films

The Ag NPs used in this study were grown on an Al_2O_3/NiAl(110) substrate. The NiAl sample was mounted in a similar way to that for the Ag (111) sample; the edge of the NiAl(110) was directly spotwelded to a pair of supporting tantalum wires (0.25 mm in diameter) connected to the cold head. A Chromel-Constantan thermocouple (type *E*) was

also spotwelded to the crystal edge. The NiAl(110) surface was cleaned by Ar^+ sputtering (1500 V, 5 μA, 60 minutes) at 700 K and annealing to 1250 K for 5 minutes. Subsequently, the crystal was exposed to 4×10^{-6} mbar oxygen at 540 K for 15 minutes and annealing at 1200 K for 2 minutes, which leads to an ordered film structure. The oxidation procedure was repeated 3 cycles, resulting in a well ordered and smooth structure of an alumina oxide film which consists of two aluminum-oxygen double layers and whose thickness is close to 5 Å [81-83].

After the oxidation, Ag atoms were subsequently deposited from an evaporator with a molybdenum oven heated by electron beam acceleration (voltage: 800 V, emission current: 10 mA, flux of evaporant: 1 μA). The deposition rate was calibrated before each Ag evaporation by the quartz micro balance (~1 Å per 90 s). A sticking coefficient of unity was assumed like many other transition metals on clean oxides at room temperature [84-86]. During evaporation, the sample temperature was kept at room temperature and the sample was positively biased at a higher voltage than the electron beam voltage to prevent the damage of the alumina oxide layer by Ag^+ formed in the evaporator.

The sample position for Ag evaporation had to be adjusted carefully, because the diameter of the Ag atom beam (11.5 mm) was only slightly larger than the sample diameter (10 mm). To achieve a uniform Ag distribution on the Al_2O_3/NiAl(110), AES was used to monitor the coverage of deposited Ag to optimize the sample position for evaporation. Fig. 2.2 shows results of Ag AES measurements as a function of distance from the center of the sample after the sample position for evaporation was optimized. Here Ag atoms are distributed on the whole sample surface. X and Z denote the distance from the center of the sample along the horizontal and vertical directions, respectively.

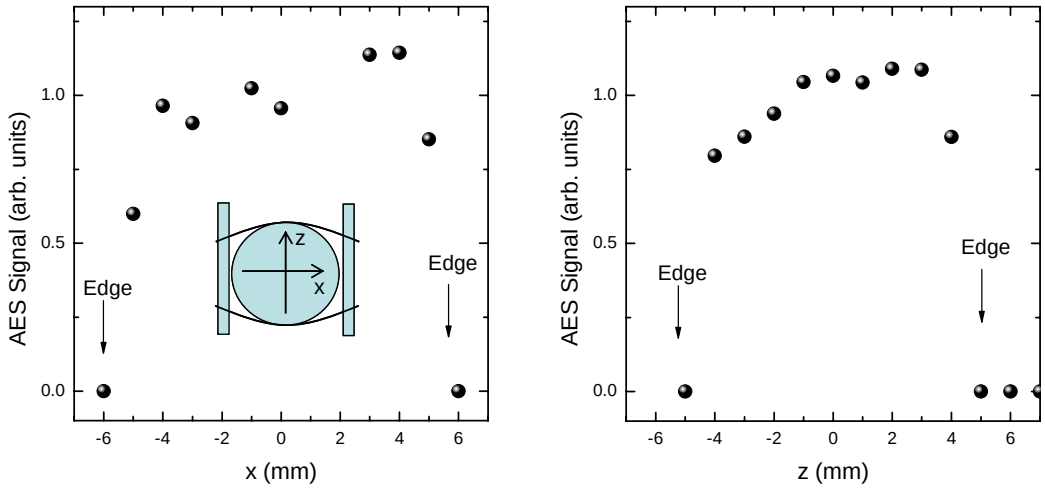

Fig. 2.2. Ag AES intensity as a function of the distance from the center of the sample in the horizontal (left) and the vertical (right) directions.

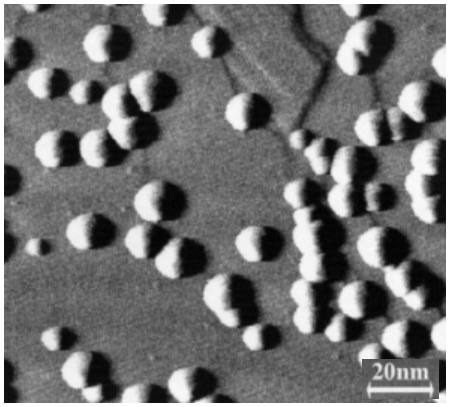

Fig. 2.3 STM (constant current topography) image of Ag nanoparticles on an Al_2O_3 film. Ag was depositied at room temperature. U_{tip} = -2 V, average thickness is 2 Å. Reprinted from ref. [87], Copyright (2002) with permission from Elsevier.

It is known that Ag atoms deposited on a Al_2O_3/NiAl(110) surface form particles via the Volmer-Weber growth mode. Fig. 2.3 displays an STM image of Ag nanoparticles grown on the alumina film [87]. As interaction between Ag and the oxide film is weak, Ag grows as 3D particles on defect sites such as domain boundaries or step edges.

Since the density of nucleation sites is known to be constant ($\approx 4\times10^{11}/cm^2$), the mean particle size can be varied by controlling deposition time. In Fig. 2.4 , the mean particle size measured by STM is plotted as a function of the total amount of Ag deposited at room temperature. It is proportional to the cubic root of the deposited Ag atoms on the alumina oxide film. In the case of mean particle size $\geq$ 10 nm, coalescence of the particles is expected [88]. As the sticking coefficient and the particle density decreased with increasing substrate temperature [28, 89], Ag deposition was always performed at room temperature. The mean particle size was estimated by the plot in Fig. 2.4.

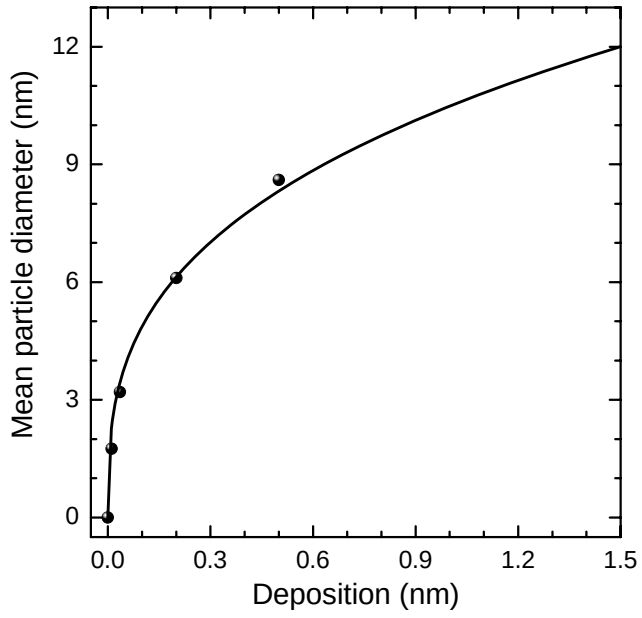

Fig. 2.4. Mean particle diameter as a function of Ag deposition on the Al_2O_3/NiAl(110). The closed symbol is taken from STM measurements by the Photon STM group [90]. The data are fitted to the cubic root of the deposition (solid line) based on the 3D growth mode,

2.2.3. Adsorption of reactant molecules

The reactant gases, namely, NO, N_2O, and Xe, were adsorbed on the sample surface in vacuum after the preparation. The gases were introduced through a copper tube (~8 mm in diameter) ending about 3 cm in front of the sample and connected to a pulsed valve (General Valve Corp.). Prior to gas dosage, the sample was flashed to room temperature to remove contaminants (mainly CO_2 and H_2O) and cooled down to temperatures suitable for the respective gases. The sample temperature was kept constant during dosage. The pressure in front of the sample was estimated to be in the order of 10^{-5} mbar, whereas the background pressure during gas dosage was kept below ~ 2×10^{-9} mbar. This minimized the condensation of gases on the cold head. The gas dosage per opening of the pulsed valve (for ~1 *ms*) was calibrated by measuring TPD peak areas of adsorbates. Either by keeping the substrate temperature above the condensation temperature of the gas or by controlling the number of gas pulses, a well-defined monolayer (ML) of molecules/atoms was formed.

The purities of NO, N_2O, and Xe gases were 99, 99, and 99.999 %, respectively. The N_2O and Xe gases were used without further purification. In contrast, the NO gas was purified by a cold trap connected after the gas cylinder. The trap was cooled by a mixture of ethanol and liquid nitrogen (-114 °C) and impurities such as N_2O were removed.

2.3. Temperature programmed desorption (TPD)

TPD measurement is a widely used and versatile technique to study adsorbate coverage, adsorption species, surface-adsorbate binding energy, and so forth [91, 92]. The main concept is observing desorbed molecules from a surface when the surface is heated.

The theory of this method can be explained as following. The desorption rate against temperature is generally expressed by the Wigner-Polanyi equation,

$$-\frac{d\theta_{ins}}{dt} = \nu_n \cdot {\theta_{ins}}^n \cdot \exp\left(\frac{-E_{des}}{RT_s}\right) \tag{2.1}$$

where θ_{ins} is the instantaneous coverage, ν_n the frequency factor, n the desorption order, E_{des} the activation energy for desorption, R the gas constant, T_s the surface temperature. During TPD, the sample can be heated linearly by means of a computer control,

$$\begin{aligned} T_s &= T_0 + \frac{dT_s}{dt}t \\ &= T_o + \beta t \end{aligned} \tag{2.2}$$

where β is the heating rate ($K \cdot s^{-1}$).

In practice, four reaction types of desorption order are frequently observed. The typical behaviors of zero-order desorption kinetics ($n = 0$) are having a common leading edge for all initial coverages, a rapid drop after the desorption peak and a shift of peak temperature with coverage. It has been commonly observed in thick multilayers. In the case of first-order desorption ($n = 1$), Redhead has derived an equation to estimate E_{des} by assuming coverage independent ν_n and E_{des} [93]

$$E_{des} = RT_{\max}\left(\ln\frac{\nu_1 T_{\max}}{\beta} - 3.64\right) \tag{2.3}$$

where $T_{\max}$ is the peak temperature. The typical features are that the desorption rate is proportional to the instantaneous coverage, the peak temperature is constant with increasing initial coverage, and the peak shape is asymmetric. Second-order desorption ($n = 2$) is observed for recombinative desorption. In this case, the desorption rate is proportional to the square of instantaneous coverage, the peak temperature moves to

lower temperature with increasing initial coverage, the peak shape is almost symmetric and all coverages have common trailing edges. Finally, fractional-order desorption ($0 < n < 1$) is occasionally observed. A characteristic property is that the peak temperature shifts to higher temperature as the initial coverage is increased. It may indicate cluster formation on surface.

It should be noted that TPD is a destructive measurement. The adsorbate sitting on a certain adsorption site can be modified before thermal desorption or reaction during sample heating, resulting in a loss of initial information before sample heating. To study initial adsorbate states on the surface, other methods, e.g., IR spectroscopy, STM, SFG, etc., should be used.

TPD was used for two situations throughout this thesis, i.e. pre-irradiation and post-irradiation TPD. The pre-irradiation TPD was performed to investigate the initial adsorbate coverage, adsorption species, and thermally induced chemical reaction. The post irradiation TPD, on the other hand, was used to observe reduced adsorbate coverage, photoproducts on the sample surface, and modified surface binding energy compared to those in the pre-irradiation TPD. The QMS in the upper chamber for TPD is mounted to a linear translator which allows it to move to the sample and is differentially pumped. Its entrance (2 mm) is smaller than the size of the laser beam irradiated area on the sample. Thus, the signal from an unirradiated region was minimized in post-irradiation TPD.

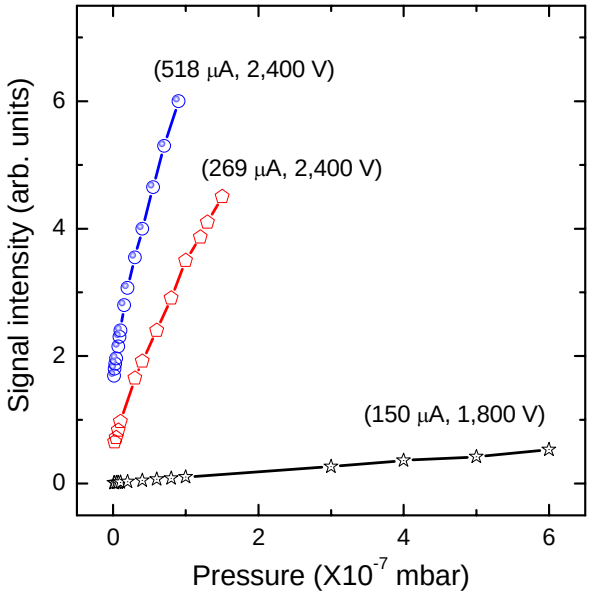

Fig. 2.5. QMS signal intensity as a function of pressure. (emission current, SEM voltage)

The QMS signal count can be nonlinear at high desorption rate. Thus, the QMS signal against N_2O gas pressure was measured in a separate experiment, which is presented in Fig. 2.5. In this study, emission current: 269 μA and secondary electron multiplier (SEM) voltage: 2400 V of the QMS ionizer was used, and it was confirmed that the desorption signal was in the linear regime throughout all of the TPD measurements.

The sample temperature was measured by using an E-type thermocouple, which is non-magnetic and suitable for low temperatures to high temperatures (<1200 K). The

wire thickness (0.08 mm) was thin enough to neglect heat flow through it. The sample temperature was feedback controlled and increased linearly at a rate of 0.5 K/s. The measurement software has been programmed in a LabVIEW environment previously (homemade data acquisition system developed by Kazuo Watanabe). The sample is heated by electron bombardment from a tantalum filament near its back and could be cooled below 30 K by liquid helium. The accuracy of the temperature reading was investigated by TPD of mutilayers of xenon on the surface by comparing to ref. [94]. The error was estimated ±2 K at 60 K.

During TPD measurements, the sample was positioned ~ 0.5 mm in front of the QMS skimmer. The distance of 0.5 mm was small enough to minimize signals from the sample holder and rear side of the sample. The sample was biased at around -100 V to repel stray electrons from the QMS ionizer which can cause electron beam damage of adsorbates.

Multiple mass numbers were observed quasi-simultaneously by multiplexing the QMS signals. The relative sensitivity, for example, NO, N_2, and N_2O, were calibrated by measuring the cracking patterns and the relative sensitivity for this QMS, which are shown in Table 2.1. The signal intensities for N_2, N_2O, and NO were measured in steady-state pressure, 1×10^{-7} mbar by backdosing. The relative intensities of parent and fragment signals depend on the ionizer conditions, such as emission current and SEM voltage. The relative sensitivity for each molecule at the same pressure is calculated with respect to NO. The cracking pattern of N_2O was 100 : 14 : 4 for N_2O, NO, and N_2, respectively, with emission current = 269 μA and SEM voltage = 2.400 V, for example.

Table 2.1. Relative QMS sensitivity and fragments under pressure = 1×10^{-7} mbar. (emission current = 269 μA, SEM voltage = 2.400 V)

Dosed molecule	*Counts/second*			*Relative sensitivity*
	N_2	**N_2O**	**NO**	
N_2	529000	0	0	2.12
N_2O	11500	280000	38000	1.12
NO	0	0	250000	1.00

2.4. Investigation of photodesorption dynamics by mass-selected TOF and PID

2.4.1. Principles

Photodesorption has been successfully explained by the MGR model [4, 63] or the Antoniewicz model [9] as mentioned earlier. The translational energy distributions and the photodesorption cross sections reflect the details of photodesorption dynamics and intial adsorption states, etc. In this thesis work, mass selected-TOF and PID measurements were used.

In the case of photodesorption initiated by a laser pulse, the velocity of a desorbed molecule can be determined by measuring its flight time t from the surface to the detector. The basic idea of the TOF method is estimating the translational energy E_t of the desorbed molecule by the measured flight time t with an equation,

$$\begin{aligned} E_t &= \frac{1}{2}mv^2 \\ &= \frac{1}{2}m\left(\frac{L}{t}\right)^2 \end{aligned} \tag{2.4}$$

where m is the mass of the desorbed molecule, L the distance from the surface to the detector. A QMS with an electron impact ionizer has been used to measure TOF spectra throughout this thesis. The detected signal intensity, therefore, is proportional to the density of the desorbed molecule. This means that faster molecules spend less time in the QMS ionizer than slow molecules, resulting in less signal intensity. Thus, the TOF distribution of desorbed molecules is different from the measured TOF spectrum. The velocity distribution of desorbed molecules on the surface can be fitted by a flux-weighted Maxwell-Boltzmann distribution in the functional form of [2, 45, 95]

$$f(v) \propto v^3 \exp\left(-b(v - v_0)\right) \tag{2.5}$$

where v_0 is a shift from Maxwellian, which is zero for the molecules produced by a supersonic free jet expansion. For the TOF spectra measured with a QMS with an electron impact ionizer, a modified flux-weighted Maxwell-Boltzmann functions for the TOF distribution is used;

$$g(t) \propto \frac{1}{t} \cdot f(v) = \frac{a}{t^4}\exp\left(-b\left(\frac{L}{t} - v_0\right)\right) \tag{2.6}$$

where a, b are the parameters for amplitude and spread, respectively. The $1/t$ in equation (2.6) stems from the speed of molecules in the ionizer, which is mentioned above. The desorption flux and the mean translational energy $<E_t>$ can be obtained by numerical integration of the fitted function. The translational temperature T_t is expressed by $T_t=<E_t>/2k_B$, where k_B is the Boltzmann constant.

The term PID is used for measurements in which the time evolution of the total photodesorption signal (at a single mass number) integrated by flight time is studied. The signal intensity in PID measurements can be assumed to be proportional to the coverage of photoactive adsorbates. If there are only single adspecies and a single photodesorption pathway, the rate of PID signal change corresponds to the photodesorption cross section. The procedure of the PID data analysis will be presented below.

2.4.2. Setup for mass selected-TOF and PID measurements

The optical setup and data acquisition for the TOF measurement is represented in Fig. 2.6. Nanosecond and femtosecond laser pulses have been alternatively used. Two PMTs are adopted for laser pulse detection, which are connected to Quad CFDs to produce accurate timing information from analog signals of varying heights but the same rise time. PMT1 is assigned to start pulses for a multichannel scaler (FAST MCS 7882), and PMT2 is used for the shutter drive.

The laser beams were introduced to the UHV chamber through a magnesium fluoride viewing port. The incident angle of the laser beams is usually 45 degrees from the surface normal, but it is varied by rotating the manipulator when it is necessary. The frequency of photoirradiation was reduced from 1 kHz (the repetition rate of the femtosecond laser) to 50 Hz so that the data acquisition system can follow all the photodesorption events. The master clock of the regenerative amplifier was divided by five with a TTL frequency divider, and its output triggered an optical chopper (New Focus Model 3501, with a modified wheel) with a 20:1 rate, resulting in a 100:1 division in total.

Photodesorbed molecules were detected for each laser pulse by the QMS in the lower chamber in pulse counting mode. The signal pulse (Fast NIM) from the LN_2 cooled QMS was sent to an ORTEC preamplifier to amplify with very fast rise times and was distributed to a ORTEC 100 MHz discriminator for noise filtering, which had two kinds of output, Fast NIM and TTL pulse. The TTL pulse was counted by a LOG/LIN ratemeter, and the Fast NIM pulse was used as a stop pulse for the MCS 7882 to determine the mass selected TOF. The distance between the sample surface and the exit of the QMS ionizer, the flight length of neutral desorbates, was ~19 cm.

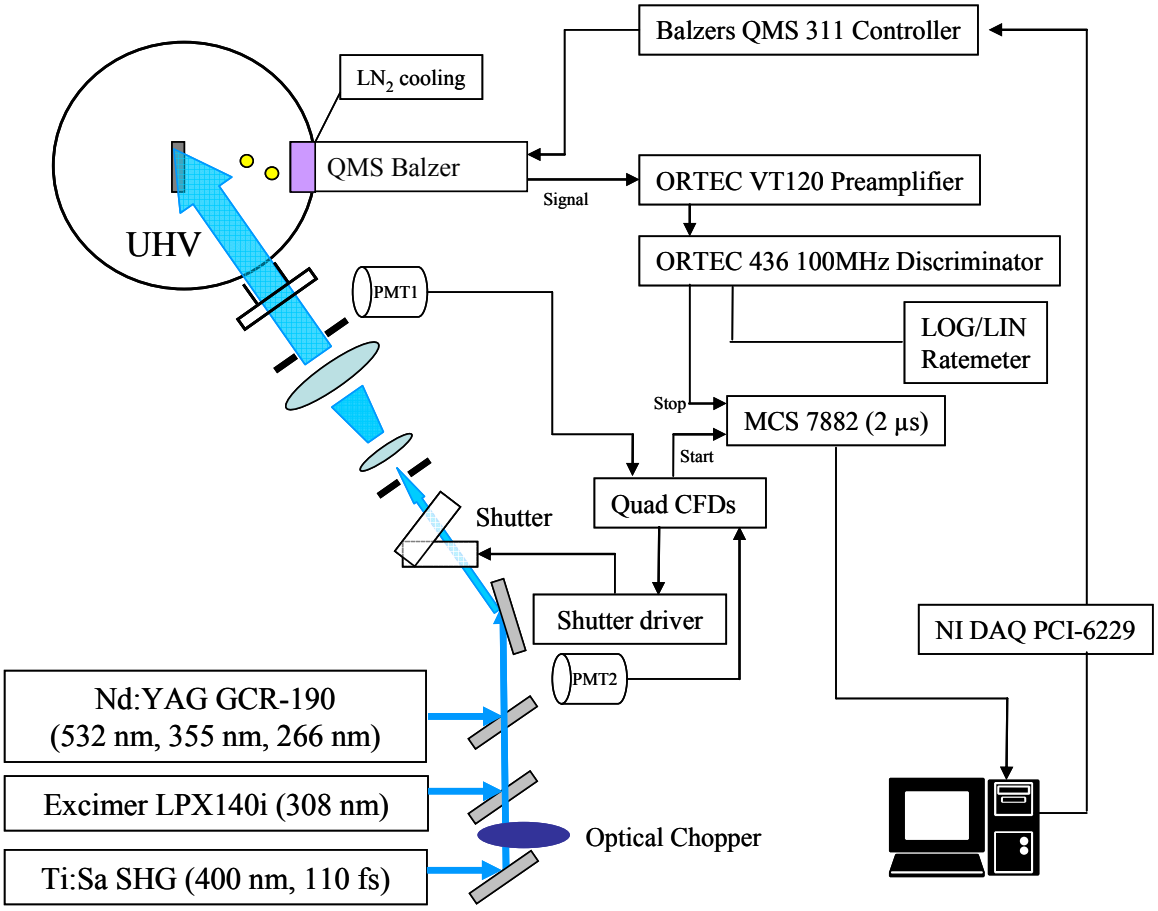

Fig. 2.6. Optical setup and data acquisition system for mass-selected time-of-flight measurements.

2.4.3. Laser system

For photodesorption measurements the sample surface was irradiated with the output from nanosecond lasers or a femtosecond laser. In the case of nanosecond-laser induced desorption, the second (532 nm, 2.3 eV), the third (355 nm, 3.5 eV), and the fourth (266 nm, 4.7 eV) harmonics of a Nd:YAG laser (Spectra Physics GCR-190) and the output of a XeCl excimer laser (4.0 eV, Coherent Lambda Physik LPX140i) operating at 10 Hz were used. The polarization of the light from the former was chosen by rotating the

harmonic generator housing. The light from the latter was non-polarized. The laser beams were introduced to the UHV chamber through a MgF viewing port. The transparency of the viewing port was measured at normal incidence angle for each laser beam, and the results are shown in Table 2.2. The transmittance is defined as transmitted laser intensity / input laser intensity. Since transmittance at normal incidence is polarization independent, the results are used to estimate PCS for each wavelength in *p*-, *s*-, and *non*-polarized laser irradiation.

The nanosecond laser beam from the Nd:YAG or XeCl excimer laser was expanded threefold using a telescope in order to use only the center of the Gaussian beam profile, in order to avoid nonuniform coverages over the irradiated spot during irradiation. The incident angle of the laser beam was 45 degrees from the surface normal. The beam size was set to 7 mm by an iris so that only the sample surface was irradiated.

To generate femtosecond laser pulses, a two-stage regenerative amplifier system (Spectra Physics Spitfire, beam energy ~2 mJ/pulse at 800 nm, pulse width ~80 fs, repetition rate of 1 kHz) was used. It was seeded by a Ti:Sapphire laser (Tsunami) pumped by a Millenia diode laser, and pumped by two pulsed Nd:YLF lasers (Merlin). The second harmonic pulses (400 nm, ~ 110 fs) were generated by a BBO crystal from the output of Spitfire and were then separated from the fundamental beam by a dichroic mirror. The second harmonic beam was directed on to the sample after being trimmed to 2 mm in diameter by an iris without expansion by a telescope in order to achieve higher laser fluences.

Table 2.2. Transmittance of viewing port at normal incidence for different wavelengths. The transmittance is defined as transmitted laser intensity / input laser intensity.

Wavelength (nm)	532	400	355	308	266
Transmittance (%)	94.3	91.0	90.6	87.7	81.0

2.4.4. Ion drift time

The measured TOF consists of the flight time of neutrals between the sample and the ionizer and that of ions between the ionizer and the detector (channeltron). To obtain information about the kinetic energy of desorbates, the neutral flight time must be extracted from the total (measured) flight time by subtracting the ion flight time. Fig. 2.7 shows a schematic diagram of TOF measurements of photodesorbed molecules from the sample surface. The sample covered with adsorbates is irradiated by a laser pulse. Neutral desorbates fly to the QMS with a certain kinetic energy and are ionized at the ionizer (shown as a rectangle). Then they are accelerated and mass-selected by the quadrupoles.

The flight time (length) from the sample surface to the end of ionizer is denoted as T_n (L_n: ~ 19 cm), and the ion drift time (length) from the end of the ionizer to the detector is expressed by T_i (L_i). Thus, the measured flight time T_m is a sum of T_n and T_i. The laser pulse width (~ 10 ns or ~ 110 fs) is negligibly short compared to the typical flight time T_m (> 10 μs) and not considered.

The translational energy of the desorbates at the detector is written as

$$E_m = \frac{1}{2} m \left(\frac{L_i}{t_i} \right)^2 = E_n + IE \qquad (2.7)$$

where m is the mass of the desorbate, E_n the kinetic energy of the neutral desorbate, and IE the acceleration energy after ionization. Therefore, the ion drift time t_i can be written as:

$$t_i = L_i \sqrt{\frac{m}{2(E_n + IE)}}. \qquad (2.8)$$

Fig. 2.8 shows calculated ion drift times of NO and Xe as a function of total flight time (measured flight time) at IE = 30 eV (field axis = 50 V, grid = 80 V). The L_i (~ 0.22 m) was determined by a separate measurement with directly dosed gas into the chamber (E_n = 0). The higher the initial kinetic energy of desorbates, the shorter becomes the ion drift time. The ion drift times are almost constant over 50 and 150 μs for NO and Xe, respectively.

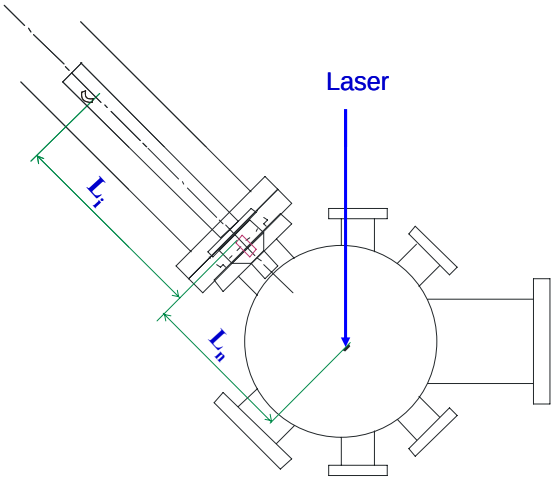

Fig. 2.7. Configuration of TOF measurements. L_n and L_i denote distance from the sample surface (center) to the end of ionizer and from the end of ionizer to the detector, respectively.

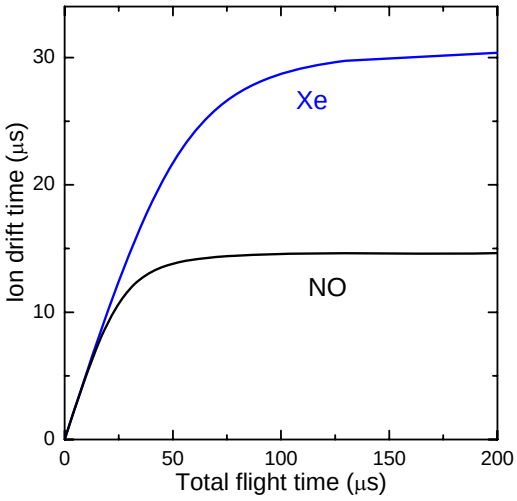

Fig. 2.8. Ion drift time t_i as a function of total flight time. It depends on the initial kinetic energy and mass of the desorbed molecules.

2.4.5. Analyses of TOF spectra and PID data

All the measured TOF spectra were corrected considering the ion drift times mentioned above. The neutral flight time t_n is expressed with a constant IE =30 eV,

$$t_n = t_m - t_i = t_m - L_i \sqrt{\frac{m}{2\left(\frac{1}{2}m\left(\frac{L_n}{t_n}\right)^2\right) + 30eV}} \tag{2.9}$$

The desorption signals as a function of t_m (raw data) and t_n (corrected data) are compared in Fig. 2.9. The raw data is peaked at ~200 μs, and the peak of the corrected spectrum is shifted by ~15 μs to earlier time. This is derived from the curve in Fig. 2.8. It should be noted that all TOF spectra appearing in this thesis are plotted as a function of flight time of neutral desorbates.

The corrected TOF spectra were fitted by a sum of the modified flux-weighted Maxwell-Boltzmann functions given in equation (2.6) in order to estimate the translational temperature of the desorbed molecules. The TOF spectra often show a long

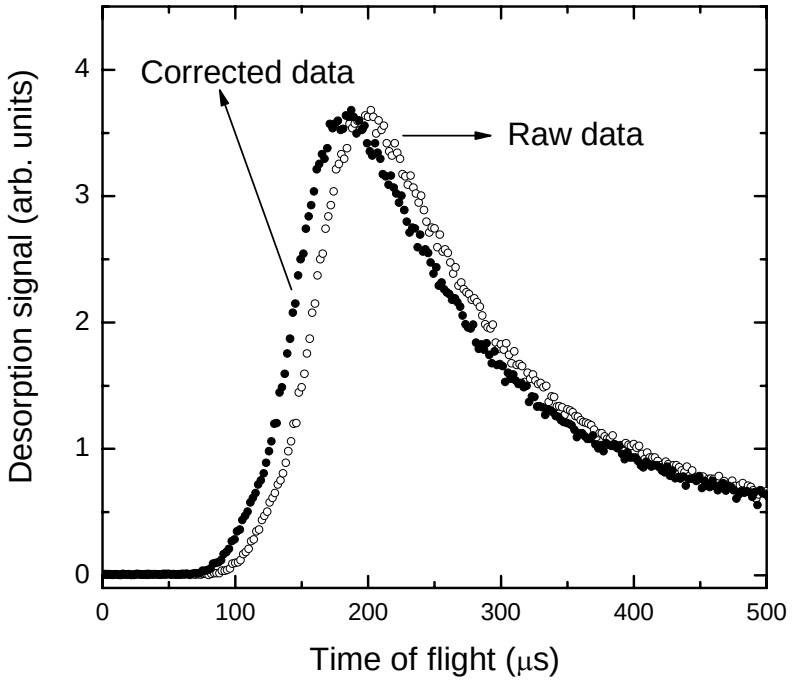

Fig. 2.9. TOF of NO from NO dosed at 75 K on Ag(111) by using 4.7 eV, *p*-polarization. The data is accumulated from the 1st to 4,000th laser shot. Raw data is shifted to earlier time because of ion drift time subtraction.

tail, in addition to the main peak(s). In such a case, an additional Maxwell-Boltzmann function is used to fit the tail. It is attributable to secondary processes among adsorbates/desorbates or multiple scattering near the QMS ionizer, for example. Its translational temperature is usually lower than the thermal desorption temperature of the adsorbate on the surface and its origin is discussed in this thesis.

Fig. 2.10 displays a fitting result of the corrected TOF spectra shown in Fig. 2.9 with a sum of two modified flux-weighted Maxwell-Boltzmann functions. The sum of the two functions is shown by the blue solid curve. The mean translational energy $<E_t>$ is calculated by the numerical integration of the fitted function using software programmed in the Excel VBA environment based on the fitted parameters in equation (2.6). The translational temperature T_t is calculated by the relationship $T_t=<E_t>/2k_B$, where k_B is the Boltzmann constant.

The PCS is defined as the overall cross section of photoinduced processes of the reactant including desorption, dissociation, and site conversion, etc. This definition is based on the fact that the decay of PID data represents the loss of the reactant. It is obtained by fitting the PID data to either a mono-exponential or a bi-exponential function. If photodesorption is the only reaction pathway, the photodepletion cross section is equal

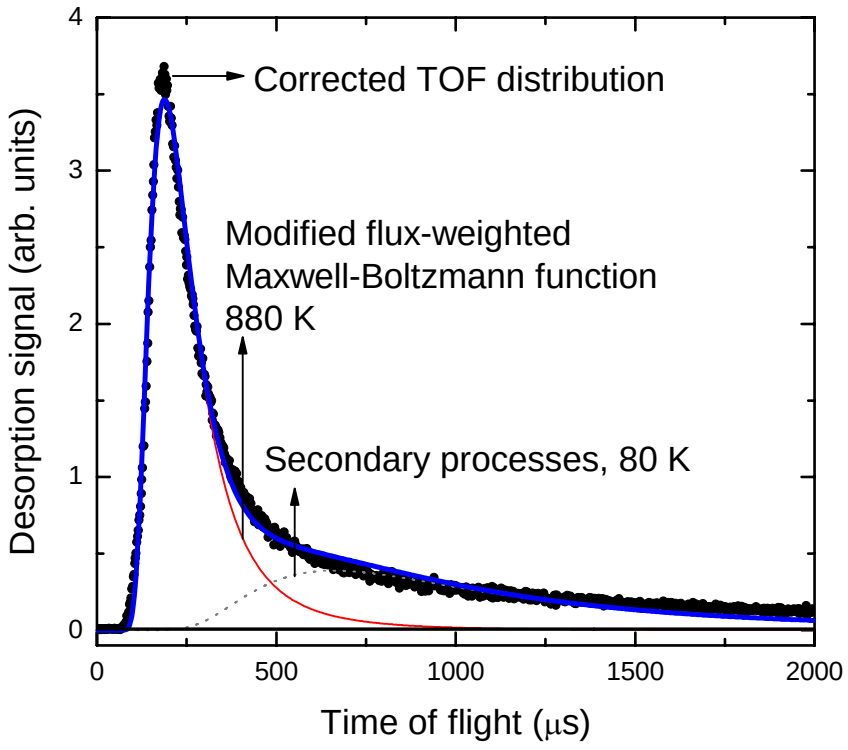

Fig. 2.10. Fitting of TOF distribution after flight time correction with two modified flux-weighted Maxwell-Boltzmann functions. The Blue solid curve represents the sum of two contributions.

to the photodesorption cross section.

Fig. 2.11 displays an example PID data measured from NO/Ag(111), fitted with a single-exponential function,

$$Y = A\exp\left(-\sigma N_{ph}\right) \tag{2.10}$$

where Y is the desorption signal, N_{ph} the irradiance (photons/cm^2), A the intensity, and σ the photodepletion cross section 14.6×10^{-18} cm^2. The data was fitted from the desorption signal driven by the first laser shot to 50% of the maximum desorption signal.

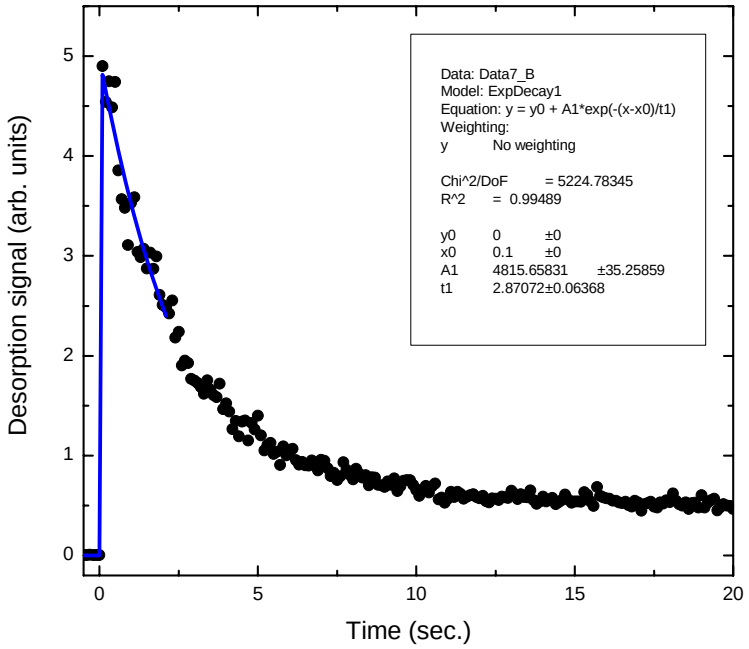

Fig. 2.11. PID curve of NO from NO dosed at 75 K on Ag(111). The curve is obtained from integrations of desorbed molecules in the TOF spectra for 2 ms by single laser pulse, 266 nm, *p*-polarization. The data is fitted with a single exponential until 50% of the maximum desorption signal.

Chapter 3. Thermal- and photoreactions of NO and N_2O on Ag(111)

This chapter presents thermal- and photoreactions of NO on Ag NPs as well as Ag(111), and those of N_2O on Ag(111). The first section deals with thermal and photoreactions of NO dimers and NO monomers on Ag(111). Their electron affinity levels, photodesorption dynamics, photoreaction cross sections, and reaction pathways are investigated. Photochemical formation of both N_2 and N_2O from NO dimers on Ag(111) have been observed by photoirradiation at $\geq$ 2.3 eV. To elucidate the formation mechanism of N_2, thermal- and photoreactions of N_2O on Ag(111) have been investigated. Thus, section 3.2 presents angle-resolved photodesorption measurements of N_2 and N_2O from a N_2O monolayer on a Ag(111).

3.1. Thermal- and photoreactions of NO on Ag(111)

This section presents thermal and photochemical reactions in NO dimer and monomer layers on Ag(111) investigated by TPD, mass-selected PID and TOF measurements. The adsorption states of the NO species were controlled by dosing procedures and annealing temperatures. Their different photoreactivities were further differentiated by photon energy dependent measurements (2.3 – 4.7 eV). While NO dimers are by far the most photoreactive species, NO monomers are shown to be photoreactive as well. Furthermore, direct photochemical formation of N_2 with a very high T_t (~ 5700 K) has been observed for the first time as well as N_2O in photoreactions of NO dimers on Ag(111) induced by irradiating with photon energies $\geq$ 2.3 eV. We propose that this reaction occurs via the simultaneous cleavage of the two N-O bonds followed by the formation of a N-N triple bond of N_2, and can be regarded as mutual abstraction of the N atom from each nitrosyl in $(NO)_2$. Photochemical interconversion

processes between NO dimers and monomers are identified and their significance in the analysis of NO photodesorption is discussed. The photon energy and polarization dependences of the action spectrum of NO photodesorption from NO dimers are shown to be fully understandable by the hot electron yield at the surface. These results clear up some open or controversial points in previous publications and will serve as a reference for an investigation of the same process on Ag nanoparticles for Chapter 4.

3.1.1. Introduction

Photodesorption of NO from metal and semiconductor surfaces has been widely studied owing to the importance of NO as a key molecule in many heterogeneous reactions [96-99]. Because of its particular suitability for state-resolved laser spectroscopic methods [2], very detailed understandings of photoexcitation mechanisms and microscopic desorption dynamics have been obtained for NO chemisorbed on a number of surfaces, for example, Pt [52, 53, 100], NiO [101-104], Pd [65, 105] and Si [106-109]. At low temperatures (below ~ 80 K) NO forms metastable dimers on several solid surfaces [110]. When dimers and monomers coexist, it is essential to distinguish their contributions to photo- and thermal reactions because they possess very different chemical properties.

The complex adsorption structures and thermal reactions of NO on Ag(111) have been studied in detail before. Fig. 3.1 summarizes the adsorption structures of NO [111, 112] and relevant thermal reaction pathways [113] as a function of surface temperature. Below 65 K NO exists as a monomer at low coverages; it condenses to form 3D clusters or multilayers of dimers at higher coverages. Above this temperature a monolayer (ML) of NO dimers are formed [114] in four phases labeled as α, β, γ, δ in Fig. 3.2 [112]. It has been found that the structure α is the least prevalent, while the structure δ is dominant, covering roughly half of the surface. Above 77 K some of the NO dimers, $(NO)_2$(a), dissociate and form N_2O(a) and O(a). NO dimers in the α-, γ-, and δ-phases decompose at 94 K, leading to desorption of NO(g) and N_2O(g) [113]. Here and in the following, (a) and (g) denote adsorbates and desorbates, respectively. Above 77 K, β-phase NO dimers, NO(a) perturbed by O(a), and disordered N_2O(a) and O(a) coexist. At 120 - 125 K, N_2O(a) stabilized by O(a) desorbs. This desorption temperature of the N_2O formed from the reaction of NO on Ag/Ru(0001), which reaches the same behavior as on Ag (111) [115], is higher than N_2O adsorbed on a clean or oxygen-covered surface [116]. Ludviksson et al. [116] speculate that NO_2 which interacts with N_2O causes higher desorption temperature of the N_2O from NO dimer. Carlisle and King [112], however, observed an absence of any other species in the STM images whereas the ringlike

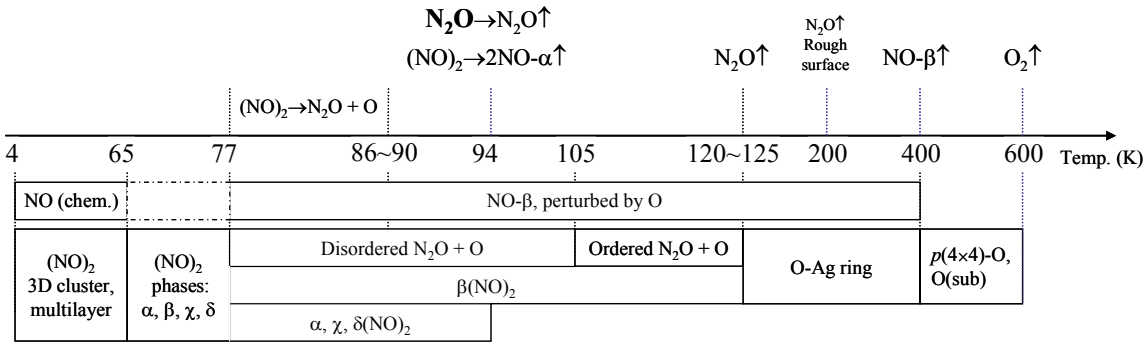

Fig. 3.1. A summary of reactions and structures of NO on Ag(111) as a function of temperature, derived from TPD [113] and STM studies [112].

structures of an oxide after heating to 130 K for 5 minutes, leading to desorption of the N_2O and any remaining NO. Thus, they concluded that optimized interactions between N_2O and O atoms in well ordered phases leads to a high desorption temperature of N_2O formed from the reaction of NO on the Ag surface. The *β*-phase NO dimers decompose into $N_2O(g) + O(a)$ at 120 - 125 K. Some N_2O desorbs at ~ 200 K from defect sites [113]. At ~ 400 K NO(a) perturbed by O(a) finally leaves the surface. At ~ 600 K, remaining oxygen atoms desorb associatively as O_2.

The photochemistry of NO on Ag(111) has been investigated by several groups. Natzle et al. studied photodesorption of NO from thick condensed films of NO (up to 2000 MLs) at 25 - 50 K, where the interaction with the Ag(111) substrate was negligible[117]. Photochemistry of submonolayer NO on Ag(111) and on Cu(111) at 80 - 85 K were studied in detail by Ho and coworkers [62]. They measured photodesorption cross sections of NO and of the photoproduct N_2O for a range of photon energies (2.1 - 4.8 eV). Meech and coworkers [49] measured action spectra (initial photodesorption yield as a function of photon energy) of NO photodesorption and explained them in terms of substrate mediated excitation mechanisms via the polarization dependence – i.e. transfer of hot electrons created in the substrate into an affinity level of the adsorbate and momentum transfer to the desorbing species in the resulting transient negative ion [2] - using a phenomenological model assuming two adsorbate attachment levels located at 1.2 and 3.9 eV above the Fermi level. Later [113] they investigated the photodesorption dynamics and the photochemistry of NO on Ag(111). Depleting the NO dimers by sample annealing, they showed that NO monomers are also photoactive though less efficiently than NO dimers, and that NO is photodesorbed with higher kinetic energy from the monomer than from the dimer.

Recently, Nakamura and Yamashita [118] studied the photodesorption mechanism of NO on Ag(111) using density functional theory (DFT) and a nonequilibrium Green's function approach. They could reproduce the action spectrum measured by Meech and coworkers [49] reasonably well by considering NO dimers as the photoreactive species

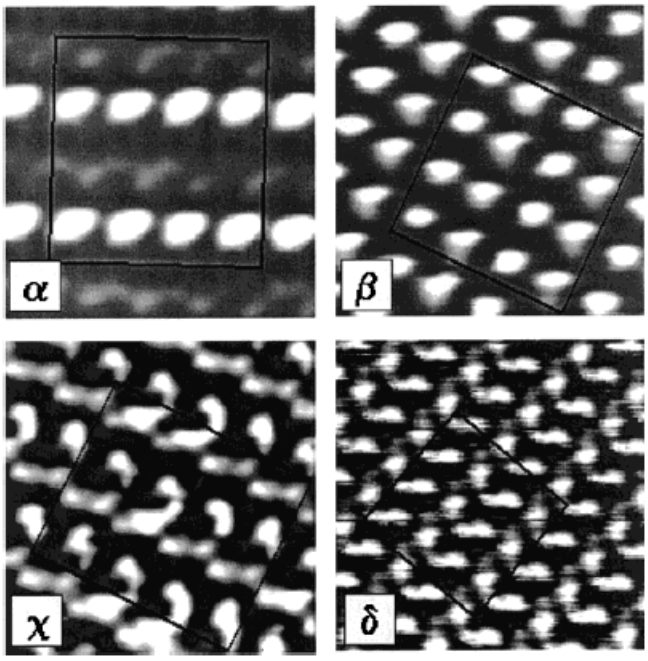

Fig. 3.2. STM images of the four phase structures of NO dimers on Ag(111) at 77 K. Each dimer appears as an elongated bright feature. All were recorded with a 1 V bias and a 1 nA tunneling current. (a) A 30 Å × 30 Å area with a local coverage of 0.125 ML of $(NO)_2$. (b) A 33 Å × 33 Å area with a local coverage of 0.25 ML of $(NO)_2$. (c) A 30 Å × 30 Å area with a local coverage of 0.25 ML of $(NO)_2$. (d) A 44 Å × 44 Å area with a local coverage of 0.25 ML of $(NO)_2$. (Reprinted with permission from ref. [112]. Copyright 2001 American Chemical Society.)

whose calculated resonant level was located at 2 eV above the Fermi level. However, the calculated resonance level for a hypothetical NO monomer (0.6 eV above the Fermi level) was too low to account for the measured action spectrum. This led them to conclude that the NO dimer is the only photoactive species.

In this section, we reexamine the photochemistry of NO on Ag(111) in the range between 2.3 and 4.7 eV. Our main incentive comes from our interest in photochemistry on metal NPs for comparison. A detailed quantitative knowledge of NO photodesorption on Ag(111), obtained by using the same techniques and procedures, is essential as the principle comparison point in this work to assess the changes induced by the small and varied size of the particles. At the same time we wanted to clear up the mentioned discrepancies between previous works. To achieve this we carried out measurements in which we control the adsorption states, for which photodesorption is measured, by the substrate temperature used for preparation.

In the present study, NO was dosed at 75 K on the Ag(111) sample cooled by liquid helium so that only a ML of NO dimers was formed. This is in contrast to the previous photochemistry experiments [49, 62, 113] in which liquid nitrogen was used for cooling and typical sample temperatures were between 80 and 90 K resulting in mixtures of NO, $(NO)_2$, N_2O, and O on the surface (Fig. 3.1) prior to photoirradiation. A monolayer of NO monomers was prepared by heating the NO dimer layer to 130 K to desorb all the NO dimers and N_2O. Photoreactions of NO dimers and monomers were then investigated on these NO layers at ~ 30 K (base temperature) and 130 K, respectively. The use of these

substrate temperatures enabled to be distinguished and compared the photoreactivities of the NO dimer and the monomers.

The reactivity was measured by using the decay of the PID signal at several photon energies (2.3 – 4.7 eV). It will be compared to the calculated surface absorbance as well as to the action spectra in the literature. We confirm that NO monomers are also photoactive. Photodesorption dynamics of NO from both NO dimers and monomers were monitored and distinguished by mass selected-TOF. Photochemical interconversion between dimers and monomers, $(NO)_2(a) \leftrightarrow 2NO(a)$ is revealed by combining TPD and mass selected-TOF data.

3.1.2. Experimental

Pre- and post-irradiation TPD, mass selected TOF, and PID measurements have been performed to investigate thermal- and photochemistry of NO on Ag(111). The sample was dosed at 75 K with NO gas to the saturation coverage, then subsequently cooled down to ~ 30 K for studying of the NO dimer on the surface or heated up to 130 K, holding the sample at this temperature for investigation of the NO monomer on the surface. The dosing temperature of 75 K was chosen to avoid thermal reactions of NO dimers at the higher temperatures and the condensation of NO at the lower temperatures. The second (2.3 eV), the third (3.5 eV), and the fourth (4.7 eV) harmonics of the Nd:YAG laser and the output of the XeCl excimer laser operating at 10 Hz were used. The incident angle of the laser beam was set to 45 degrees from the surface normal. Experimental detail and data analysis are described in Chapter 2.

3.1.3. Thermal reaction and photodesorption of NO on Ag(111)

Pre- and post irradiation TPD of NO

Fig. 3.3 (a) and (b) show the pre- and post-irradiation TPD results from Ag(111) dosed with NO at 75 K to the saturation coverage measured at mass numbers m/e = 30 and 44, respectively. The post-irradiation TPD spectra were measured after the photodesorption signal of NO had decreased nearly to the detection limit: The required total irradiances were ~ 2.0×10^{19}, 1.4×10^{19}, and 1.1×10^{19} photons/cm^2 at 2.3, 3.5, and 4.7 eV in *p*-polarization, respectively.

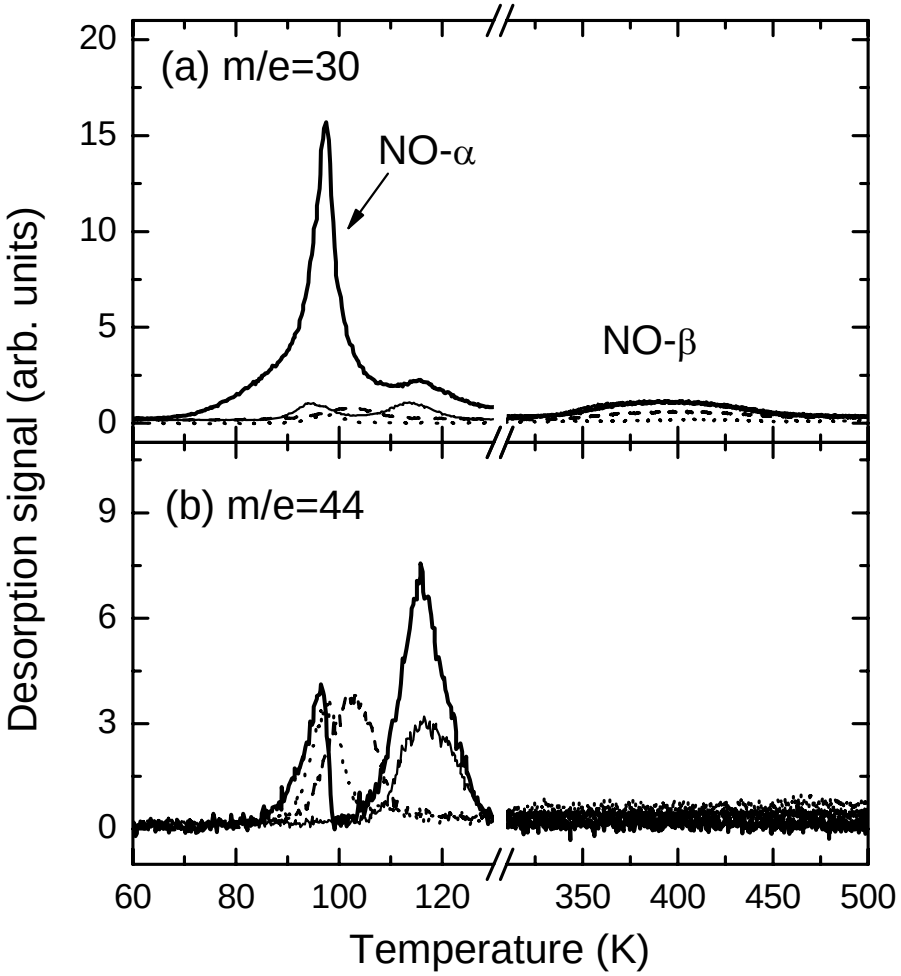

Fig. 3.3. TPD results from Ag(111) dosed with NO at 75 K to the saturation coverage before and after irradiation, measured at mass numbers m/e=30 (a) and 44 (b). The thick solid curves show the data before irradiation. The thin solid, the dashed, and the dotted curves correspond to the results after 2.3, 3.5, and 4.7 eV irradiation in *p*-polarization, respectively.

The pre-irradiation TPD spectrum at m/e = 30 (the thick solid curve) consists of three peaks at ~ 97, 115, and 400 K. Although NO (m/e = 30) was dosed at 75 K, the desorption signal started at ~ 65 K, suggesting structural rearrangements after dosage during sample cool-down. The peak at ~ 97 K originates from dissociation of $(NO)_2$ to emit NO. The peak at 115 K is not due to NO desorption but stems from cracking of desorbing N_2O in the ion source. The broad feature peaked at 400 K starting from ~ 320 K and ending at ~ 500 K is assigned to desorption of NO monomers perturbed by O atoms [113]. In the pre-irradiation TPD result at m/e = 44, two peaks at ~ 97 and 116 K are observed. Both originate from N_2O formation from NO dimers: the former stems from the α, γ, δ-phases and the latter from the β-phase (see Fig. 3.1). The relative

Table 3.1. Relative desorption yields in pre- and post-irradiation TPD of Ag(111) dosed with NO at 75 K (1 ML = the saturation coverage of NO). The numbers in parentheses are desorption peak temperatures.

Photon energy (eV)	Polarization	Total [ML]	NO-α (~ 97, ~ 115 K)	NO-β (~ 400 K)	N_2O (~ 97, ~ 116 K)	N_2 (~ 53 K)
n/a	n/a	1.00	0.39	0.15	0.46	0.00
2.3	*P*	0.40	0.04	0.15	0.20	0.00
3.5	*p*	0.32	0.03	0.09	0.20	0.00
4.0	*non*	0.19	0.013	0.013	0.17	0.05
4.7	*p*	0.15	0.007	0.007	0.14	0.06

desorption yields (θ_d) of NO from the dimers (hereafter NO-α), NO from the monomers (hereafter NO-β), N_2O, and N_2 as well as their peak temperatures are summarized in Table 3.1. The θ_d before irradiation were 0.39, 0.15, and 0.46 ML for NO-α, NO-β, and N_2O, respectively. Note that the relative yields were calculated with respect to the total amount of N atoms on Ag(111) saturated with NO molecules at 75 K (θ_d = 1.00 ML); the θ_d of N_2O appears larger than the observed peak intensities at m/e = 44, as an N_2O molecule contains two nitrogen atoms. It should be noted that as much as ~50% of the initially adsorbed NO dimers preferentially desorb as N_2O in pre-irradiation TPD.

The post-irradiation TPD results of NO show marked photon energy dependence. With 2.3 eV photon irradiation (thin solid curves), the NO-α peak at ~ 97 K is reduced to θ_d = 0.04 ML whereas the NO-β peak at ~ 400 K is almost unchanged (θ_d = 0.15 ML). The N_2O peak (m/e = 44) at ~ 97 K has disappeared and the amount of N_2O is reduced almost by a factor of two (θ_d = 0.20). At $h\nu$ = 3.5 eV, the total amount of nitrogen atoms is decreased by $\Delta\theta_d$ = 0.08 ML compared to that at $h\nu$ = 2.3 eV. This reduction is mainly due to the decrease of the NO-β peak. At $h\nu$ = 4.0 eV (not shown) and 4.7 eV, NO-α and NO-β were almost totally removed, but the N_2O peak remained (θ_d = 0.17 ML and 0.14 ML, respectively) and shifted to ~100 K. At 4.7 eV, an N_2 desorption peak (θ_d = 0.06 ML) at 53 K was also observed (not shown). The formation of N_2 is attributable to photodissociation of the photoproduct N_2O, which has been confirmed by separate post-irradiation TPD measurements of N_2O/Ag(111) (See section 3.2).

It should be noted that the areas of the NO-α, the NO-β, and the N_2O peaks do not indicate the coverages of NO dimers, monomers, and N_2O before the TPD measurement. Thermal conversions of NO species occurring in the TPD measurements lead to loss of information about the initial coverages and adsorption states. For example, the photoproduct NO(a) reacts to form $(NO)_2$(a) thermally; even though NO dimers were

depleted by irradiation, the NO-α peak appears due to this reaction. This suggests that some NO(a) can also contribute to the N_2O peak by the reaction $(NO)_2 \rightarrow N_2O+O$.

In spite of the complexity due to the thermal reactions of NO species, the post-irradiation TPD revealed another photoreaction channel of NO(a). On Ag(111) dosed with NO at 75 K and annealed to 300 K, an N_2O peak was observed in post-irradiation TPD after 4.7 eV irradiation. In contrast, this peak did not appear without irradiation. As both NO dimers and N_2O are depleted by annealing to 300 K, the formation of N_2O can only be explained by a photoreaction of the NO monomers, $2NO \rightarrow N_2O+O$.

Finally, we compare our post-irradiation TPD results with those of Meech et al. In the latter, the NO-β peak persisted even after irradiation with 4.3×10^{19} photons/cm^2 at 4.7 eV [113] whereas we found that it disappeared after prolonged irradiation at $h\nu \geq 4.0$ eV. There is also a difference in the post-irradiation TPD of N_2O. No shift of the N_2O peak was observed between pre- and post-irradiation TPD in Ref.[113], whereas the peak shifted from ~115 K to ~100 K in our case. The downshift of the N_2O peak indicates a reduction of the coverage of oxygen atoms; N_2O on a clean Ag(111) desorbs at ~ 80 K whereas the N_2O peak is shifted to ~ 120 K after photodissociation of N_2O into N_2 and O (See section 3.2). These differences between Meech's and our post-irradiation TPD may have resulted from the different sample temperatures during gas dosage and photoirradiation.

Photoinduced desorption of NO

Fig. 3.4 displays PID signals of NO (30 amu) from NO adsorbed on Ag(111) at 75 K, measured at $h\nu = 2.3$ eV (triangles), 3.5 eV (squares), and 4.7 eV (circles) in *p*- (solid symbols) and *s*-polarization (open symbols), respectively, up to a total number of photons of 1.6×10^{18} cm^{-2}, in a logarithmic scale. The signal intensities were normalized by the number of photons per pulse (per-shot irradiance) for comparison. With increasing photon energy, the PID intensities increase, and decay faster. At $h\nu = 2.3$ eV, the slope of the PID signal is almost constant; it can be fitted to a single exponential decay function. In contrast, at $h\nu = 3.5$ and 4.7 eV, the decay slows down as the number of photons is increased. PID measurements of NO dimers (60 amu) were attempted, but no signal was observed.

Fig. 3.5 presents PID results of NO measured at $h\nu = 4.7$ eV in *p*-polarization from Ag(111) covered with differently prepared NO adsorbates. The small solid circles show the PID result from Ag(111) dosed with NO at 75 K, which is identical to that in Fig. 3.4. The open squares correspond to PID from Ag(111) dosed with NO at 85 K. With the dosing temperature at 85 K, the initial intensity of the fast decaying component is reduced to 55% of that of 75 K dosing, whereas the slow component is almost unchanged. This change is attributed to thermal decomposition of NO dimers to form N_2O and O at 85 K

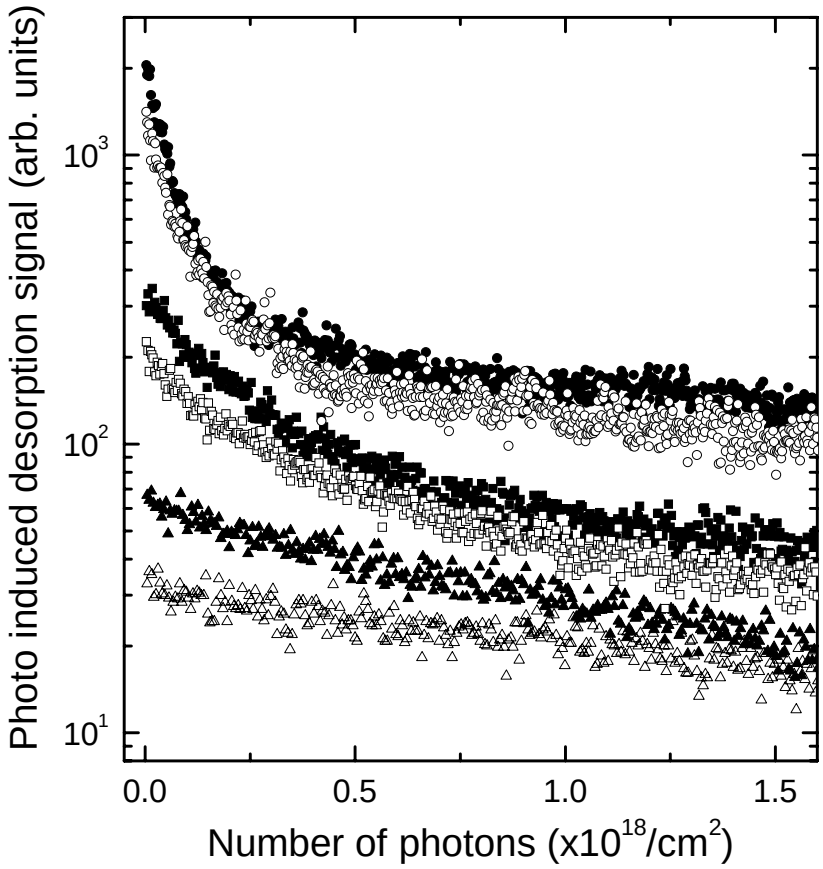

Fig. 3.4. PID results of NO from Ag(111) with the saturation coverage of NO dosed at 75 K measured at hν = 2.3 eV (triangles), 3.5 eV (squares), and 4.7 eV (circles), in *p*- (filled symbols) and *s*- (open) polarizations, respectively.

(see Fig. 3.1). The large solid circles show a PID result from Ag(111) dosed with NO at 75 K and subsequently annealed to 300 K to deplete NO dimers and N_2O. In this case, only NO monomers should contribute to the PID signal, which decays linearly at the same rate as the slow component in the other cases.

The photodepletion cross section (PCS) of NO at different photon energies, i.e., the cross sections derived from the decay of PID signal with irradiation, is summarized in Table 3.2. Note that the PCS is the overall cross section of photoinduced processes of the reactants which lead to a decrease of their concentrations, including desorption, dissociation, and site conversion, etc. Obviously, the PCS can be changed with progressing photoreaction. If photodesorption is the only reaction pathway, the PCS is equal to the photodesorption cross section. Limiting values are obtained by fitting the PID data to either a single-exponential or a bi-exponential function.

In fitting by a single-exponential function, data from the desorption signal driven by the first laser shot to 50% of the maximum desorption signal were fitted by the formula,

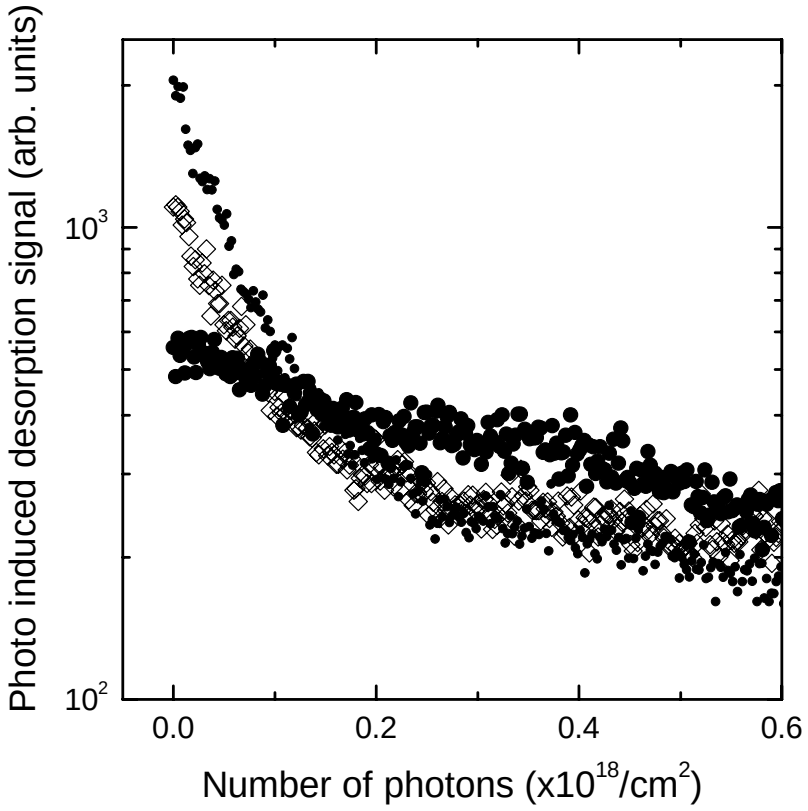

Fig. 3.5. PID results of NO from Ag(111) measured at hν = 4.7 eV in *p*-polarization for the saturation coverages of NO formed at 75 K (small solid circles) or 85 K (open squares); and at 75 K followed by annealing to 300 K (big solid circles), respectively.

$Y = A\exp(-\sigma N_{ph})$, where Y is the desorption signal, N_{ph} is the irradiance (photons/cm^2), A the intensity, and σ the PCS. The signal in the initial decay originates mainly from NO dimers as discussed above. Therefore, the PCS obtained by the single-exponential function can be regarded as those of the NO dimers.

At hν ≥ 3.5 eV, the PID decay deviates from a single-exponential function and must be fitted at least by a bi-exponential function, $Y = A_f \exp(-\sigma_f N_{ph}) + A_s \exp(-\sigma_s N_{ph})$, where A_f and A_s are the intensities, and σ_f and σ_s the PCS of the fast and the slowly decaying components ($\sigma_f > \sigma_s$), respectively.

The fitted values of σ and σ_f are close to each other. Therefore σ_f can also be regarded as the photoreaction cross section of the NO dimers. However, caution is necessary for the interpretation of σ_s. It cannot be simply taken as the photoreaction cross section of the NO monomers because the bi-exponential fitting is only phenomenological; it assumes that some NO monomers exist already at $N_{ph} = 0$, which is not the case under our experimental conditions (Ag(111) dosed with NO at 75 K), where only NO dimers

Table 3.2. Photodepletion cross sections of NO from Ag(111) dosed with NO at 75 K. (Unit: 10^{-18} cm^2)

Photon Energy (eV)	Polarization	Cross Section, σ (Single-exponential fit to 50% decay)	Cross sections (Bi-exponential fit)	
			Fast, σ_f	Slow, σ_s
2.3	*P*	0.86	N/A	N/A
	S	0.39	N/A	N/A
3.5	*P*	3.9	4.5	0.17
	S	2.8	2.8	0.083
4.0	*Non*	6.3	5.8	0.11
4.7	*P*	15	16	0.33
	S	12	12	0.30

exist before irradiation. The coverage of NO monomers will initially increase with N_{ph} by photodissociation of NO dimers, $(NO)_2 \rightarrow 2NO$, and then decrease with the depletion of NO dimers. Also, the bi-exponential fitting does not include photoinduced association, $2NO \rightarrow (NO)_2$. However, this reaction path is minor compared to others and can be disregarded here.

No PID signal at m/e = 60, i.e., of NO dimers was observed from the pre-annealed Ag(111) at $h\nu$ = 4.7 eV. This suggests that all NO dimers dissociate before desorption, or that all photodesorbed NO dimers are dissociated before being detected by the QMS.

Mass selected time-of-flight of NO

The T_t and the yield of photodesorbed NO were measured by the mass selected TOF method. Fig. 3.6 shows the TOF spectra of NO from Ag(111) dosed with NO at 75 K and irradiated with 3.5 eV photons in *p*-polarization. The traces (a), (b) were measured for the numbers of laser shots (accumulated numbers of photons, $\times 10^{18}$ cm^{-2}) between the 1st and 100th (0.03 – 3), and between the 1001st and 1500th (33 – 49), respectively, and normalized by the irradiances. The shift of peak time of the TOF spectrum to shorter times at larger irradiance is noticeable. The spectra were deconvoluted by two shifted Maxwell-Boltzmann distributions (see details in Chapter 2) and the T_t were calculated for the fast (slow) component, yielding 660 K (41 K) and 890 K (82 K) for traces (a) and (b), respectively. The relative fluxes of the fast and the slow components are 0.88 : 0.12 and 0.85 : 0.15 for traces (a) and (b), respectively. The fast component is relevant to

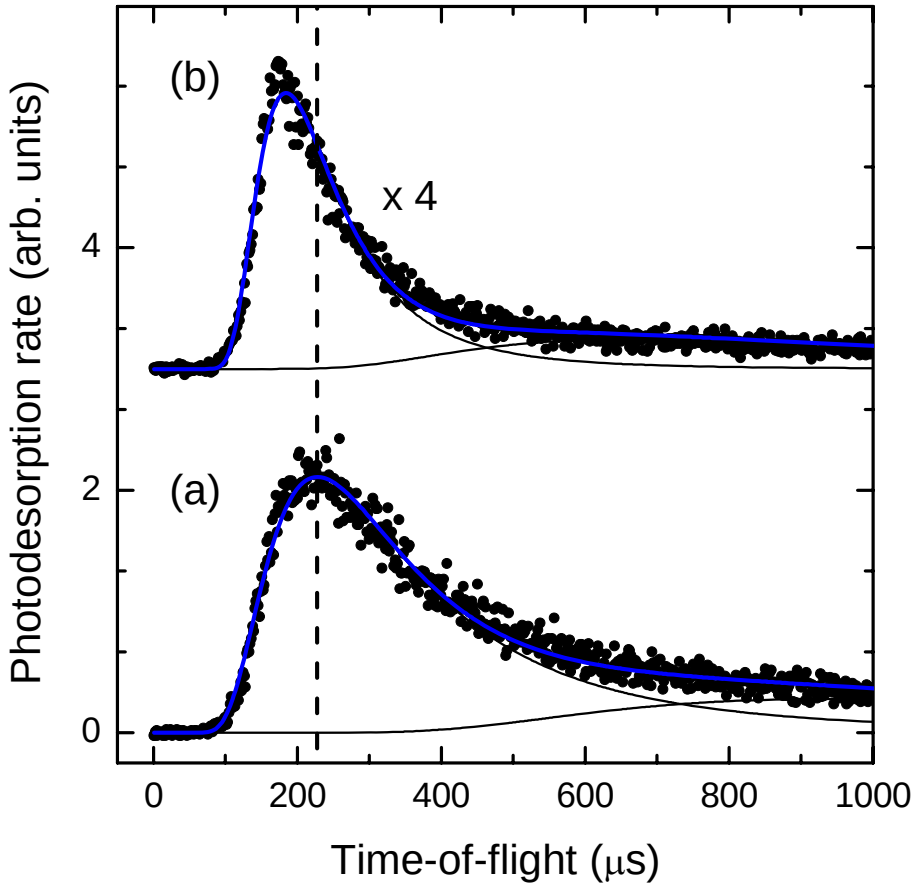

Fig. 3.6. Time of flight spectra of NO photodesorbed from Ag(111) hν = 3.5 eV in *p* polarization with a laser fluence of 1.8 mJ/cm^2 accumulated for numbers of laser shots (accumulated number of photons, ×10^{18} cm^{-2}): (a) 1 - 100 (0.003 - 0.3) and (b) 1000 - 1500 (3.3 - 4.9), respectively. The intensity of trace (b) was magnified by 4 times and shifted for clarity. The thick curves are the best fit by the sum of two shifted Maxwell-Boltzmann functions (thin curves). The dashed line is to guide the eye.

photodesorption of NO, whereas the slow component is attributable to secondary processes such as collisions among adsorbates/desorbates and with the walls of the flight tube. Laser induced thermal desorption should be negligible for the irradiance used in this measurement (1.8 mJ/cm^2). The speed ratio [95] S was found to be 1.2 for trace (a) and 0.86 for trace (b), which indicates that the fast component in trace (a) is broader and that in (b) is narrower than the normal Maxwell-Boltzmann distribution (S = 1), respectively.

Fig. 3.7 displays the evolution of T_t of the fast component in the TOF spectra of photodesorbed NO as a function of the number of photons (N_{ph}) at various photon energies. The solid, open, and half symbols correspond to *p*-, *s*-, and *non*-polarized light, respectively. The small symbols show the results measured for NO dimer-covered

Ag(111) dosed with NO at ~ 75 K and kept at ~ 30 K during photoirradiation at various photon energies. The large solid circles show those measured for NO monomer-covered Ag(111) dosed with NO at ~ 75 K and kept at ~ 130 K during photoirradiation at 4.7 eV (cf. Fig. 3.1). The solid circles with a white cross correspond to the data measured for NO monomer-covered Ag(111) dosed with NO at 75 K and annealed to 300 K, then kept at ~ 30 K during photoirradiation at 4.7 eV.

At $h\nu$ = 2.3 eV (triangles), T_t slightly increases with N_{ph} from ~ 570 K to ~ 650 K. The initial values of T_t can be extrapolated to 550 – 650 K. At $h\nu$ = 3.5 (squares), 4.0 (diamonds), and 4.7 eV (circles), T_t increases from ~ 600 K and levels off around 900 K. The initial rise in T_t becomes faster with increasing photon energy, in accord with the

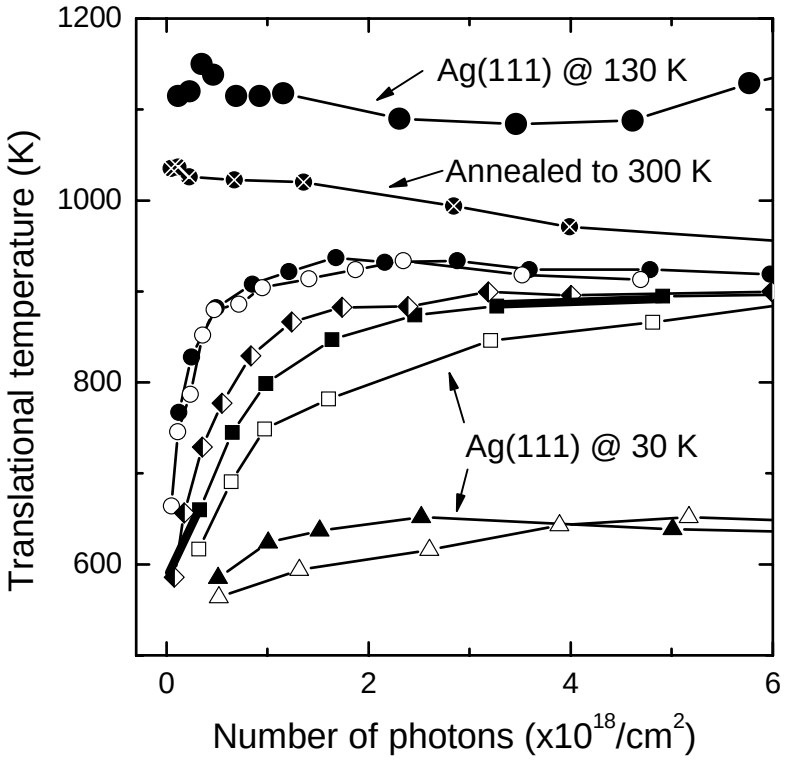

Fig. 3.7. Evolutions of translational temperatures of the fast component of photodesorbed NO from NO/Ag(111), measured at 2.3 (triangles), 3.5 (squares), 4.0 (diamonds), and 4.7 eV (circles), respectively. The solid, the open, and the half symbols correspond to *p*-, *s*-, and non-polarized light, respectively. The small symbols represent the data from Ag(111) dosed with NO at 75 K (i.e., covered with NO dimers only) whereas the solid crossed circles are the data from Ag(111) dosed with NO at 75 K and annealed to 300 K to remove NO dimers. The sample temperatures were 30 K for the above data. The large solid circles correspond to data measured at 4.7 eV at the sample temperature of 130 K (i.e., covered with NO monomers and oxygen atoms only). The lines between symbols are to guide the eye; data points at higher photon numbers exist.

PCS (cf. Table 3.2). The two thick bars between the data points at $h\nu$ = 3.5 eV in *p*-polarization (solid squares) show the segments of N_{ph} for the TOF spectra in Fig. 3.6 (the starting point at N_{ph} = 0 is extrapolated.). The segments $N_{ph} \leq 0.3 \times 10^{18}$ cm^2 and $3.3 \times 10^{18} \leq N_{ph} \leq 4.9 \times 10^{18}$ cm^2 correspond to the traces (a) and (b) in Fig. 3.6, and thus to photodesorption of NO stemming mainly from NO dimers and NO monomers, respectively.

For the 300 K preannealed NO monomer/Ag(111) surface irradiated with 4.7 eV photons, T_t decreases slowly from ~ 1040 K to ~ 950 K (large solid circles with a cross). It is therefore concluded from the comparison beween the NO dimer and the NO monomer covered Ag(111) surfaces that the characteristic T_t of photodesorbed NO from NO dimers is ~ 600 K and that from NO monomers is ~ 900 K (~ 1000 K for the NO monomers annealed to 300 K). The evolution of T_t seen at the 75 K dosed NO/Ag(111) sample reflects the gradual change of the surface reactants from NO dimers to NO monomers. The T_t can be regarded as the average translational temperature weighted by the coverages of NO dimers and monomers. This means that T_t can be used as a semi-quantitative in-situ relative coverage parameter.

From T_t measured for the sample kept at 130 K (the large solid circles), it can be concluded that T_t for pure NO monomers is ~ 1100 K. The T_t for the sample annealed to 300 K (the solid circles with a cross) suggests that some of the NO monomers dimerize when the sample is cooled to ~ 30 K. The gradual decrease of T_t for this case results from photoreaction of NO monomers to form NO dimers.

3.1.4. Direct formation of N_2 by photoinduced abstraction reaction within NO dimers on Ag(111)

The photochemical formations of dinitrogen (N_2) in addition to N_2O from NO dimers adsorbed on Ag(111) are investigated. Fig. 3.8 displays PID signals as a function of photon irradiance, i.e. while the initial $(NO)_2$ coverage was converted to products. The signal intensities were corrected by the QMS sensitivities at corresponding mass numbers. The NO signal measured at a substrate temperature (T_{sub}) of 30 K decays initially as the reactant NO dimers are consumed. Later it decays more slowly, when the NO dimers are depleted and photoproduct NO monomers become the main reactant. This is corroborated by the NO signal measured at T_{sub} = 130 K where only NO monomers exist on the surface (see Fig. 3.1). The slopes of signal decays of N_2O, N_2, and O_2 (T_{sub}=30 K) are almost the same as that of NO in the early stage. The similarity in decays of the PID signals indicates that these photoproducts are formed from single-photon photoreactions of $(NO)_2$. The initial short plateau seen in the N_2O signal is attributable to the accumulation of photoproduct N_2O on the Ag surface which is depleted by subsequent photoirradiation.

A similar PID signal of N_2 from NO adsorbed on Ag(111) at 85 K has been reported before [62]; however, it was ascribed to the fragmentation of photodesorbed N_2O and NO in the QMS. By contrast, the intensity of the N_2 signal in Fig. 3.8 is about half that of N_2O, which is significantly larger than the cracking pattern of the QMS, and does not exhibit the initial plateau seen in the N_2O signal.

Fig. 3.9 shows the TOF spectra of these molecules accumulated for an irradiance of 2×10^{18} (2×10^{17} for NO) photons/cm^2. One immediately notices that the TOF peak in the N_2 data (Trace A) appears much earlier and is narrower than those of the other species. In contrast, the peak in the TOF spectrum of N_2 photodesorbed from a monolayer of N_2O on Ag(111) at 71 K (Trace B) occurs later, and is similar to the shoulder in Trace A. The translational temperature of the fast component of N_2 (the peak in Trace A) is about 5700 K, whereas those of N_2 (Trace B), O_2, N_2O, and NO are 1200, 810, 1200, and 770 K, respectively.

The photon energy dependence of the TOF spectra of N_2 from Ag(111) with the saturation coverage of NO dosed at 75 K, subsequently cooled down to ~ 30 K is shown in Fig. 3.10. Extremely fast N_2 signals were also observed for incident photon energies 2.3 and 3.5 eV. When the spectra were deconvoluted by three shifted Maxwell-Boltzmann distributions, the T_ts for the fast, middle, and slow components were independent of photon energy and were 5700 K, 1100 K, 40 K for 2.3, 3.5 and 4.7 eV laser irradiation, respectively. The slow component can be ascribed to the secondary processes as mentioned before. The speed ratios [95] S for the each component were also independent of irradiated photon energy and were 0.47, 1.25, and 1.30 for the fast, middle, and slow components, respectively. The relative fluxes of the fast, middle and slow components were 0.63 : 0.30 : 0.07, 0.62 : 0.30 : 0.08, and 0.60 : 0.35 : 0.05 for 2.3, 3.5 and 4.7 eV laser irradiation, respectively. Thus, there are almost no differences in the branching ratio and photodesorption dynamics among these photon energies. This suggests that the N_2 is formed via the same excited states of $(NO)_2$ even at 2.3 eV photon energies.

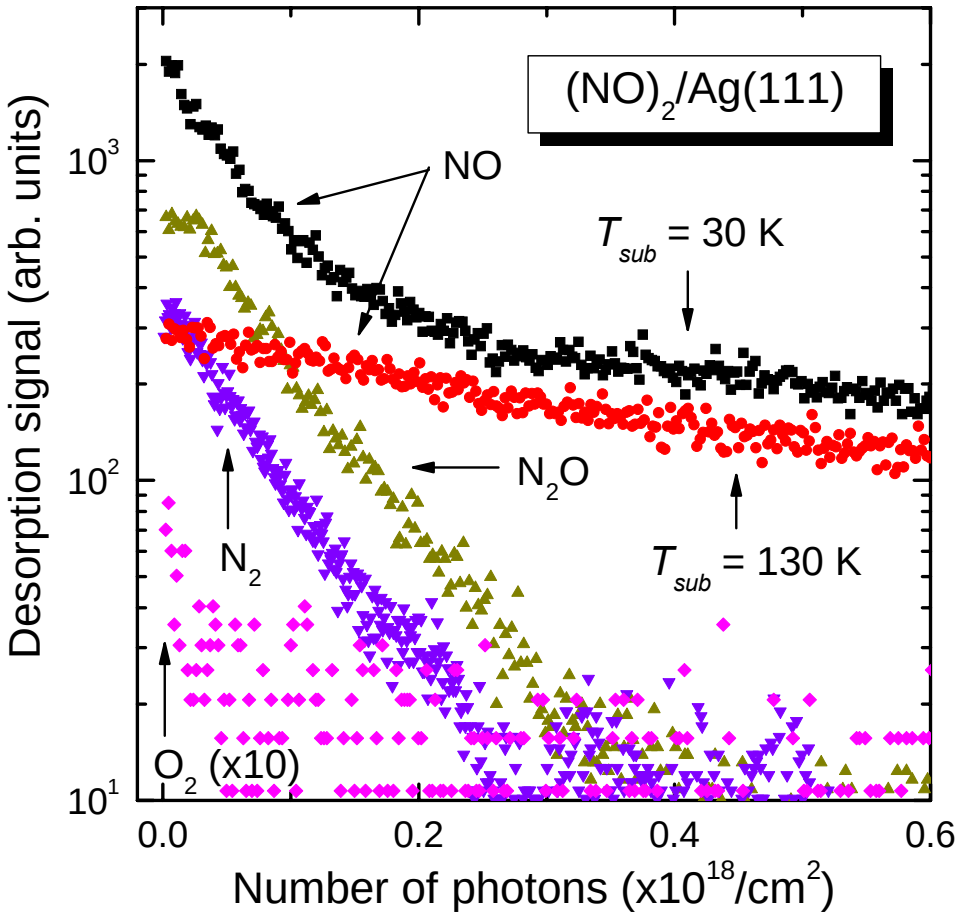

Fig. 3.8. PID results of NO, N_2O, N_2, and O_2 from Ag(111) with the saturation coverage of NO dosed at 75 K, subsequently cooled down to ~ 30 K (closed symbols) or annealed to ~ 130 K and kept at that temperature (open square), measured at 4.7 eV in *p*-polarization. The signal intensities were corrected by the number of irradiated photons and the QMS sensitivities at corresponding mass numbers.

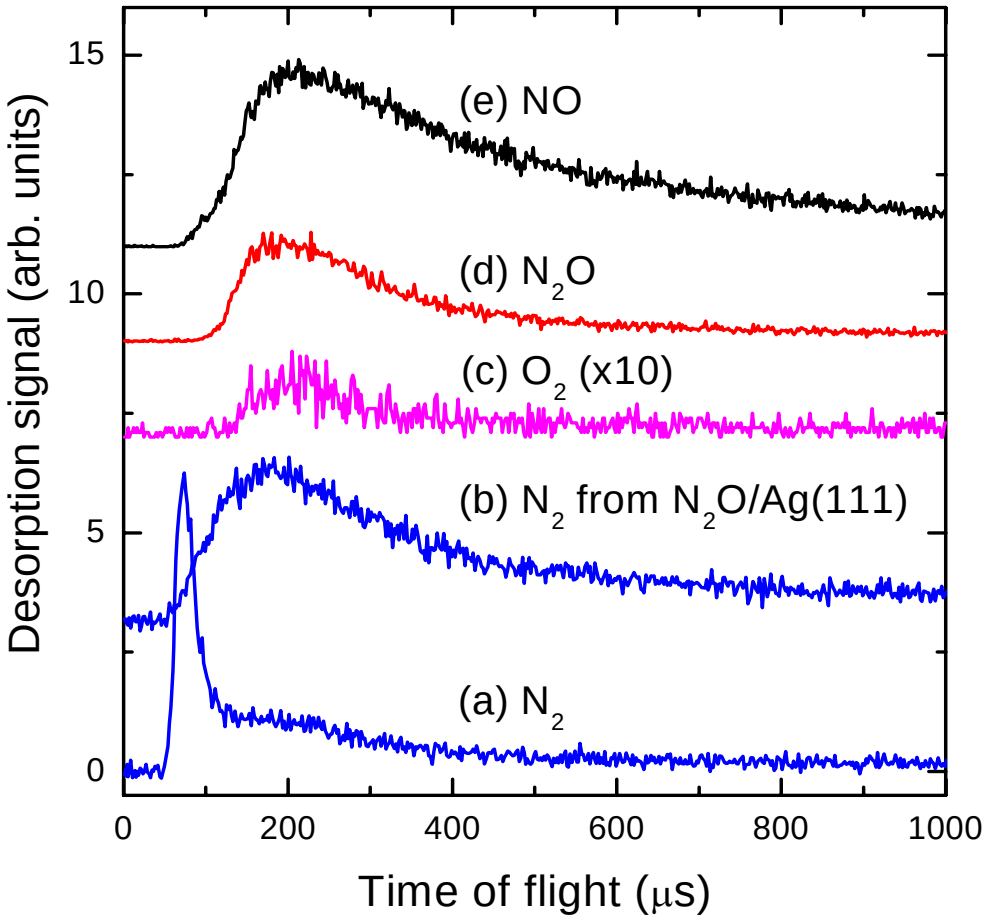

Fig. 3.9. Time of flight spectra of photoproducts desorbed by 4.7 eV, *p*-polarized laser irradiation of $(NO)_2$/Ag(111) (Traces (a), (c) - (e)) and N_2O/Ag(111) (Trace (b))

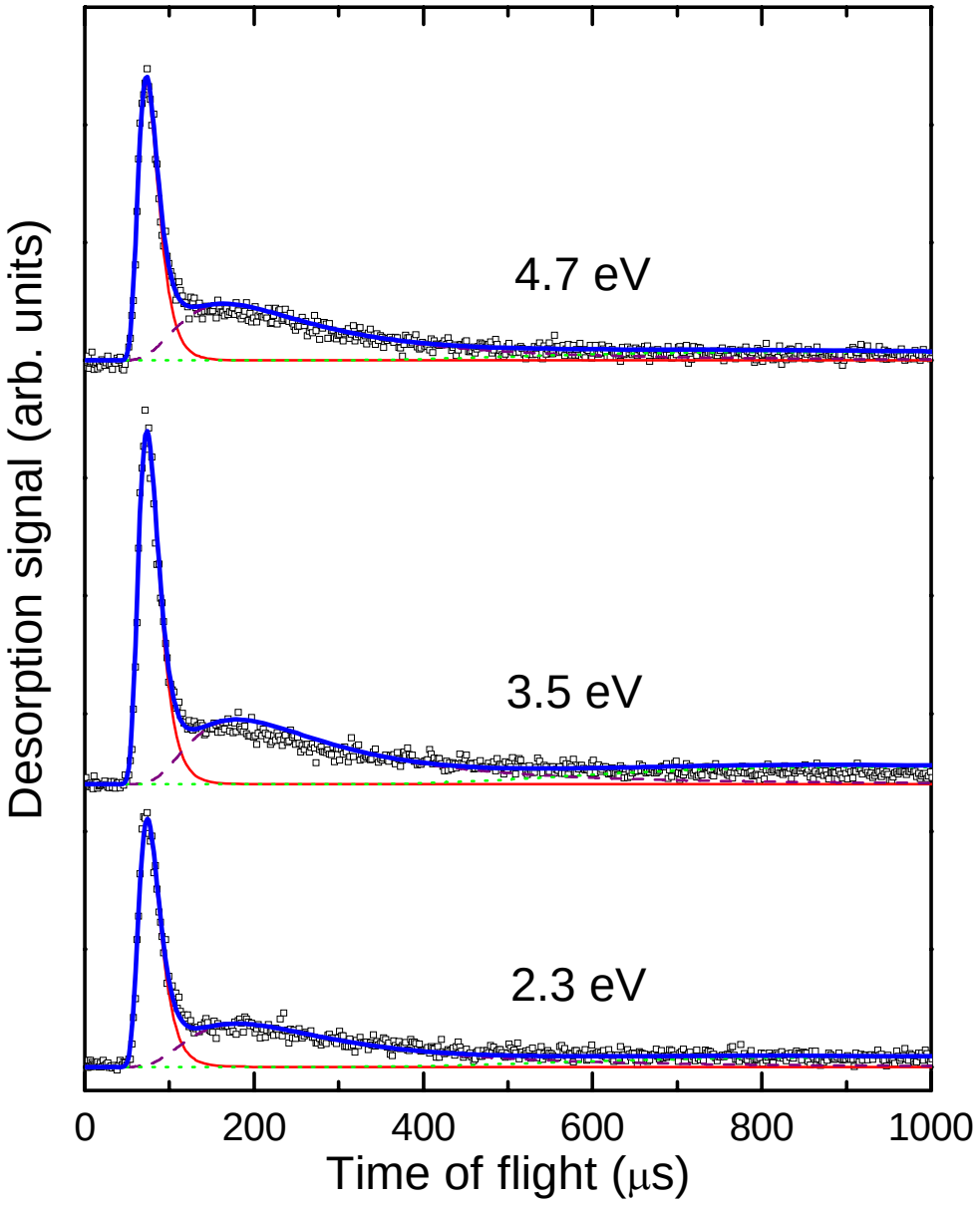

Fig. 3.10. Time of flight spectra of N_2 from Ag(111) with the saturation coverage of NO dosed at 75 K, subsequently cooled down to ~30 K, measured at 2.3, 3.5 and 4.7 eV in *p*-polarization. The signal was accumulated for 2 × 10^{18} photons/cm^2. The thick solid curves are the best fit by the sum of three shifted Maxwell-Boltzmann functions. The thin solid curves (fast), dashed curves (middle) and dotted curves (slow) represent each of the functions.

3.1.5. Discussion

Photoreaction pathways

As was shown above, NO species on Ag(111) undergo not only photodesorption but also photoinduced interconversion between dimers and monomers of NO, and photochemical reactions to form N_2 + 2O and N_2O + O. The coexistence of several adspecies complicates the analysis of the photodesorption data. Furthermore, strong coverage-dependent inter-adsorbate interactions significantly influence the photochemical properties of the adsorbates. The biggest problem is that the thermal reactions during post-irradiation TPD inevitably lead to loss of information about the photoproducts. Keeping these difficulties in mind, we discuss photoreaction pathways of each NO species in the following.

NO dimers. According to the photoproducts observed in post-irradiation TPD, mass selected PID and TOF, the possible photoreactions of NO dimers are summarized as follows:

$$(NO)_2(a) \rightarrow r\ NO(g) + (2 - r)\ NO(a) \quad (0 < r < 2) \tag{3.1}$$
$$(NO)_2(a) \rightarrow N_2O(x) + O(x) \tag{3.2}$$
$$(NO)_2(a) \rightarrow N_2(x) + 2O(x) \tag{3.3}$$

Some of these photoproducts desorb (x = g) and others remain on the surface (x = a).

Photodesorption of NO is explained by (3.1), the dissociation of the N-N bond emitting NO(g) into the gas phase and/or producing NO(a) on the surface. The ratio between NO(g) and NO(a) can be written as r : (2 - r), which is, however, not readily determined because of the thermal conversion of NO(a) during TPD measurements.

N_2O is produced from NO dimers by (3.2), the photosynthesis to form N_2O and O. Also in this case, there are two possibilities: the product N_2O is either desorbed (g) or adsorbed (a) on the surface after formation. N_2O(g) was clearly observed by the PID and TOF measurements in accordance with the previous studies by the groups of Ho and Meech in which the action spectra of NO and N_2O photodesorption track each other [49, 62], indicating (3.1) and (3.2) share the same primary excitation [118]. The formation of N_2O(a) should also be possible. However, it is not possible to distinguish by post-irradiation TPD a photochemically produced N_2O(a) from one formed by thermal decomposition of remaining NO dimers occurring in the TPD measurements, because both reactions give the same products. Thus, post-irradiation TPD of N_2O cannot be used to measure the coverage of photochemically produced N_2O. On the other hand, the

HREELS (High Resolution Electron Energy Loss Spectroscopy) data by Ho et al. suggest an increase of the coverage of N_2O by photoirradiation; in the data presented in Ref. [62], the peak at 271 meV, assigned to the N-N stretching vibration of N_2O, was increased more than twice by irradiation, although it was not mentioned explicitly.

The photoreaction (3.3) accounts for the direct formation of N_2 from NO dimers on Ag(111) for photon energy ≥ 2.3 eV, shown in Fig. 3.8 - Fig. 3.10. On the other hand, N_2 is also formed by photodissociation of N_2O(a) from reaction (3.2), proven by separate measurement of N_2O on Ag(111) adsorbed at ~ 71 K with photon energy ≥ 4.0 eV (will be shown in section 3.2),

$$N_2O(a) \rightarrow N_2(x) + O(a) \qquad (3.4)$$

However, the two reaction pathways can be easily distinguished by mass selected TOF as shown in Fig. 3.9 due to quite different dynamics of N_2 from reaction (3.3) and (3.4). The details of reaction (3.4) will be presented in section 3.2.

NO monomers. The photodesorption of NO from Ag(111) dosed with NO at 75 K and annealed to 300 K indicates that the NO monomer is also photoactive, which agrees with Ref. [113] but disagrees with Ref. [118]. Photodesorption of NO from the NO monomers is distinguished by its higher T_t (~ 900 – 1100 K) than that from dimers (T_t = ~ 600 K). NO monomers simply photodesorb by

$$NO(a) \rightarrow NO(g) \qquad (3.5)$$

NO monomers also dimerize photochemically, as is evidenced by the appearance of an N_2O peak in the post-irradiation TPD from the 300 K pre-annealed NO/Ag(111). A likely reaction mechanism is the following (The asterisk denotes an energetic species which undergoes a further reaction):

$$NO(a) \rightarrow NO^*(a) \qquad (3.6)$$
$$NO^*(a) + NO(a) \rightarrow (NO)_2{}^*(a) \qquad (3.7)$$
$$(NO)_2{}^*(a) \rightarrow (NO)_2(a) \qquad (3.8)$$

N_2O(a) is either formed by the thermal reaction of the $(NO)_2$(a) produced by (3.8) or by a reaction of the energetic NO dimer of (3.7),

$$(NO)_2{}^*(a) \rightarrow N_2O(a) + O(a \text{ or } g) \qquad (3.9)$$

The re-formation of NO dimers (3.8) may explain why the increase of T_t in Fig. 3.7 is generally slow compared to the initial decay of the PID signal (i.e. decrease of NO dimers) at $h\nu \geq$ 3.5 eV in Fig. 3.4. Since T_t of photodesorbed NO is the coverage-weighted average of the contributions from NO dimers (T_t = ~ 600 K) and monomers (T_t = ~ 900 K), the increase of T_t will be slowed down when the processes (3.6) – (3.8) compete with (3.1). Note that (3.7) is a second-order reaction of NO(a). Therefore, the dimerization of NO(a) will become less efficient as its coverage is reduced. The evolution of T_t results from the balance of the photoreactions of NO dimers and monomers on Ag(111) mentioned above.

Photoexcitation mechanisms

We discuss the photoexcitation mechanisms of the NO dimers and monomers by comparing the PCS with calculated surface absorbances. The groups of Ho [62] and Meech [49] have already confirmed that the substrate mediated mechanism plays the major role according to the action spectra of NO photodesorption. However, in view of several disagreements between the two groups mentioned above, it is still of interest to check if there is any difference between their and our results. In their previous studies, the Ag(111) was most probably covered with a mixture of N_2O and O as well as $(NO)_2$ and NO because the base sample temperature was above liquid nitrogen temperature. In contrast, we used liquid-helium cooled Ag(111) surfaces covered with $(NO)_2$ only, so that coadsorption effects are avoided at least in the early stages of photoreaction.

In Fig. 3.11, the PCS data of NO from Ag(111) dosed with NO at 75 K are plotted as functions of photon energy. The filled, the open, and the half-filled circles correspond to the data from Table 2 for *p*-, *s*-, and *non*-polarized light, respectively. The curves are effective absorbances of Ag surfaces calculated by the equation used in Refs. [62] and [49], which take into account the penetration depth of light and the mean free paths of photoelectrons, $A(E) = \left(1 - R_{eff}(E)\right)\left(1 - e^{-\alpha(E)\Lambda}\right)$, where $\alpha(E)$ is the wavelength-dependent absorption coefficient of the metal and Λ is the electron mean free path, set to 10 nm [49, 62] (the classical model, hereafter). The solid curves were calculated for non-polarized light by using the optical constants tabulated in [48], respectively. The dashed and dotted curves correspond to *p*- and *s*-polarized light calculated after ref [48]. The action spectra measured with *non*-polarized light by Ho [62] and Meech [49] are also plotted as " ×" and "+", respectively. The absorbances and the action spectra were rescaled according to the average value of photodepletion cross sections for *p*- and *s*-polarizations at 3.5 eV. The light incident angle was 45 degrees (40 degrees in Ref. [62], a negligible difference).

The surface effective absorbance curves calculated after Ref. [48] show significant discrepancies - up to 85 % - between 2.0 and 3.4 eV and between 3.8 and 4.0 eV. If the action spectra are rescaled according to the curve at a lower photon energy as in Ref. [62]

and [49], a large deviation results at higher photon energies; In fact, this deviation was explained in terms of the involvement of direct excitations of the adsorbate-substrate complex [62]. Nevertheless, the polarization dependence of the PID signal intensity did not show any evidence of the direct excitation mechanism [49]. In spite of the variations in the optical constants, however, the classical model can reproduce the overall trend of the experimental data.

The probability of electron attachment-induced reactions of the adsorbate is thought to be dependent on three energy-dependent factors [49]: The hot electron distribution at the surface, the electron tunneling probability, and the electron attachment levels of the adsorbates [119]. The good agreement between the classical model and the PCS data supports the substrate mediated excitation mechanism for the NO dimers at $h\nu > \sim 2$ eV, although it precludes the determination of these factors.

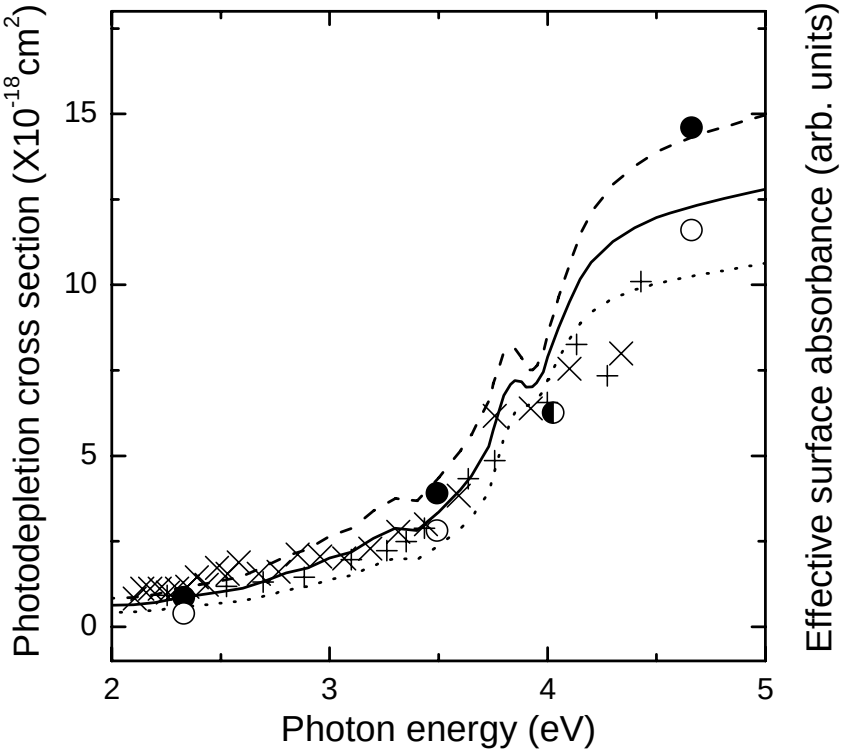

Fig. 3.11. Photodepletion cross sections (circles) of NO from Ag(111) saturated with NO at 75 K. The filled, the half-filled, and the open circles correspond to the data measured with *p*-, *non*-, and *s*-polarized light, respectively. The "x" and "+" show the action spectra (initial PID intensities) of NO photodesorbed from Ag(111) dosed with NO at 80 - 86 K by Ho et al. [62] and Meech et al. [49], respectively. The solid, the dashed, and the dotted curves plot the effective surface absorbances (see text) for *non*-, *p*-, and *s*-polarized light, respectively. All datasets were scaled at 3.5 eV.

The excitation mechanism for the NO monomers can be discussed based on the σ_s in the bi-exponential fitting of the PID data shown in Table 3.2, though we recall that σ_s is not a very reliable parameter. Above the onset of the photoreactions of NO monomers at ~ 3.5 eV, σ_s generally increases with photon energy as in the classical model and there seems no resonance-like feature. Thus, it is likely that the substrate mediated excitation plays a major role also in the photochemistry of NO monomers on Ag(111). The photoexcitation of monomeric NO on metal surfaces such as Pt and Pd in the UV range is generally interpreted by the substrate mediated excitation mechanism [2].

As mentioned earlier, the adsorption states of the NO monomers on Ag(111) are perturbed by the oxygen atoms produced by the reaction (3.2). The discrepancy in the affinity level of the NO monomer between the experiments and the theoretical calculations [118] can be partly explained in terms of the perturbation by oxygen atoms in the experiments. Meech et al. showed that NO monomers (NO-β) are perturbed by neighboring oxygen atoms to various extents depending on the local adsorption structures of coadsorbed oxygen [113]. They also showed that some of NO monomers are photoinert even at 4.7 eV. This is probably due to the higher concentration of oxygen atoms on their sample than ours.

Photoreaction mechanisms

Photodesorption of NO originates from several reaction pathways. It originates from photodissociation of NO dimers on Ag(111) as in (3.1). Photodesorption of NO from the NO monomers is understood as dissociation of the N-Ag bond. Both cases can be explained by the excitation/deexcitation mechanisms in terms of the MGR or Antoniewicz models, which have been frequently used in general for photodesorption of NO from metal surfaces. In the framework of the substrate mediated excitation mechanism, the photoreactions of the NO dimers and the monomers take place via a transient negative ion (TNI) state. The fact that the T_t of NO from NO dimers and monomers are insensitive to the photon energy indicates that the same TNI states are accessed by the photon energies from 2.3 to 4.7 eV.

The direct formation of N_2 from NO dimers on Ag(111), was clearly shown in Fig. 3.8 - Fig. 3.10. This photoreaction channel has not been identified before, neither on solid surfaces nor in the gas phase. For the mechanisms of the photoproducts, i.e., NO, N_2O, N_2 from $(NO)_2$, we suggest the following scenario. The resonance orbital responsible for the photoreactions has antibonding character for both the ON-NO and the N-O bonds [118]. With this orbital being populated by an electron, both the ON-NO and the two N-O bonds will start to elongate. When the weak ON-NO bond (bond energy 700 cm^{-1}) [120-122] is broken first, two NO molecules desorb; this is the most efficient path as shown by the yields in Fig. 3.8. If one of the N-O bonds is broken earlier than the ON-NO bond, the

N atom is abstracted by the other NO and an N-N double bond is formed to produce N_2O (NNO). When the two N-O bonds split simultaneously, the two nitrogen atoms abstract each other to form dinitrogen, N_2. No atomic nitrogen is deposited on the Ag surface, as evidenced by the absence of N_2 formed by its thermal recombination [113]. Theoretical calculations [118, 123] show that by adsorption of a free $(NO)_2$ onto Ag(111) its N-N bond is contracted from 2.26 Å to ~1.63 Å, whereas the N-O bond is stretched from 1.15 Å to ~1.21 Å. Thus, the N-N bond formation becomes feasible for the adsorbed $(NO)_2$.

Once an N_2 is formed from an adsorbed $(NO)_2$, it finds itself on a very steep repulsive potential since it is too close to the surface. The height of the N atoms in an $(NO)_2$ molecule on Ag(111) is 2.11 – 2.27 *Å* [124], whereas the equilibrium distance between N_2 and Ag(111) is 3.68 Å [124]. The resulting strong repulsion causes the extremely high translational temperature (~ 5700 K) of the photodesorbed N_2.

An interesting question poses itself regarding the oxygen atoms which have to be produced in the photoreaction to N_2. They could remain on the surface or be photodesorbed as well. As to the split-off oxygen, only a small part photodesorbs by associative recombination to form O_2 (see Fig. 3.8 and Fig. 3.9), and only with 3.5 and 4.7 eV irradiation, but not with 2.3 eV. The initial decay of this weak signal is steeper than those of the other products. This indicates that the molecular O_2 signal stems from secondary processes between nascent and/or adsorbed oxygen atoms, $O^* + O^* \rightarrow O_2$ and/or $O^* + O(a) \rightarrow O_2$, and not from a first-order process of the NO dimers, $(NO)_2 \rightarrow N_2 + O_2$. The signal of photodesorbed atomic oxygen (mass 16) was below the detection limit at all the photon energies, which could still be a detection problem due to its high sticking probability on the ion source walls. However, the splitting-off of two O atoms from the NO dimers is thermodynamically impossible at 2.3 eV; an estimate based on heats of formation shows that splitting off two O atoms from the NO dimers would cost at least 3.4 eV i.e., not possible for 2.3 eV photons, and even for 3.5 eV photons would require that almost all the excitation energy would be channeled into the desorptive fragmentation. These results suggest that the majority of oxygen atoms produced by N_2 formation from $(NO)_2$ are adsorbed on the silver surface; some may go subsurface upon heating

More detailed information about photodesorption mechanisms of NO and N_2 may be obtained by state-resolved methods such as LIF and REMPI. In particular, the REMPI is able to probe NO dimers, which were not detected in the present study.

3.1.6. Summary and conclusions

The combination of TPD, PID, and mass selected-TOF measurements were used to reveal photoreactions of NO dimers and monomers on Ag(111). Photoreactivities and photodesorption dynamics of each NO species have been studied selectively by controlling their adsorption states. The main results and conclusions are summarized below.

(1) The affinity levels (E_a) of the NO dimers and monomers are determined as follows: The E_a of the NO dimer is situated below 2.3 eV. That of the NO monomer is higher than 2.3 eV and situated partially below 3.5 eV, and lower than 4.0 eV. The latter can be shifted above 4.7 eV by the perturbation of coadsorbed oxygen atoms.

(2) NO molecules photodesorbed from NO dimers and monomers are characterized by translational temperatures of ~ 600 K and 900 ~ 1100 K, respectively. Photodepletion cross sections of each species have been measured as a function of photon energy. They are in agreement with the substrate mediated excitation mechanism.

(3) Direct photochemical formation of N_2 has been identified for the first time in photoreactions of $(NO)_2$ adsorbed on cold Ag(111), induced by UV and visible light. We propose that this reaction occurs via simultaneous cleavage of the two N-O bonds followed by the formation of an N-N triple bond of N_2, and can be regarded as mutual abstraction of the N atom from each nitrosyl in $(NO)_2$. The Ag surface serves as reducing the N-N bond length of $(NO)_2$ to enable the formation of N_2 as well as N_2O.

3.2. Dynamics and excitation mechanisms of N_2O and N_2 photodesorbed from N_2O on Ag(111)

This section provides nanosecond-laser-induced photoreactions of N_2O adsorbed on Ag(111) by means of TPD and mass-selected TOF and PID measurements. It is shown that N_2O molecules in the first monolayer are thermally inert but photodissociate into N_2 + O or photodesorb molecularly at photon energy $h\nu \geq 3.5$ eV. The desorption flux of the fastest component of N_2O is peaked ~ 25° off the normal, whereas the others are directed at the surface normal. Origins and photodesorption mechanisms of the N_2O and N_2 are discussed.

3.2.1. Introduction

N_2O is known as the important intermediate in automobile catalysts for NO_x reduction to form N_2, and molecular-level studies have been performed in catalytic NO decomposition on Pd(110) [125, 126], Rh(110) and Rh(111) [127], and TiO_2(110) [128] for example. On Pt(111) [129] and Ag(111) [130], on the other hand, N_2O does not dissociate thermally and desorbs molecularly at 80 – 90 K. However, the photochemistry of N_2O has been studied in detail on Pt(111) [131-133] as well as Si(100) [134-137]. On Pt(111), N_2O is photodissociated at photon energies exceeding 4.35 eV [131]. On Si(100), N_2O undergoes photoreactions over 2.3 eV [134]. In both cases, the photoreactions are initiated by the substrate mediated excitation [132, 134].

In contrast, photochemistry of N_2O on Ag(111) has not been reported until recently. Instead, electron stimulated dissociation of multilayer N_2O to form gas-phase N_2 and oxygen adatoms was reported by Schwaner et al [130]. They concluded that the reaction is induced by the attachment of secondary electrons produced by the primary electron beams (50 eV and 2500 eV) via N_2O^- formation. In the monolayer regime, no dissociation nor desorption of N_2O was observed; they ascribed this to the strong quenching of anions formed by attachment and cations formed by impact ionization.

Interestingly, however, N_2O is formed photochemically [113] as well as thermally [96, 114] from NO dimers on Ag(111). In the previous section, we showed that not only N_2O but also N_2 is also formed from the NO dimers under irradiation of 2.3 – 4.7 eV

photons and the kinetic energy distributions of photodesorbed N_2 and N_2O from NO dimers are very different; the translational temperatures are 5700 and 1200 K, respectively. Such a high translational energy of desorbing N_2 had never been observed for any other surfaces including Si(100). This led us to study the photochemistry of pure N_2O adsorbed on clean Ag(111), in order to distinguish whether the very energetic N_2 is formed from N_2O or $(NO)_2$.

In this section we present photoreactions of N_2O adsorbed on Ag(111). The N_2O adsorbate is photoreactive at $h\nu \geq$ 3.5 eV. N_2O either photodesorbs molecularly or dissociates into N_2 and O. The photoexcitation mechanisms are studied by light polarization and incident-angle dependences of photodepletion cross sections. Both direct and indirect (substrate-mediated) excitations are involved, depending on the photon energies. Also, photodesorption dynamics of N_2O and N_2 are studied by angle-resolved mass-selected time-of-flight measurements. It was found that the mechanism of photodesorption is not single for these species; it consists of two components with different angular distributions.

3.2.2. Experimental

Pre- and post-irradiation TPD, mass selected TOF, and PID measurements have been performed to investigate thermal- and photochemistry of N_2O on Ag(111) (disk type, 10 mm in diameter). Saturated monolayers of N_2O on Ag(111) were used for all the experiments and prepared by dosing the sample surface at 71 K with N_2O gas from a pulsed valve through a copper tube (inner diameter of ~ 6 mm) ending about 3 cm in front of the sample. The gas dosage was controlled by the number of valve openings so that the TPD peak from the first monolayer was saturated but none from multilayers emerged.

Angular dependences of the PCS and the TOF spectrum of photodesorbing molecules were measured by rotating the sample at the crossing point of the laser beam and the QMS center axis. The measurement configuration is schematically drawn in Fig. 3.12. The angle between the laser beam and the QMS axis was fixed at 45^o. Therefore, the desorption detection angle θ_{des} and the light incident angle θ_{in} with respect to the surface normal were varied under a constraint $\theta_{des} = 45^o - \theta_{in}$. This means both parameters cannot be changed independently; however, the determination of the photoexcitation mechanism and the desorption dynamics was still possible as will be shown later. The data were normalized with respect to relative sensitivities of the QMS to the target molecules (here N_2O and N_2) after subtracting the QMS cracking signal from N_2O^+ (m/e = 44) to N_2^+ (m/e

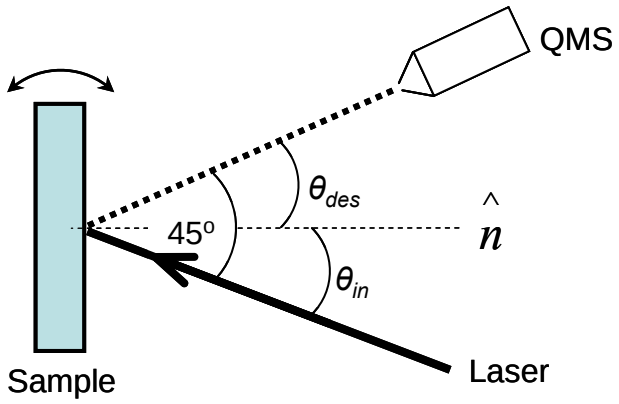

Fig. 3.12. Configuration of PID measurement. The angle between the QMS and laser beam is fixed at 45°. The direction of the surface normal is varied in the experiment by rotating the sample manipulator.

= 28). Also, a change of irradiated area on the sample surface by rotation was taken into account for the normalization.

3.2.3. Thermal- and photoreactions of N_2O on Ag(111)

Pre- and post-irradiation TPD of N_2O on Ag(111)

Fig. 3.13 displays pre- and post-irradiation TPD results at mass numbers (a) m/e = 44, (b) m/e = 28, and (c) m/e = 32 from monolayers of N_2O on Ag(111). The sample was irradiated with 5000 laser shots (1 mJ/cm^2 per shot) of 3.5 (dashed), 4.0 (thin solid), or 4.7 eV (dotted curves) photons at $\theta_{in} = 45^o$.

The pre-irradiation TPD spectrum at m/e = 44 shows only a single peak at ~ 82 K which corresponds to molecular desorption of N_2O. At m/e = 28, a replica of the signal at m/e = 44 due to cracking of N_2O at the QMS is seen. No products such as N_2 and O_2 (m/e = 32) were observed. This indicates that N_2O on Ag(111) is not thermally dissociated; this result is consistent with previous work [130]. After irradiation of 3.5 eV photons, the N_2O peak height was reduced to ~ 80 % without any shift. However, a small tail was observed from ~ 83 K to ~ 95 K as shown in inset of Fig. 3.13 (a). After 4.0 and 4.7 eV photon irradiation, the N_2O peak was shifted to ~ 102 K.

At m/e = 28, the same features were observed in the post-irradiation TPD spectra measured in the temperature range between 70 K and 120 K because of the cracking of N_2O at the QMS ionizer. However, an additional peak was observed below 60 K. This is attributable to molecular N_2. Also, at m/e=32, a recombinative desorption peak of O_2 around 540 K was observed at 4.0 and 4.7 eV. At 3.5 eV, the O_2 peak was below the detection limit most probably because of the low reaction yield of oxygen atoms. These

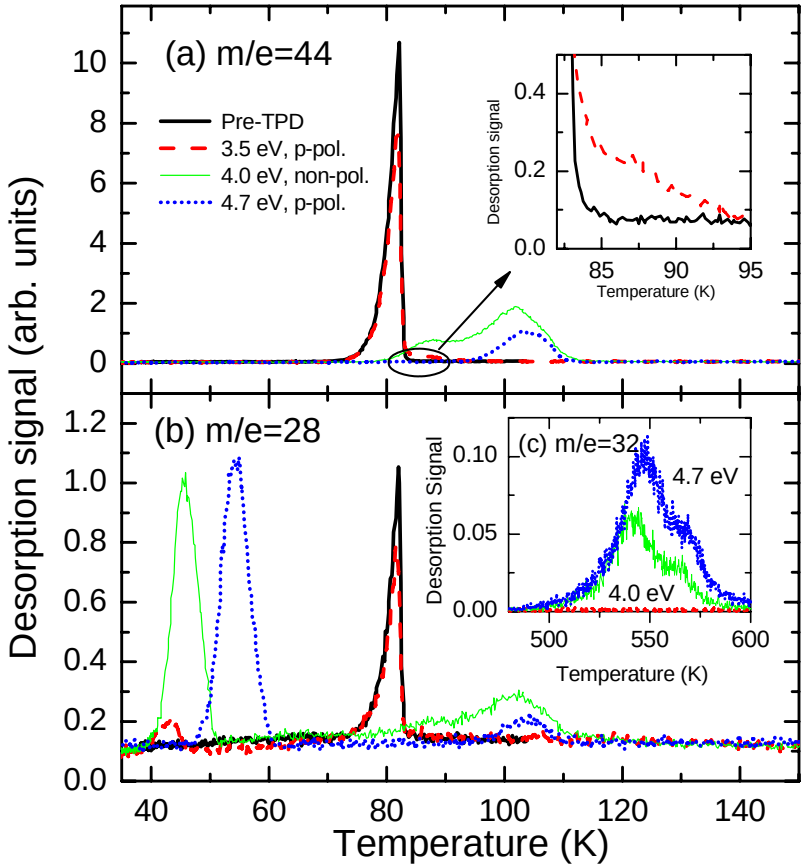

Fig. 3.13. TPD results from Ag(111) dosed with N_2O at 71 K to the saturation coverage before and after irradiation, measured at mass numbers (a) m/e=44, (b) 28, and (c) 32.

results indicate that N_2O is photodissociated at 3.5 eV or higher. The other reaction products, i.e., NO (m/e = 30), NO_2 (m/e = 46), were not observed in both pre- and post-TPD.

Mass selected time-of-flight of N_2O and N_2

Fig. 3.14 shows TOF spectra of (a) N_2O (m/e = 44) and (b) N_2 (m/e = 28) photodesorbed from a monolayer of N_2O on Ag(111) measured at desorption angles θ_{des} = -25°, 0°, 25°, and 45° by 4.7 eV photons in *p*-polarization. The desorption signals were accumulated until they were almost depleted: The necessary irradiances were ~ 1×10^{18} photons/cm^2. The N_2 signals were corrected by the relative sensitivity of the QMS after taking into account the cracking pattern of N_2O into the m/e = 28 signal. Therefore, the

N_2 signal is attributable to the photofragment N_2 produced by photodissociation of N_2O on Ag(111). The data were further normalized by the actual area on the sample irradiated with the laser beam, i.e., 61.5, 65.4, 87, and 100% at θ_{in} = 0°, 20°, 45°, and 70°, respectively.[1]

All the spectra were fitted by a sum of three modified flux-weighted Maxwell-Boltzmann functions for each mass number, where $i \leq 3$

$$F(t) = \sum_i \frac{a_i}{t^4} \exp\left(-b_i \left(\frac{L}{t} - v_i \right) \right) \tag{3.10}$$

in which a_i, b_i, and v_i are the parameters for amplitude, spread, and a shift from Maxwellian, respectively, L the distance from the surface to the detector. The data were globally fitted; common parameters b_i and v_i were shared for the data sets of all the desorption angles. Instead, the parameter a_i was optimized independently for each angle. This procedure should give the information about the angular distribution of each speed component.

The two fast components (indicated in the figure as P_1 and P_2 for N_2O and Q_1 and Q_2 for N_2) will be mainly discussed in this section. The slowest component is attributable to secondary processes such as among adsorbates/desorbates. The translational temperatures of these components are obtained as 3100, 1100, 2200, and 600 K, respectively.

The TOF spectra of N_2O in Fig. 3.14 (a) show distinct desorption angle dependences. The P_1 intensity is larger at θ_{des} = ±25° than at θ_{des} = 0°, indicating P_1 is peaked off-normal. On the other hand, the P_2 intensity is strongest at at θ_{des} = 0°. The P_1 to P_2 ratio is almost the same at θ_{des} = ±25°, as a result of the symmetry. The small variation in the intensity is probably due to errors in estimating the beam irradiated area mentioned above. It is seen that the P_1 intensity is more sensitive to θ_{des} than the P_2 intensity, indicating that the spatial distribution of the former is narrower than that of the latter. The ratios of the fluxes of P_1 to P_2 were ~ 0.92, ~ 0.15, ~ 0.93, and ~ 0.04 at θ_{des} = -25°, 0°, 25°, and 45°, respectively. The fitting of the angular dependent photodesorption fluxes of P_1 and P_2 to a $\cos^n\theta_d$ function gave n = 20 (at θ_d = 25°), and 1.7 (at θ_d = 0°), respectively.

The θ_{des} dependence of the photofragment N_2 signal in Fig. 3.14 (b) shows remarkably different features compared to those of N_2O. The desorption fluxes of Q_1 and Q_2 were the highest at θ_{des} = 0°. Q_1 is peaked more sharply than Q_2. The ratios of Q_1 to Q_2 are ~ 0.70, ~ 1.22, ~ 0.59, and ~ 0.22 at θ_{des} = -25°, 0°, 25°, and 45°, respectively. The fitting of the angular dependent photodesorption fluxes of Q_1 and Q_2 to a $\cos^n\theta_d$ function resulted in n = 12 (at θ_d = 0°), and 5 (at θ_d = 0°), respectively.

[1] Since the irradiated area on the sample varied with the θ_{in}, whole beam wass shinned on the sample surface when θ_{in} < 45°, but 44% of irradiated laser beam was out of the sample at θ_{in} = 70°. This factor was taken into account in an estimation of irradiated area.

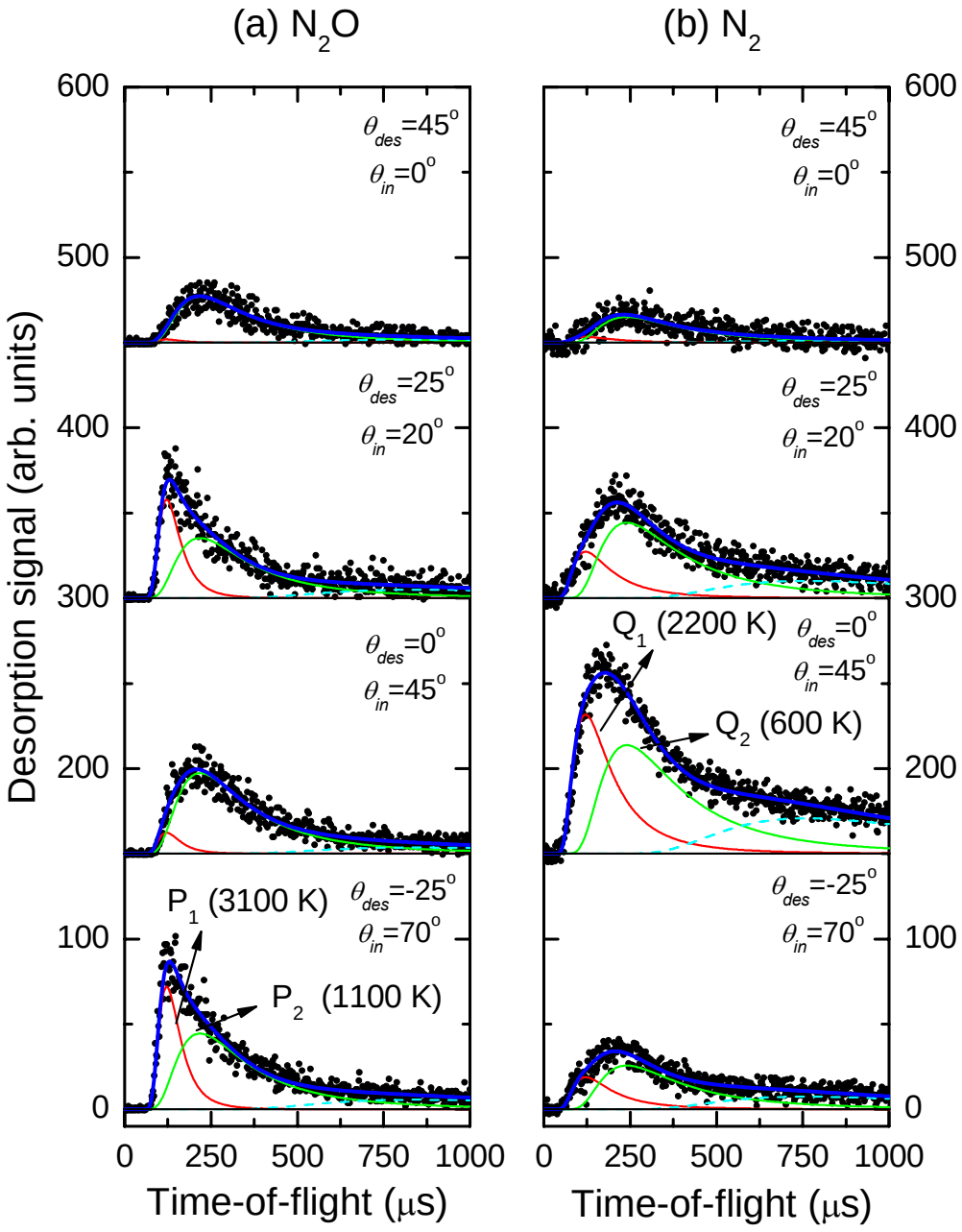

Fig. 3.14. TOF spectra of (a) N_2O and (b) N_2 photodesorbed from the N_2O monolayer on Ag(111) measured at different desorption angles, -25°, 0°, 25°, and 45° (θ_{in} = 70°, 45°, 20°, and 0°) from the bottom, by using 4.7 eV photons in *p*-polarization. The fitting results from a sum of three shifted Maxwell-Boltzmann distributions are shown with thick (sum), thin (fast component, indicated), thin (slow component, indicated), and dashed (secondary process components) curves.

TOF spectra of N_2O accumulated for (a) 1 – 25 shots and (b) 501 – 3001 shots measured at θ_{des} = -25° by irradiating with 4.7 eV photons in *p*-polarization are compared in Fig. 3.15. One laser shot corresponds to 1.1×10^{15} photons/cm^2 on the surface. In this case, fitting was done independently for the two traces. The spectral shape of each speed component is almost the same for the two traces, but the relative intensity is significantly different. The fast component is dominant at low irradiance, and it becomes minor at larger irradiances, i.e., the fast component decays faster than the slow component. This suggests that the origins of the two components are different, which is consistent with the difference in the angular dependences of them shown in Fig. 3.2.

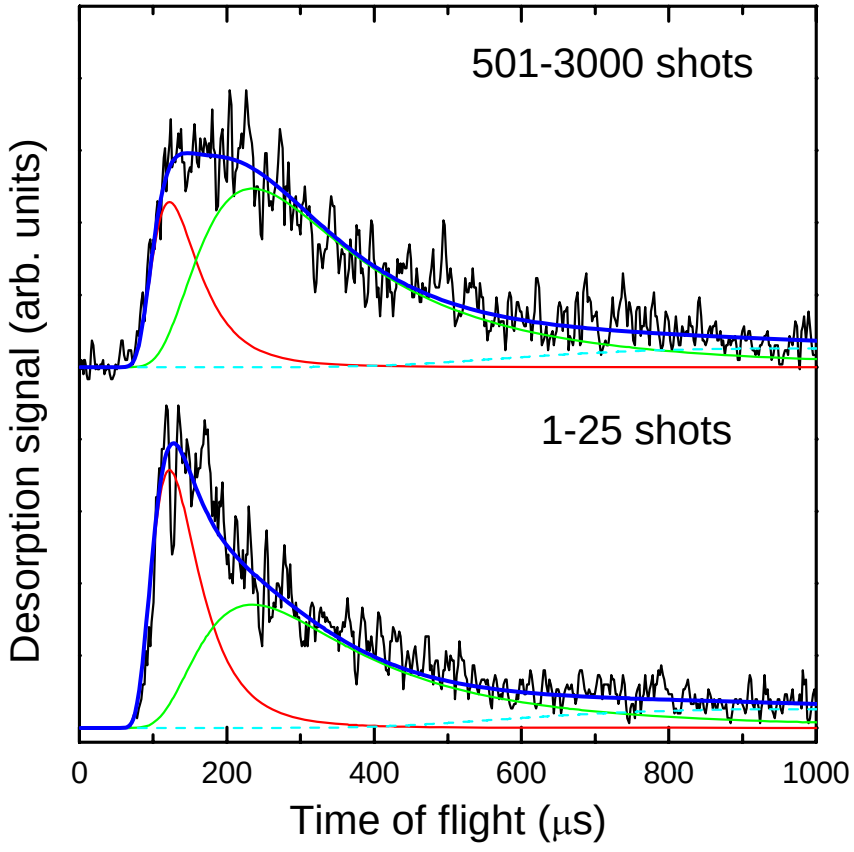

Fig. 3.15. Irradiated number of photon dependence of TOF spectra of m/e = 44 at θ_{des} = -25° by means of 4.7 eV, *p*-polarization. The fast component decays faster than the slow component.

Photoinduced desorption of N_2O and N_2

Fig. 3.16 presents the PID signal of (a) N_2O and (b) N_2 on a logarithmic scale as a function of accumulated number of photons at 4.7 eV in *p*-polarization. Each data point is an integrated ion signal of desorbed molecules for 2 ms after a single laser pulse and is normalized by the QMS sensitivity, the photon density on the sample, and the irradiated area. In the case of N_2 PID, the cracking from N_2O is also subtracted. The signal intensity and slope strongly depend on the incident angle (desorption angle). For example, the largest intensity and the fastest decay of the N_2O PID signal was observed at $\theta_{des} = -25^o$ ($\theta_{in} = 70^o$), whereas that of the N_2 signal was detected at $\theta_{des} = 0^o$ ($\theta_{in} = 45^o$).

The N_2 PID signals generally decay more slowly than those of N_2O. More interestingly, they do not decay linearly (exponentially). Rather, they start with a small rise in the early stage especially at $\theta_{des} = -25^o$ ($\theta_{in} = 70^o$) and $\theta_{des} = 45^o$ ($\theta_{in} = 0^o$). The rising N_2 signal becomes more obvious with lower laser intensity (0.2 mJ/cm^2/shot) for all desorption angles (data is not shown). This indicates that there are multiple desorption channels contributing to the overall N_2 PID signal. The initial rise is attributable to the accumulation of molecular N_2(a) produced by photodissociation of N_2O on the surface. In the early stage the N_2(a) formation rate is higher than the N_2 photodesorption rate because of the high N_2O(a) coverage. However, as N_2O(a) is depleted, the overall N_2 photodesorption rate becomes higher than the N_2(a) formation rate, resulting in the decay of the N_2 PID signal in the late stage. Simultaneously, N_2 photofragments produced by N_2O photodissociation photodesorb. The photoreactions involved in the PID of N_2O and N_2 are summarized as follows:

$$N_2O(a) \rightarrow N_2O(g) \quad (3.11)$$
$$N_2O(a) \rightarrow O(a/g) + N_2(g) \quad (3.12)$$
$$N_2(a) \rightarrow N_2(g) \quad (3.13)$$

The N_2 PID rises and decays more slowly at larger θ_{des} than at $\theta_{des} = 0^o$. This suggests that the contribution from the photodesorption of molecular N_2(a), Reaction (3.13), is larger at larger θ_{des}. In contrast, the initial rise is insignificant at $\theta_{des} = 0^o$ as shown in Fig. 3.16 (b), suggesting that the contribution from the photofragment N_2, Reaction (3.12), is dominant. Thus, photodesorbed N_2 by Reaction (3.12) is sharply peaked at $\theta_{des} = 0^o$.

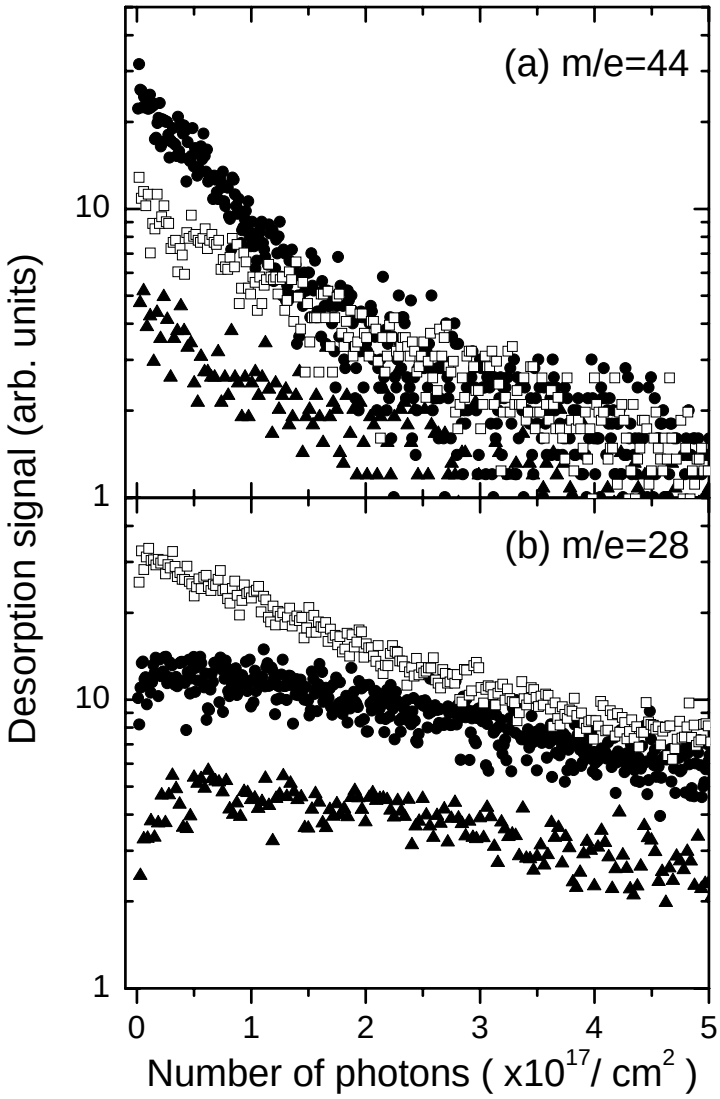

Fig. 3.16. PID of the desorption signal at incident angle θ_{in} = 70° (filled circles), 45° (open squares), and 0° (filled triangles) for (a) m/e = 44 and (b) 28 by irradiating with 4.7 eV photons in *p*-polarization.

Based on the angular dependences of the N_2 PID results, it is possible to assign the speed components in the mass selected-TOF spectra shown in Fig. 3.14 (b). As the angular distribution of Q_1 is narrower than that of Q_2, Q_1 and Q_2 can therefore be assigned to Reactions (3.12) and (3.13), respectively.

On the other hand, the N_2O PID signals decay almost linearly. By using the results of the angle-resolved mass selected-TOF measurements, however, it is still possible to differentiate the contributions from P_1 and P_2 to the PID signals. According to the mass selected-TOF spectra shown in Fig. 3.14 (a), it can be concluded that the N_2O PID data measured at $\theta_{des} = 0^o$ ($\theta_{in} = 45^o$) and $\theta_{des} = 45^o$ ($\theta_{in} = 0^o$) stem mainly from the P_2 component, whereas both P_1 and P_2 contribute almost equally to the data at $\theta_{des} = -25^o$ ($\theta_{in} = 70^o$). This can be used for the analysis of the polarization and incident angle dependences of photodesorption cross sections to determine the photoexcitation mechanisms, which will be described in the next section.

Secondary processes such as

$$O^* + N_2O(a) \rightarrow N_2 + O_2 \quad (3.14)$$
$$O^* + N_2O(a) \rightarrow 2NO \quad (3.15)$$
$$O^* + N_2O(a) \rightarrow N_2O(g) + O(a) \quad (3.16)$$

may also be possible. Reaction (3.14) is not distinguishable from Reactions (3.12) – (3.13) as far as N_2 photodesorption is measured. Measurement of O_2 photodesorption was not attempted in this study. Reaction (3.15) may be possible. For example, desorption of O_2 by a photofragment O atom is reported on O_2/Pt(112) [138], however, the formation of NO was not observed in the post-irradiation TPD.

Distinguishing photoexcitation mechanisms by incident-angle and polarization dependences of photodesorption cross sections

In order to distinguish the photoexcitation mechanisms involved in the photodesorption of N_2O and N_2, light incident angle and polarization dependences [46] of the PCS have been studied. The PCS was estimated by fitting a single exponential decay function to the PID data in the range between the maximum and the decay to the half maximum. The PCS values at 4.7 eV are summarized in Fig. 3.17. The error bars for N_2O at $\theta_{des} = \pm 25^o$ in Fig. 3.17 were estimated from a difference caused by fitting the region in the N_2O PID signal from the signal for the first laser shot to that decayed to 50 - 10 % (upper limit) and 50 + 10 % (lower limit). For the N_2O PCS data, the calculated absorbances of Ag by assuming the indirect excitation (substrate mediated excitation) are plotted as blue solid and dashed curves for *p*- and *s*-polarized light, respectively. Also, the results of the model calculations assuming the direct excitation mechanism with an angle

of 74° between the transition dipole vector and the electric field vector for the surface with ≥ C_3 rotational symmetry [46] are plotted as red solid and dashed curves for *p*- and *s*-polarized light, respectively. It is obvious that the data points cannot be fitted by a single function. For example, in the case of the PCS of N_2O measured with *p*-polarization, the PCS at θ_{in} = 45° is lower than that at θ_{in} = 20°, although both direct and indirect excitation mechanisms predict an increase of PCS for *p*-polarized light in this angular range.

Such a discrepancy is caused by the fact that the main photodesorption mechanisms of N_2O are different between θ_{in} = 45° (θ_{des} = 0°) and at θ_{in} = 20° (θ_{des} = 25°). The P_2 component is dominant in the former case whereas the P_1 component is dominant in the early stage of the latter case (See Fig. 3.14 (a) and Fig. 3.15). The situation is similar for the N_2 PID; the PCS of N_2 is about three times larger at θ_{in} = 45° (θ_{des} = 0°) than at the other angles. This is because the Q_1 component is dominant at θ_{des} = 0°, whereas the Q_2 component is larger at the other angles as shown in Fig. 3.14 (b). In order to distinguish the main photodesorption mechanism at each angle, the corresponding speed components in Fig. 3.14 are indicated next to the data symbol.

With the help of the marking of data symbols, it is now clear that the data points assigned to P_1 are fitted best by the theoretical curves of the direct excitation mechanism, whereas the data points for P_2 are fitted well by the surface absorbance curve. Those for Q_2 can be fitted well by the surface absorbance curve (not shown). However, it was not possible to apply these fitting procedures to the single data point for Q_1 at θ_{in} = 45°. For Q_1, its PCS could be measured if only θ_{in} was changed with a constant θ_{des}. However, unfortunately this was not possible due to the limitation in the experimental configuration where θ_{in} and θ_{des} cannot be changed independently.

The PCS of N_2O at θ_{in} = 45° for 3.5 eV in *p*-polarization, 4.0 eV in *non*-polarization, and 4.7 eV in *p*-polarization, were estimated to be ~ 1.5×10^{-20} cm^2, ~ 2.1×10^{-19} cm^2, and ~ 5.7×10^{-18} cm^2, respectively[2]. Significant discrepancy between the effective absorbance of the Ag surface and the PCS of N_2O as a function of incident photon energies is found. The ratio of the effective absorbances at the Ag surface [49] is 0.17: 1.0: 2.0, however, that of the PCS is 0.07: 1.0: 27 for 3.5 eV in *p*-polarization, 4.0 eV in *non*-polarization, and 4.7 eV in *p*-polarization, respectively, at θ_{in} = 45°. The deviation of the PCS from the effective absorbance can be explained by (1) involvement of the direct desorption mechanism at higher photon energies and (2) the existence of multi-resonances of the electron affinity level as in the case of N_2O on Si(100) [134].

[2] Since the photodesorption signal by 3.5 eV in *p*-polarization irradiation was hardly detectable with the QMS due to a low photodesorption cross section, the integration of the desorption signal in the pre- and post-irradiation TPD shown in Fig. 3.13 (a) are compared with the irradiated number of photons in order to estimate the PCS.

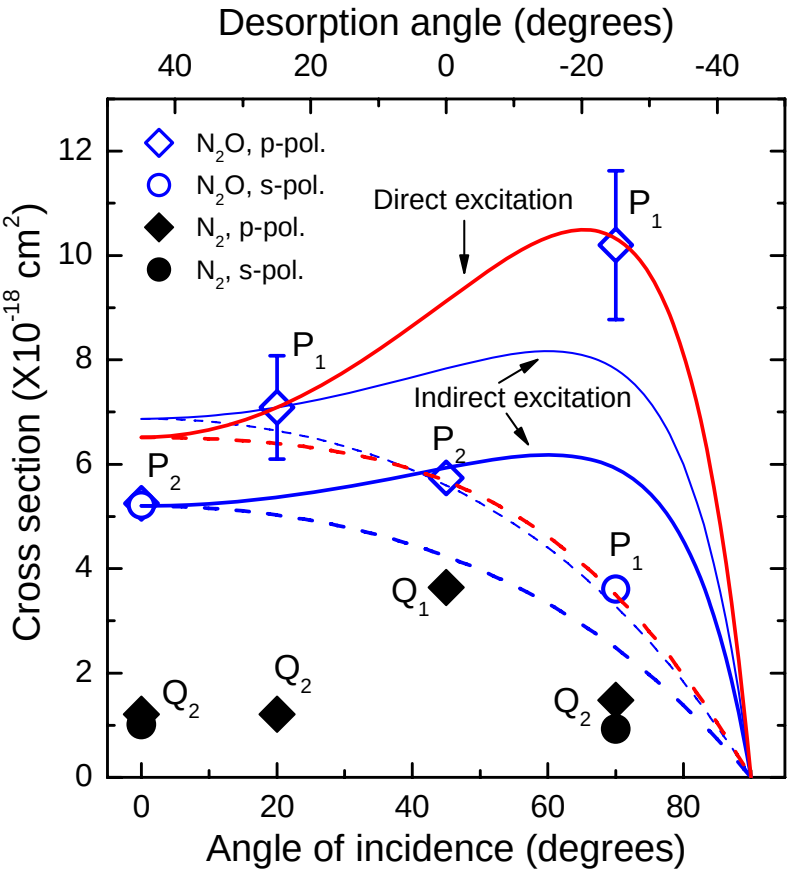

Fig. 3.17. PCS of N_2O (open symbols) and N_2 (solid symbols) as a function of angle of incidence and QMS detection angle by using 4.7 eV photons. Blue curves and red curves show the best fit of the calculated surface absorbance and photoexcitation probability, respectively. Solid and dashed curves correspond to *p*- and *s*-polarization, respectively. The captions P_1, P_2, Q_1, and Q_2 (See Fig. 3.14) indicate the main speed component contributing to the PID signal at each desorption angle.

3.2.4. Origins and photodesorption mechanisms of N_2O and N_2 from N_2O/Ag(111)

So far, at least two different speed components have been identified for both N_2O and N_2 photodesorbed from Ag(111) at 4.7 eV (See Fig. 3.14). They also show differences in angular distributions and photodesorption cross sections. Here we discuss their origins and possible photodesorption mechanisms.

Photodesorption of N_2O

The two speed components, P_1 and P_2, show clear differences in their angular distributions, photodesorption cross sections, and photoexcitation mechanisms. Table 3.3 summarizes their characteristic features.

Table 3.3. Comparison of P_1 and P_2 in photodesorption of N_2O from N_2O/Ag(111) at 4.7 eV.

Component	Excitation Mechanism	Photodesorption Cross Section	Translational Temperature (K)	Direction of Photodesorption	n in $\cos^n\theta_d$
P_1	Direct	High	3100 K	Off-normal, $\theta_{des} = \sim 25°$	20
P_2	Indirect	Low	1100 K	Normal, $\theta_{des} = 0^o$	1.7

The most remarkable difference between P_1 and P_2 lies in their excitation mechanisms, which suggests that a photodesorption channel via direct photoexcitation of N_2O is responsible for P_1, whereas one via excitation by hot electron attachment into the resonance state of N_2O gives rise to P_2. These two components seem to evolve differently (cf. Fig. 3.15), suggesting that their origins are different. This excludes parallel excitation of a single state N_2O by direct photon absorption and electron attachment.

Then the question is the multiplicity of N_2O adspecies. The only experimental evidence concerning the adsorption states of N_2O on Ag(111) is the pre-irradiation TPD result which shows only a single molecular desorption peak at 82 K. This is against the coexistence of multiple N_2O species. However, there may be several different configurations of N_2O at the sample temperature for photodesorption experiments at ~ 30 K, which is well below the desorption temperature. The N_2O molecule has one oxygen atom and two distinguishable nitrogen atoms which can bonud to the surface. Therefore, (1) oxygen-end-down, (2) central nitrogen-end-down, (3) terminal nitrogen-end-down,

and (4) flat lying structures, etc., may be possible. Also, the difference in the adsorption sites on Ag(111) may lead to different adsorption states of N_2O. The perturbation by photofragments such as O and N_2 may influence the adsorption states and photoreactions of N_2O. However, this is not the main effect causing the multiple photoexcitation/photodesorption mechanisms, because P_1 and P_2 appear from the very beginning of photoirradiation.

The correlation between the initial adsorption states and photodesorption channels cannot be distinguished at present, because there is little information about either the geometrical or electronic structures of N_2O on Ag(111). It is clear that further experimental and theoretical studies are necessary to determine the adsorption states of N_2O. Also, the determination of photodesorption mechanisms like the MGR model [4, 63] or the Antoniewicz model [9] is not possible, because the nature of the excited states of N_2O on Ag(111) is unknown.

The involvement of direct excitation at 4.7 eV strongly suggests that the absorption band of N_2O is red shifted. The absorption of gaseous N_2O starts from 5.6 eV [139]. Thus, the corresponding excited state must be lowered by at least 0.9 eV. The lowering of the direct photoexcitation energy of a weakly bound adsorbate has been observed for CH_4 on Pt(111), Pd(111), and Cu(111) [44, 140], in which CH_4 either dissociates or desorbs at 6.4 eV. In the CH_4 on Pt(111) and Pd(111) cases, theoretical studies revealed that the Rydberg states of CH_4 interact with empty states of the metal surfaces. The situation for N_2O/Ag(111) would be quite similar; N_2O has Rydberg states. Thus, the red shift of the excitation energy via the same mechanism seems plausible. Also, the molecular structure of N_2O is known to dramatically change the potential energy surface and absorption cross section [141-143]. Thus interaction between N_2O and Ag(111) can open up new excitation channels which are accessible with a 4.7 eV photon.

Next, we discuss the dynamics of photodesorption. The most striking feature is that photodesorption of the P_1 component is peaked in off-normal direction. This requires that a lateral force is exerted on the adsorbate in the electronically excited state. Hasselbrink et al. reported that photodesorption of α_3 superoxo O_2 coadsorbed with $p(2 \times 2)$ oxygen atoms on Pd(111) is peaked at $\sim 60°$ from the surface normal [144]. In this case, the atomic-molecular oxygen repulsion in addition to the orientation of the molecular axis was thought to be the origin of the off-normal desorption.

However, in the case of N_2O/Ag(111), there are no other adsorbates like oxygen atoms which may affect the adsorption geometry and the PES of N_2O as in the case of O_2/ $p(2 \times 2)$-O/Pd(111). Note that off-normal photodesorption of N_2O is observed from the early stage of photoirradiation; thus, this is not due to the influence of oxygen atoms produced by photodissociation of N_2O. Since the Ag(111) surface is flat and in the sixfold or threefold symmetry, it is unlikely that only a tilted structure of N_2O results in the off-normal photodesorption. In many systems where the molecular axis of the adsorbates are tilted from the surface normal, off-normal photodesorption is seldom

observed [2]. Off-normal photodesorption of O_2 has been observed for O_2 adsorbed on a stepped Pt(112) by 4.0 eV photons [138]. However, in this case, the primary step is photodissociation of an O_2 molecule and neighboring O_2 molecules are hit by the energetic O fragment and gain a surface-parallel momentum. Matsumoto and coworkers observed off-normal photodesorption of N_2 from N_2O on Si(100) at 5.0 and 6.4 eV [133]. Also in this case, the interaction between the adsorbate and oxygen atoms is thought to give a surface-parallel momentum. However, off-normal photodesorption was not observed in the case of N_2O and N_2 photodesortpion from N_2O/Pt(111) studied by the same authors [133]. In contrast, Kummel and coworkers observed off-normal photodesorption of oxygen atoms emitted from N_2O/Pt(111) irradiated with 6.4 eV photons [145]. They concluded that oxygen atoms (both $O(^3P)$ and $O(^1D)$) are emitted along the molecular axis of the parent N_2O molecule tilted at 35° from the surface plane [146]. However, photodesorption of N_2O tilted from the surface normal has not been observed. In the case of N_2O/Pt(111), oxygen atoms are accumulated by photodissociation of N_2O. Thus, coadsorption with oxygen atoms does not significantly change the molecular photodesorption of N_2O, probably because the adsorption of N_2O on Pt(111) is weak and it is not modified by coadsorbed atomic oxygen.

The off-normal photodesorption of N_2O from Ag(111) requires that a mechanism in which photodesorbing N_2O gains a surface-parallel momentum is involved. However, no force parallel to the flat Ag(111) will be applied on the transiently formed N_2O^- by electron attachment, which will be attracted by the image charge, in terms of the Antoniewicz model. If the PES of the excited N_2O is repulsive, as in the MGR model, the high symmetry of the flat Ag(111) should not apply a significant surface-parallel momentum on the weakly bound N_2O.

A plausible mechanism for the off-normal photodesorption of N_2O is that the P_1 component stems from photodissociation of a dimer or a cluster of N_2O. It is well known that N_2O forms van der Waals dimers in the gas phase [147]. On a cold Pd(110) surface, small aggregates of N_2O extending along the [110] have been observed by STM [148, 149].

The assumption of formation of N_2O dimers or small clusters on Ag(111) can explain the three main features of the experimental results:

(1) Off-normal photodesorption of N_2O. Splitting of N_2O dimers/clusters aggregating parallel to the surface should lead to the acceleration of the N_2O monomer in an off-normal direction.

(2) Red shift of photoexcitation energy from 5.6 eV to 4.7 eV; The LUMO or Rydberg states of N_2O may be lowered by the hybridization as a result of clustering. This may enable direct photoexcitation from the HOMO to the hybridized states.

(3) Direct excitation of adsorbates inferred by the results of the incident angle dependence of the PCS measurements.

These agreements strongly support the assumption that photodissociation of N_2O aggregates is responsible for the P_1 component. Structural information of N_2O on Ag(111) below liquid nitrogen temperatures is not available. However, it is not unlikely that N_2O forms dimer or clusters on Ag(111) at 30 K. In fact, clusters of NO are observed at the same temperature range.

A secondary process like Reaction (3.16), $O^* + N_2O(a) \rightarrow N_2O(g) + O(a)$, can also explain the off-normal desorption of N_2O. However, the mean translational energy of P_1 (0.53 eV) seems too high considering the possible kinetic energies of O* (0.4 – 0.67 eV) [145] and the mass ratio 44:16 between N_2O and O. The heat of adsorption of O atoms on Ag(111) might add some kinetic energy to the desorbing N_2O, however, the heating of the substrate should enhance thermal desorption only along an off-normal direction. Also, production of O* results from photodissociation of N_2O, which is most probably via substrate mediated (indirect) excitation. Thus, Reaction (3.16) is not fully consistent with the experimental results.

The P_2 component, on the other hand, is peaked at the surface normal with a T_t of ~ 1100 K, which is between the values (1700 K and 810 K) observed for N_2O photodesorption from Pt(111) [150]. The angle-of-incidence dependence of the PCS suggests that this component stems from indirect excitation of N_2O by hot electron attachment. Thus, photodesorption of the P_2 component can be explained successfully by the Antoniewicz model [9]. The spatial distribution of P_2 is rather broad; n=1.7. This may suggest scattering of N_2O^- by neighboring adsorbates.

Photodesorption of N_2

The characteristic features of Q_1 and Q_2 components in N_2 photodesorption from N_2O/Ag(111) are summarized in Table 3.4. Both components are peaked at the surface normal, similar to the case of N_2O/Pt(111) [145, 150]. The T_ts of Q_1 and Q_2 are also similar to those observed for N_2O/Pt(111) [150]. However, the photodesorption cross sections and the breadth of spatial distributions are different between Q_1 and Q_2.

Table 3.4. Comparison of Q_1 and Q_2 in photodesorption of N_2 from N_2O/Ag(111) at 4.7 eV.

Component	Excitation Mechanism	Photodesorption Cross Section	T_t (K)	Direction of Photodesorption	n in $\cos^n\theta_d$
Q_1	N/A	High	2200	Normal, $\theta_{des} = 0^o$	12
Q_2	Indirect	Low	600	Normal, $\theta_{des} = 0^o$	5

Since N_2O/Ag(111) photodissociates upon 4.7 eV photon irradiation, either Q_1 or Q_2 is responsible for the photofragment N_2 produced by Reaction (3.12). The growth of the PID results in Fig. 3.16 suggests that the Q_2 component stems from photodesorption by Reaction (3.13) of N_2 photoproducts accumulated on the surface. Thus, Q_1 is attributed to photodesorbed N_2 by photodissociation of N_2O (Reaction (3.12)).

The photodesorption cross section of Q_1, σ_{Q1}, measured at $\theta_{in} = 45^o$ is $\sim 4 \times 10^{-18}$ cm^2. This is about 2/3 of that of P_2 of N_2O, σ_{P2}, $\sim 6 \times 10^{-18}$ cm^2. However, if Q_1 and P_2 originate from photodissociation and photodesorption of N_2O(a), respectively, σ_{Q1} must be equal to σ_{P2}. The reason that σ_{Q1} is smaller than σ_{P2} is likely to be that the Q_2 component contributes the PID signal of N_2. The ratio of Q_1 to Q_2 is 0.55:0.45 at $\theta_{in} = 45^o$, according to the analysis of the TOF spectra in Fig. 3.14 (b). Assuming $\sigma_{Q2} = \sim 1.5 \times 10^{-18}$ cm^2 (cf. Fig. 3.17), one obtains an averaged photodesorption cross section of N_2 as $\sim 4 \times 10^{-18}$ cm^2 by simple weighted averaging, $0.55 \times \sigma_{P2} + 0.45 \times \sigma_{Q2} = (0.55 \times 6 + 0.45 \times 1.5) \times 10^{-18} = 4 \times 10^{-18}$ cm^2. This calculation confirms that Q_1 stems from photodissociation of N_2O.

Next, we discuss the photodesorption mechanism of Q_2. That its T_t is much higher than the substrate temperature shows that this process is nonthermal. Nonthermal photodesorption of N_2 from Ag(111) by infrared irradiation (1.17 eV) has been reported by White and coworkers [151]. Their results suggest that "physisorbed adsorbates can couple directly to the nascent-phonon distribution or the nascent electron–hole pairs in the photoexcited substrate without heating of the surface." They observed photodesorbed N_2 with $T_t = \sim 100$ K from Ag(111) at ~ 30 K. However, the T_t of Q_2 is ~ 600 K, far above their value. Thus, the photodesorption mechanism of Q_2 is likely different from that proposed for IR induced desorption by White et al [151]. As the LUMO corresponding to the $2\pi^*$ antibonding orbital of the weakly bound N_2 on Ag(111) is located from ~ 0.5 eV to ~ 3 eV above the vacuum level with a peak at 1.5 eV [152, 153], this state may be accessible with the photon energy of 4.7 eV and the work function of silver (4.3 eV). However, photodesorption of molecular N_2 on Ag(111) by visible and UV light has not been studied yet, and this is out of the scope of the present study. Another possible desorption mechanism is a secondary process in which N_2(a) is hit by an energetic O atom, $O^* + N_2(a) \rightarrow N_2(g) + O(a)$. Such a process was observed for photodesorption of O_2 adsorbed on the stepped Pt(112) surface [138]. However, in this case the desorbing O_2 is peaked at an off-normal direction; the surface parallel momentum is conserved. As the Q_2 component is peaked at the surface normal direction and its spatial distribution is relatively broad with $n = 5$, a thermal process is more plausible where N_2(a) is desorbed by the local heating of the substrate by adsorption of O*.

It's worth mentioning that the T_t of the Q_1 and Q_2 components are much lower than that observed in photodesorption of N_2 (~ 5700 K) from $(NO)_2$/Ag(111) described in section 3.1. It is therefore concluded that photoreactions of N_2O on Ag(111) do not

account for the photochemical formation of very energetic N_2 from the NO dimers on Ag(111).

3.2.5. Summary

N_2O on Ag(111) is photoreactive at photon energies ≥ 3.5 eV. N_2O photodesorbed at 4.7 eV shows two distinct desorption dynamics. The fast component (T_t = ~ 3100 K) is directed in an off-normal direction (~ 25°) with a sharp angular distribution, and the slow component (T_t = ~ 1100 K) is desorbed to the surface normal with a relatively broad angular distribution. Photodesorption of N_2 also consists of two components (T_t = ~ 2200 K and ~ 600 K), but both are directed to the surface normal. Based on the angle-of-incidence dependence of the PCS, it is concluded that the fastest component of photodesorbed N_2O stems from direct photoexcitation of the adsorbates, which is proposed to be aggregates of N_2O on Ag(111). This is the first example of off-normal molecular photodesorption from a monolayer of homogeneous adsorbates on a flat metal surface. The other desorption components of N_2O and N_2 are ascribed to primary or secondary processes of a transiently formed N_2O^- via substrate mediated excitation. The T_t of photodesorbed N_2 components are far below that observed for N_2 photodesorbed from $(NO)_2$/Ag(111) at 4.7 eV. Thus, a contribution of N_2O intermediates to the photochemical formation of the very fast N_2 (T_t = ~ 5700 K) from NO dimers is excluded.

Chapter 4. Comparision of thermal- and photoreactions of NO on Ag nanoparticles and Ag(111)

This chapter presents thermal- and photo-reactions of NO on Ag NPs compared to those on Ag(111) by means of the same experimental setup and procedures shown in section 3.1. Ag NPs were formed by depositing Ag atoms from an electron beam evaporator on an Al_2O_3/NiAl(110) substrate. The average size of the Ag NPs was set at ~ 8 nm as calibrated by separate STM observations. The enhanced PCS of NO on supported Ag NPs were observed on plasmon resonance as well as off plasmon resonance, and broadened mass-selected TOF spectra from NO on Ag NPs were found at all photon energies used (2.3 – 4.7 eV). Comparison of the PCS and TOF spectra of NO photodesorbed from Ag NPs between on and off Mie plasmon resonance reveals that there is no difference in the photodesorption mechanism between on and off resonance although the PCS is significantly enhanced at on resonance.

4.1. Introduction

Studies of metal NPs have been an area of intense scientific research over the last several decades [1, 14, 20] due to a wide variety of potential applications such as sensors [154], SERS [155-163], diagnosis and treatment of cancer [164], Fabry-Perot resonators [165], and surface photochemistry [1, 166]. This interesting research is based on distinct optical and electronic properties of metal NPs, typically smaller than 10 nm, compared to those of corresponding bulk.

In the previous chapter it has been shown that hot electron attachment is the main photoexcitation mechanism for the photochemistry of NO on Ag(111) by comparing the PCS with calculated surface absorbance, indicating that the photoreaction cross section is

directly influenced by hot electron dynamics. Since the energy dissipation processes of created hot electrons in small metal NPs supported on dielectric films are expected to be modified from those in corresponding bulk material, it is interesting to investigate the modified hot electron dynamics from a photochemical point of view.

Surface plasmon excitation, which is the collective motion of free electrons in the conduction band, is a unique property for metal NPs and has been studied by photon STM [18] and 2PPE [41]. Meech and co-workers have compared the PCS of adsorbates on Ag(111) and Ag surfaces roughened by sputtering and have shown that the PCS exhibits a resonant enhancement against photon energy, which is absent for Ag(111) [167]. The resonance was located at ~ 3.5 eV, corresponding to the typical Ag surface plasmon resonance, and the resonant features were independent on the adsorbates. Thus, they suggested that surface plasmon excitation enhanced the available number of hot electrons for photodesorption via the plasmon decay into electron-hole pairs and surface electric field amplification.

It should be mentioned that the T_t are different between Meech's [113] and our results in section 3.1 for NO on Ag(111). The T_ts in our TOF measurements are higher than those of Ref. [113]. Their T_t of NO photodesorbed by 3.5 eV photons from NO adsorbed on Ag(111) at ~ 87 K was ~ 490 K and that from a sample annealed to ~ 300 K was ~ 730 K. The corresponding values from our TOF measurememts are ~ 600 K (3.5 eV) and ~ 1000 K (4.7 eV). These T_t differences are probably due to different accuracies of the flight lengths and of the calibration of the ion flight time in the mass filter of QMS, and possibly to the pumping speeds near the ionizer of the QMS (flux vs. density detector properties). Differences in T_t as much as 80 % have been reported in SO_2/Ag(111) systems, for example [168, 169]. We do not want to argue which setup gives the better absolute values, but do wish to point out the importance of using the same experimental setup and procedures if comparisons of the photodesorption data between different samples are intended.

In this section thermal and incident photon energy and polarization dependent photoreactions of NO on Ag NPs supported on Al_2O_3 film are presented and compared to the results from NO on Ag(111) by means of the same experimental setup and procedures shown in section 3.1. An enhancement of the PCS for NO on Ag NPs is observed, and the enhancement factor is peaked at the plasmon resonance of Ag NPs. The TOF of NO desorbed from Ag NPs is broader than that from Ag(111). The differences are discussed with the adsorption state of NO and the properties of the surfaces.

4.2. Experimental

The fabrication of Ag NPs was described in Chapter 2. NO was dosed at 75 K on 5 Å deposited Ag/ Al_2O_3/NiAl(110) whose mean particle diameter is ~ 8 nm to the saturation coverage, and then the sample was subsequently cooled down to ~ 30 K or kept at ~ 120 K. Nanosecond laser pulses from the second, third and forth harmonics of a Nd:YAG laser (2.3, 3.5, and 4.7 eV in polarized light, respectively) and a XeCl excimer laser (4.0 eV, *non*-polarized light) were used in this section. The sample surface normal was oriented into the QMS axis, and the beam incident angle was fixed to 45 degrees. For details see experimental in Chapter 2. In order to estimate T_t of photodesorbed NO, TOF spectra were deconvoluted by two shifted Maxwell-Boltzmann distributions. The T_t shown in this section represents the main component in the TOF spectra.

4.3. NO adsorption on Ag NPs and Ag(111)

Fig. 4.1 presents pre-irradiation TPD results from Ag NPs and Ag(111) dosed with NO at ~ 75 K to the saturation coverage measured at mass number m/e = 30. The three NO peaks from Ag(111), ~ 97, ~ 115, and ~ 400 K, originate from dissociation of NO dimers to emit NO, cracking of N_2O, and NO monomer, respectively (see section 3.1 for detail). Similarly, NO desorption signals from Ag NPs peaked at ~ 86 K and ~ 102 K can be assigned to NO from NO dimer and cracking of N_2O, respectively. The broad feature from ~ 120 K to ~ 450 K from Ag NPs originates from NO monomers, consisting of two peaks (~ 160 K and ~ 250 K). We designate the desorption signals of NO from NO dimer and NO monomer as NO-α and NO-β, respectively.

The peak temperatures of NO and N_2O from Ag NPs are lower than those from Ag(111). When the particle size was varied, the desorption peaks from Ag NPs shifted to higher temperatures with increasing size and approached those from Ag(111) with a $1/R$ function, where R is the particle radius [170]. It has been explained by three effects: (i) changes of the van der Waals attraction (decrease with $1/R$ by the particles' curvature and the fact that all Ag atoms in NPs contribute. R is particle radius); (ii) possible weakened chemisorptive contribution by the change of Ag surface states; and (iii) a shift to larger distances of the repulsive part of the surface interaction, due to increasing spill-out of the Ag surface *sp*-electrons for smaller NPs [40].

The pre-irradiation TPD results at m/e = 44, shown in the inset of Fig. 4.1, present the different thermal reaction of NO dimer on Ag(111) and Ag NPs. The detail of N_2O

formation from NO dimer on Ag(111) is described in section 3.1. According to the studies by King's group [112], the peak at ~ 96 K stems from decomposition of the α, γ, and δ-phases and the peak positioned at ~ 115 K from that of the β-phase of NO dimers on Ag(111). In contrast, only one N_2O peak is observed in the TPD from Ag NPs, which is located at ~ 102 K, in between the two peaks in the Ag(111) TPD.

The relative desorption yields of NO and N_2O from NO dosed at ~ 75 K on Ag NPs and Ag(111) are summarized in Table 4.1. The NO dimers on Ag NPs compared to that on Ag(111) were preferentially dissociated to NO monomers and converted to N_2O. The relative signal intensity NO-β / NO-α is ~ 2.3 times higher for Ag NPs. N_2O signal intensity compared to the total amount of NO signal (NO-α + NO-β) is also slightly higher for the Ag NPs. Note that the signal intensities were corrected by relative QMS sensitivity for NO and N_2O.

Table 4.1. Relative desorption yields in pre-TPD of Ag NPs and Ag(111) dosed with NO at 75 K.

Surface	NO-β / NO-α	N_2O/NO
Ag(111)	0.53	0.42
Ag NPs	1.23	0.62

The pre-irradiation TPD measurement of NO dosed at 75 K on bare Al_2O_3 was performed in order to investigate the contribution of desorption signals from the supporting film. Neither parent NO molecules nor any reaction products which could be formed from NO species (N_2O, NO_2, N_2, O, and O_2) were detected; this fact allows us to investigate thermal and photoreactions of NO adsorbed only on Ag NPs.

Fig. 4.2 displays post-irradiation TPD spectra for m/e = 30 and 44 (inset) from Ag NPs measured after the photodesorption signal of NO is depleted. The incident photon energy dependence of the NO-α and NO-β peak are very different. Irradiating with a 2.3 eV laser beam, the NO-α peak is significantly reduced whereas the NO-β peak is almost unchanged. At a photon energy of 3.5 eV, the NO-α peak is totally depleted and the first NO-β peak (~165 K) is also reduced whereas the second NO-β peak (~ 260 K) is almost unaffected. All of the NO peaks are depleted after prolonged irradiation at photon energies $\geq$ 4.0 eV. All the post-irradiation TPD results were independent of the polarization of the incident laser beam. Since overall photon energy dependencies of NO on Ag NPs in post-TPD results are comparable to those on Ag(111) except the desorption temperatures, we conclude that the affinity levels of the NO dimers and monomers on Ag NPs and Ag(111) are comparable. Summarizing, the affinity level of the NO dimer is

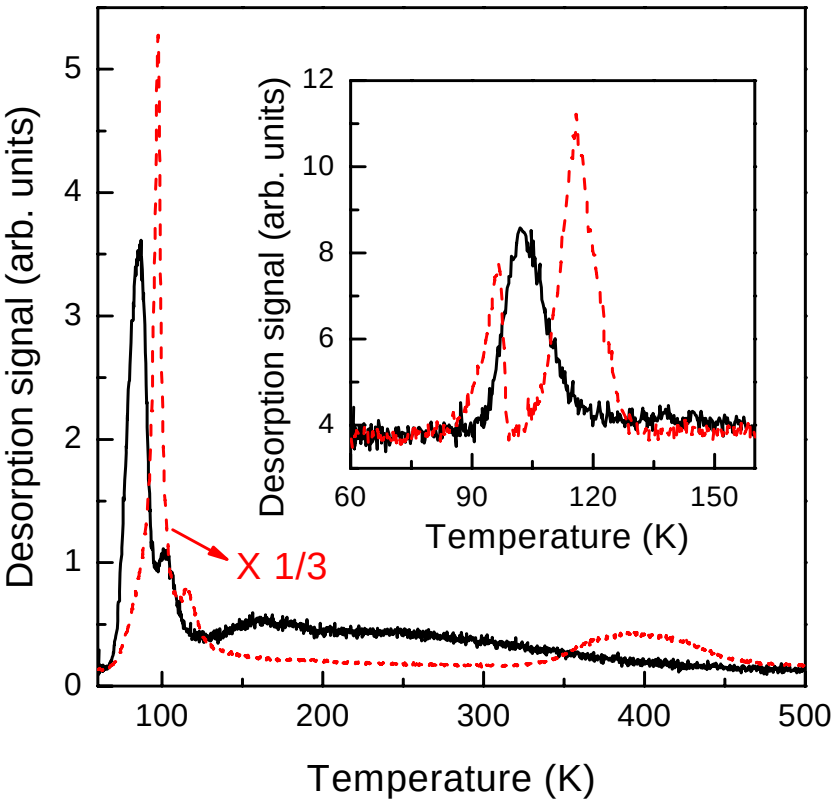

Fig. 4.1. Pre-irradiation TPD results from Ag NPs/Al_2O_3/NiAl(110) (solid curves) and Ag(111) (dashed curves, multiplied by 1/3) dosed NO at 75K to the saturation coverage, measured at m/e = 30. The inset was measured at m/e = 44.

distributed below 2.3 eV, while that of the NO monomer is higher than 2.3 eV and distributed partially below 3.5 eV, and lower than 4.0 eV.

The N_2O peak from Ag NPs (Fig. 4.2 inset) in the post-irradiation TPD compared to that in the pre-irradiation TPD is almost the same for 2.3 eV laser beam irradiation; however, it was shifted to ~ 96 K by 3.5 eV photon irradiation and almost depleted by irradiation at 4.7 eV. The photo-reactivity of N_2O formed from NO dimers on Ag(111) is described in detail elsewhere (see section 3.1). The ~ 96 K desorption peak of N_2O formed from the α, γ, and δ-phases of NO dimers on Ag(111) was depleted by laser irradiation at ≥ 2.3 eV, whereas the N_2O peak at ~ 115 K stemming from the β-phase of NO dimers was slightly reduced. The latter N_2O peak position was not altered by 2.3 eV laser irradiation but shifted to a lower temperature by ≥ 3.5 eV laser irradiation. Thus, the photo-reactivity of N_2O formed from Ag NPs is similar to N_2O formed from the β-phase of NO dimers on Ag(111).

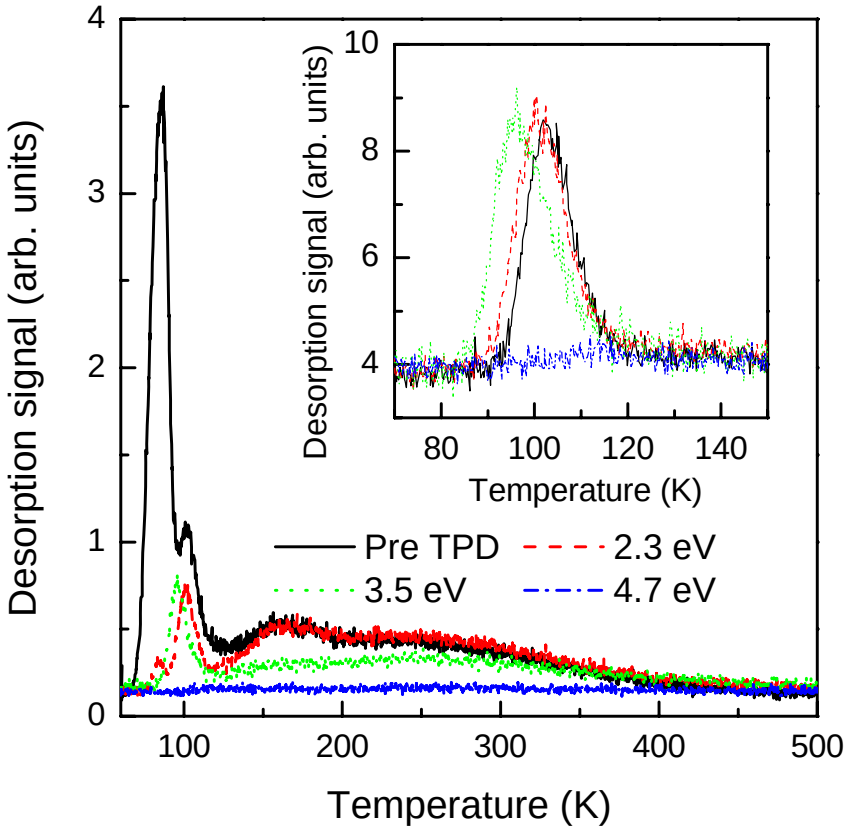

Fig. 4.2. Pre- and post-irradiation TPD at m/e = 30 and 44(inset) at various photon energies from Ag NPs measured after the photodesorbed NO signals were depleted.

4.4. Enhanced photodesorption cross section of NO on Ag NPs

PID signals of NO from Ag NPs being dosed with NO at 75 K to the saturation coverage and subsequently cooled down to ~ 30 K are presented in Fig. 4.3 using a logarithmic scale. Data measured at the sample covered with the NO saturated monolayer and annealed and kept at ~ 120 K are shown as closed stars. Keeping the sample temperature at ~ 120 K after NO dosage at 75 K leads to removal of NO dimers and N_2O on the surface. The inset shows the same data as in the main figure but plotted with an extended number of photons. The desorption signals were corrected by the number of irradiated photons and the transmittance of the viewing window at the corresponding

photon energies. The decay of the PID signal strongly depends on the incident photon energy and polarization. The decay at 2.3 eV is linear (i.e., exponential, whereas fast and slow decays are observed for photon energies ≥ 3.5 eV). These results indicate that at a photon energy of 2.3 eV only the NO dimers on Ag NPs are photoactive, whereas at ≥ 3.5 eV both the NO dimers and monomers are photoreactive. When the PID was measured at ~ 120 K only the slow component was observed even though the incident photon energy was higher than 3.5 eV, indicating that only NO monomers contributed to the PID signal. These results are consistent with the post-irradiation TPD results shown in Fig. 4.2 and NO on Ag(111) (see section 3.1).

Fig. 4.4 displays PID signals of NO dosed at 75K, measured at various photon energies and polarizations, and normalized by the desorption signal intensity for the first laser shot. The decay becomes faster with increasing photon energy in the case of the *s*-polarized laser irradiation, whereas the fastest decay is observed at 3.5 eV in the case of the *p*-polarized laser irradiation.

The PCSs of NO photodesorbed from Ag NPs and Ag(111) dosed with NO at 75 K

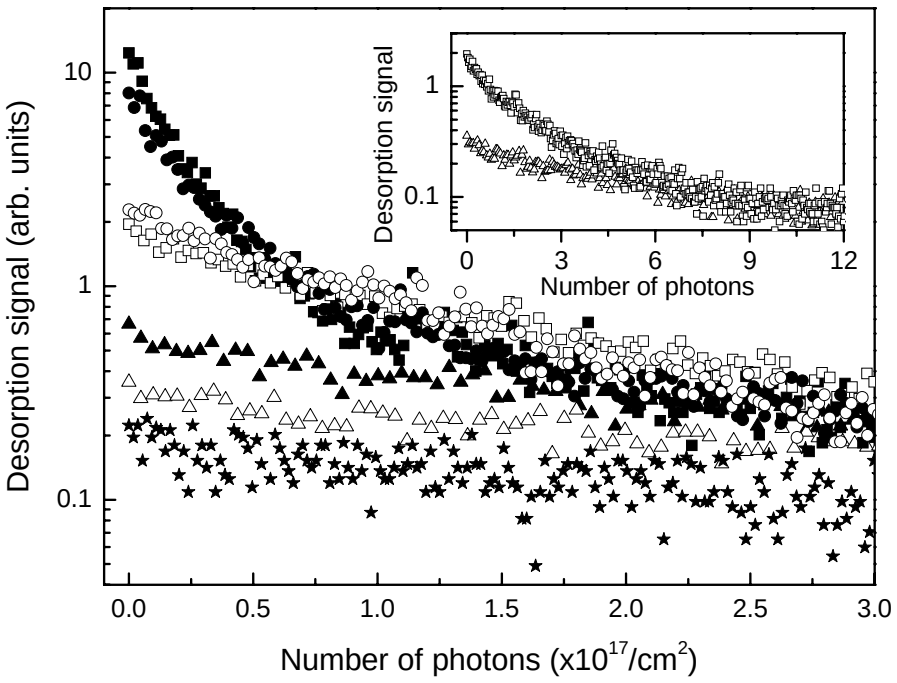

Fig. 4.3. PID results of NO from Ag NPs with saturation coverage of NO dosed at 75 K, and then subsequently cooled down to ~ 30 K, measured at photon energies 2.3 eV (triangles), 3.5 eV (squares), and 4.7 eV (circles), in *p*-(closed symbols) and *s*- (open symbols) polarization, respectively. Closed stars are data measured at 120 K after dosing at 75 K using 3.5 eV in *p*-polarization. Laser irradiances on the sample were ~ 1.0 mJ/cm^2/shot for the 3.5 eV in *p*-polarization and ~ 1.7 mJ/cm^2/shot for the others. The inset is PID results plotted with extended number of photons.

are estimated from PID curves by a single exponential fitting function, from the desorption signal driven by the first laser shot to 50% of the maximum desorption signal, and are summarized in Table 4.2. It should be mentioned that the PCS shown here represents only the decay of the NO dimer because it is much faster than the decay of the monomer. There are two noticeable phenomena: (i) the PCS of NO from Ag NPs is higher than that from Ag(111) except for at 4.7 eV in *s*-polarization; (ii) the PCS of NO on Ag(111) monotonically increased with increasing photon energy of the incident light in both polarizations, whereas that on Ag NPs showed a strong resonance feature at 3.5 eV laser irradiation only for *p*-polarized laser irradiation.

The increase in the PCS of NO from the Ag NPs is probably related to modified hot electron dynamics because the substrate mediated mechanism plays a major role in the photoexcitation of NO on Ag surfaces (see section 3.1). The electron mean free path is given by $l_{e-e} = \tau \cdot v$, where τ is the electron lifetime and v the electron velocity. Since the electron affinity level of NO dimers on Ag NPs is located ~ 2 eV from the Fermi level, l_{e-e} for hot electrons hopping from the surface to the adsorbate is ~ 8 nm with $\tau = 5$ fs [171] and $v = \sim 1.6 \times 10^6 m/s$ [3] [172]. The height of an average Ag NP is ~ 2 nm. Thus, the hot electrons can be reflected several times at the interface between the NP and the alumina before dissipating their energy via electron-electron scattering; this increases the rate of hot electrons scattering with the adsorbates, leading to a high PCS for NO dimers on Ag NPs compared to Ag(111).

It is worth mentioning that no enhancement of the PCS of NO from Ag NPs was observed compared to that from Ag(111) at 4.7 eV in *s*-polarization, which is not consistent with the above arguments. This may suggest that an additional effect plays a role at 4.7 eV irradiation, which is beyond our discussion at the moment.

The most noticeable result is the large enhancement of PCS at 3.5 eV in *p*-polarization. This is the direct consequence of the optical properties of Ag NPs, i.e. the Mie plasmon excitation. The enhanced PCS on plasmon resonance has been found in OCS, NO, and SO_2 on roughened Ag(111) [167]. Since the (1,0) mode of plasmon excitation for alumina film supported Ag NPs has been observed in Photon-STM [18] and 2PPE experiments [41] showing resonance ~ 3.5 – 3.6 eV, the enhancement at 3.5 eV in *p*-polarization can be interpreted in terms of increased hot electron populations via plasmon decay into electron-hole pairs and electric field enhancement [173] at the NP surfaces.

[3] The electron velocity at 2 eV from the Fermi level. The Fermi energy and velocity in Ag are 5.5 eV and $v_F = \sim 1.4 \times 10^6 m/s$, respectively.

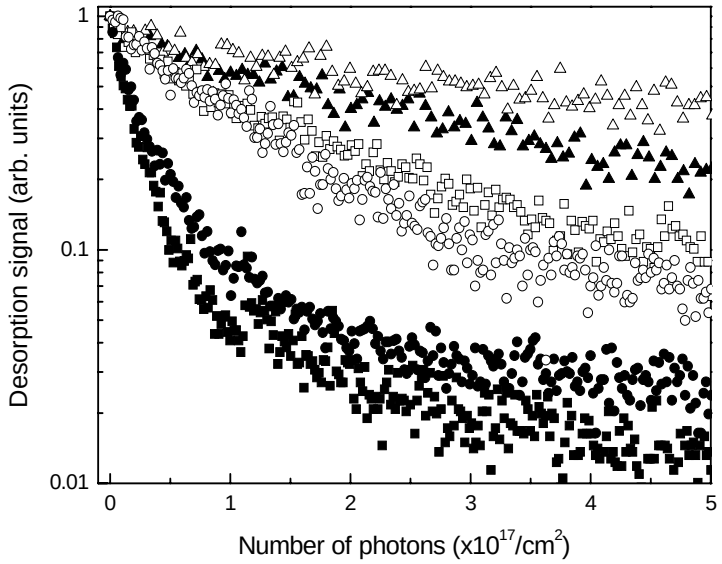

Fig. 4.4. PID results of NO from Ag NPs with saturation coverage of NO dosed at 75 K, measured at photon energy 2.3 eV (triangles), 3.5 eV (squares), and 4.7 eV (circles), in *p*-(closed symbols) and *s*- (open symbols) polarization, respectively, normalized by desorption signal intensity for the first laser shot.

Table 4.2. Photodepletion cross sections of NO from Ag NPs and Ag(111) dosed with NO at 75 K.

Photon Energy (eV)	Polarization	PCS of NO ($\times 10^{-18}$ cm^2)		
		Ag NPs	Ag(111)	Ratio (Ag NPs / Ag(111))
2.3	*P*	2.13 ± 0.06	0.86	2.48
	S	1.36 ± 0.23	0.39	3.49
3.5	*P*	58.8 ± 4.45	3.9	15.1
	S	7.30 ± 1.79	2.8	2.6
4.0	*Non-pol.*	9.5	5.8	1.64
4.7	*P*	37.8 ± 2.90	14.6	2.59
	S	11.2 ± 0.57	11.5	0.97

4.5. Mass-selected time-of-flight measurements of photodesorbed NO

TOF measurements of NO photodesorbed from Ag NPs and Ag(111) were performed in order to distinguish effects of the peculiar properties of Ag NPs on photodesorption mechanisms. The normalized TOF spectra measured at 2.3 eV in *p*-polarization are compared in Fig. 4.5. Note that only the NO dimers are photoactive with 2.3-eV laser irradiation on both surfaces. The peak positions are almost the same, however, the spectrum from Ag NPs is somewhat broader than that from Ag(111). The spectrum from Ag NPs rises earlier than that from Ag(111); however, the deviation is almost negligible after ~ 150 μs before the peak. After the peak, the deviation becomes significant at ~ 300 μs and is maximized ~ 550 μs. We speculate plausible explanations for the different TOF spectrum in the following.

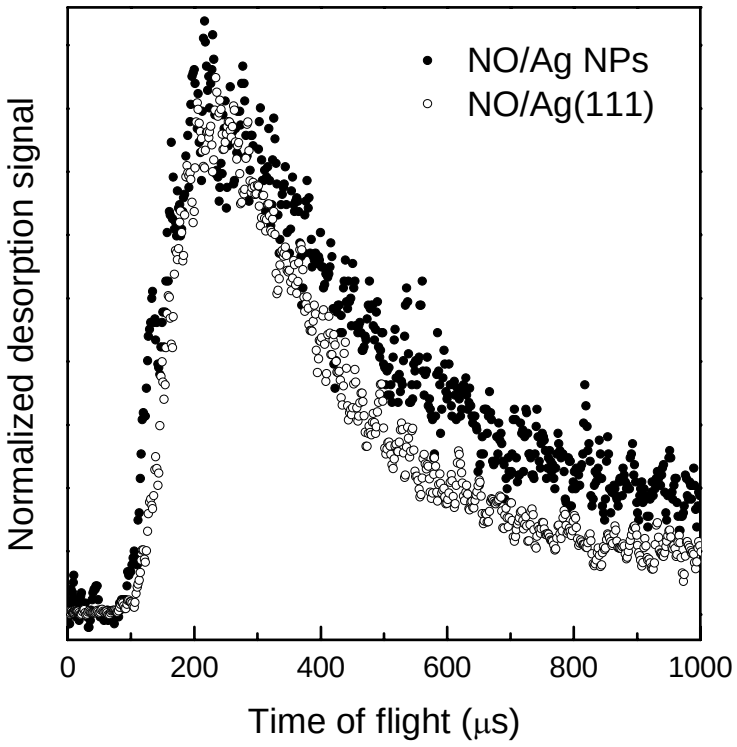

Fig. 4.5. Normalized TOF spectra of NO from NO dimers on Ag(111) and Ag NPs by *p*-polarized 2.3 eV laser irradiation. The desorption signals were accumulated for 5× 10^{17} photons/cm^2.

First, the pre-TPD result shows that the binding energy of NO dimer on Ag NPs is slightly different from that on Ag(111). Furthermore, there might be several facets on the Ag NP surface unlike Ag(111), which may lead to more complex adsorption states of NO dimers on Ag NPs. Thus, inhomogeneous adsorption structures of NO on Ag NPs compared to those on Ag(111) may cause broader TOF spectra in the former case.

Second, secondary processes such as scattering of desorbates by adjacent Ag NPs may be responsible. Generally, molecules are photodesorbed towards the surface normal with cosine power distributions. The Ag NPs on Al_2O_3/NiAl(110) used in this study are almost hemispherical [18], which implies that the desorption angle with respect to the surface normal (of the sample) varies with the position on the surface of the Ag NP. Molecules desorbed from the region near the boundary of Ag NPs may be directed towards adjacent Ag NPs, resulting in inelastic scattering or re-adsorption. In order to roughly estimate the rate of such processes, we assume that the the Ag NPs are hemispherical and uniformly distributed over the substrate, and a desorption angle is normal to the surface of Ag NPs with a cosine distribution. The re-adsorption of the desorbate on neighboring Ag NPs is neglected for simplicity. Since the density of the Ag NP is ~ 4×10^{11}/cm^2, the distance (edge to edge) between two nearest Ag NPs is ~ 8 nm. Schematic drawings of the desorption geometry of NO from Ag NPs are depicted in Fig. 4.6 (a) side view and (b) top view. In Fig. 4.6 (a), the NO on top of the Ag NP will be detected without any collision, whereas the NO sitting near the boundary of the Ag NP will collide with adjacent Ag NPs. The collision probability of the desorbate with adjacent Ag NPs is estimated by comparing total surface area of single Ag NP with the integration of the Ag NP surface whose normal vectors intersect with the adjacent Ag NPs. The simplified model calculation shows that ~ 13 % of desorbates collide with adjacent Ag NPs. Thus, such collision processes are not negligible. They should give rise to desorption with lower energies and may be responsible for the broader tail in the TOF spectrum of NO from Ag NPs than that from Ag(111).

Fig. 4.7 shows TOF spectra of NO photodesorbed from Ag NPs with 3.5 eV photons in (a) *p*-polarization, on (1,0) mode Mie plasmon resonance, (b) *s*-polarization, off plasmon resonance. The spectra are fitted by a sum of two shifted Maxwell-Boltzmann distributions. The T_t for the fast component was 686 K and 677 K on and off Mie plasmon resonance, respectively. The spectra are qualitatively the same within the experimental error, indicating no difference in photodesorption dynamics regardless of on and off Mie plasmon resonance, although the PCS is significantly different. This result is consistent with ref [168]. Meech and co-workers studied effects of surface plasmon excitation of roughened Ag surfaces on the photochemistry of SO_2 or OCS adsorbates. Their results also showed that the surface plasmon enhances the photoreaction cross section, but no new photochemical processes were found.

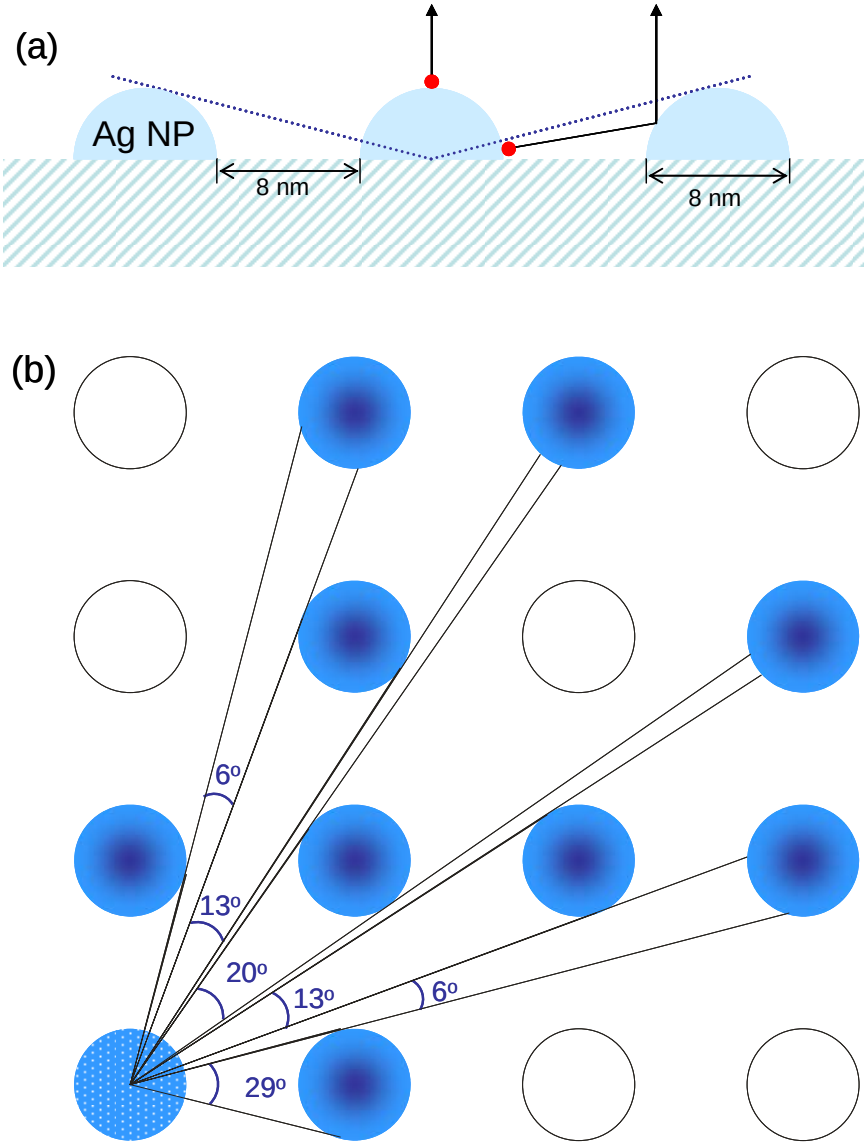

Fig. 4.6. Schematic drawings of desorption geometry. (a) side view (b) top view. The filled circles in (b) represent Ag NPs which collide with desorbates from the bottom left Ag NPs.

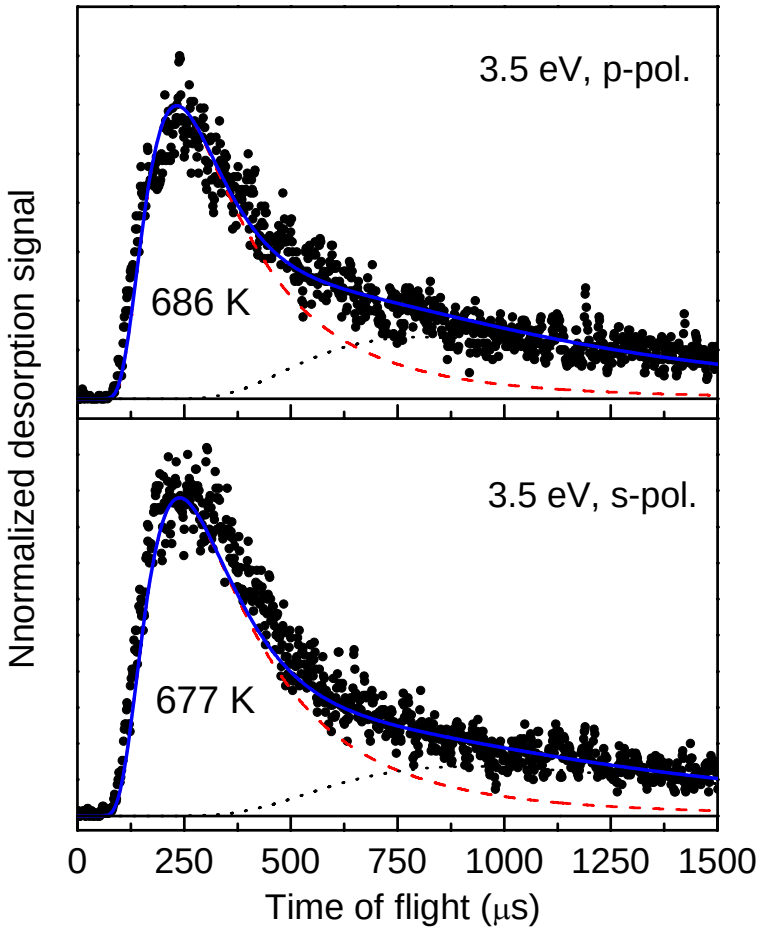

Fig. 4.7. TOF of NO on Ag NPs: on plasmon resonance (upper panel, accumulated 1× 10^{16} photons/cm^2) and off plasmon resonance (lower panel, 1.5× 10^{17} photons/cm^2).

Evolutions of T_t for NO photodesorbed from Ag NPs are compared to those from Ag(111) at various photon energies in Fig. 4.8. The initial values of T_t, resulting mainly from NO dimers on the Ag NPs, are ~ 700 K; they are ~100 K higher than those from Ag(111). As the peak positions of TOF spectra are almost the same for the Ag NPs and Ag(111), the difference in the initial value of T_t is attributed to the rising part of the TOF spectrum as shown in Fig. 4.5. The T_ts at 3.5 and 4.7 eV after the leveling-off represent the T_t of NO stemming from NO monomers. There, NO dimers are almost depleted because of their larger PCS than that of NO monomers. As was discussed in Chapter 3, T_t can be regarded as a phenomenological parameter reflecting the ratio of concentrations of NO dimers and monomers. The evolution of T_t measured for the Ag NPs at 3.5 eV is

much slower than that for Ag(111), suggesting that the efficiency of the photoinduced dimerization of NO monomers discussed in Chapter 3 is higher on Ag NPs than on Ag(111). This is supported by the lower binding energy of NO monomers on Ag NPs than on Ag(111) (Fig. 4.1) implying a higher NO mobility on Ag NPs than on Ag(111) at low temperatures. Also, NO photodesorbed in a low grazing angle may collide with adjacent Ag NPs, as discussed above, and dimerize with an existing NO monomer. However, at 4.7 eV the T_t measured for Ag NPs rises similarly to the Ag(111) case. This can be explained as follows; the affinity level of the NO monomer spans below 4.0 eV above the Fermi level and both the dimer and the monomer can be photoexcited with 4.7 eV photons. On the other hand, a 3.5 eV photon can access only a part of the affinity level of the monomer and thus photodesorption is less efficient than at 4.7 eV.

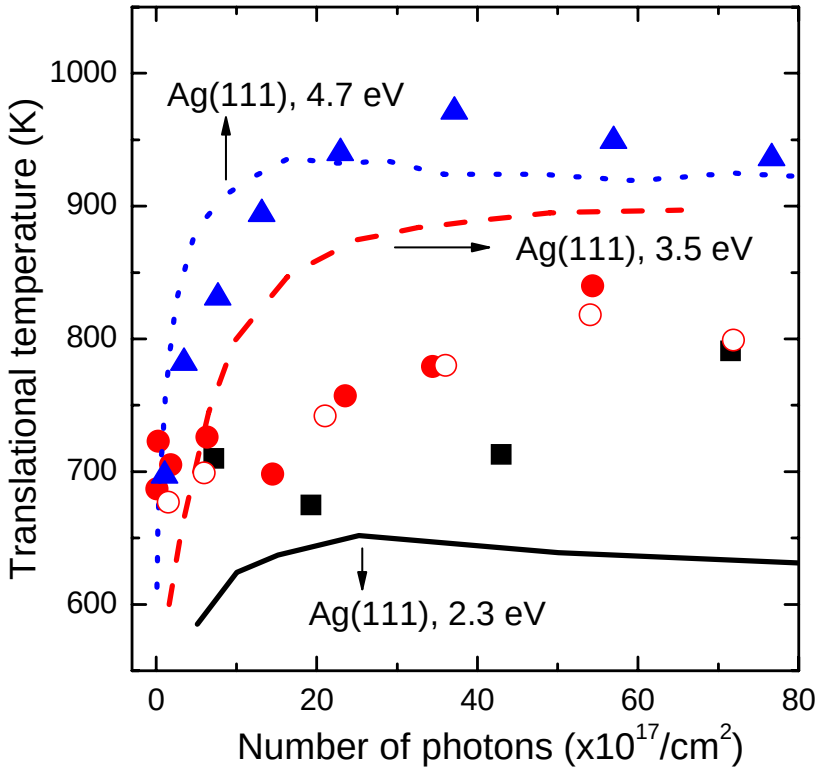

Fig. 4.8. Evolutions of translational temperatures of NO on Ag NPs (symbols) and Ag(111) (curves) using 2.3 eV (squares), 3.5 eV (circles), and 4.7 eV (triangles). Closed and open symbols are for *p* and *s* polarizations, respectively.

4.6. Summary

The thermal- and photo-reactions of NO adsorbed on Ag NPs of ~ 8 nm diameter deposited on a thin Al_2O_3 film formed on NiAl(110) were investigated by TPD, PID, and mass-selected TOF measurements. The overall results were compared with those on Ag(111). The TPD results showed that the affinity levels of the NO dimers and monomers on Ag NPs and Ag(111) are comparable. However, the PCS of NO on the Ag NPs is enhanced compared to that on Ag(111) by a factor of ~ 3 off-plasmon resonant photon energies and by a factor of ~ 15 at the (1,0) mode Mie plasmon resonance (3.5 eV in *p*-polarization). The former enhancement is ascribed to confinement effects due to the particle diameter being shorter than the electron mean free path and the isolation by the thin Al_2O_3 film. The latter is attributable to the surface electric field enhancement effect of plasmon and enhanced electron-hole pairs creation by plasmon decay (Landau damping). The TOF results revealed no difference in photodesorption dynamics between on and off Mie plasmon resonance. The broader TOF spectra of NO photodesorbed from Ag NPs were explained by inhomogeneous adsorption states of NO and collisions of desorbates with adjacent Ag NPs. Furthermore, the evolution of T_t suggested that photoinduced dimerization of NO is more efficient on Ag NPs than on Ag(111), which was explained in terms of higher mobility of NO monomers and collisions with NO photodesorbed from neighboring Ag NPs.

Chapter 5. Femtosecond laser induced desorption of NO from Ag NPs and Ag(111)

This chapter presents femtosecond laser induced desorption of NO from $(NO)_2$ on Ag NPs (width of 8 nm) and Ag(111) by means of the same experimental setup and procedures shown in Chapter 3 compared to nanosecond laser induced desorption. The photodesorption yield from Ag NPs is dramatically enhanced by femtosecond laser irradiation whereas that from Ag(111) is almost unchanged. The enhancement is discussed in terms of the DIMET and Friction models by calculating the number of hot electrons and desorbates.

5.1. Introduction

Femtosecond (fs) laser induced desorption (FID) has been studied for several solid surfaces [64-66, 77, 174-181] and metal films [182]. The most distinctive features compared to nanosecond (ns) laser induced desorption (NID) are as follows: (1) highly enhanced photodesorption yield, (2) laser fluence dependent photodesorption yield and translational temperature (T_t), (3) high vibrational excitation of desorbates, and (4) different branching ratio. The fact that desorption is driven by relaxation of hot electrons has been confirmed by two-pulse correlation experiments [174-176, 178, 180]. To quantitatively describe FID dynamics, two conceptually different models have been proposed. In the model of desorption (or more generally dynamics) induced by multiple electronic transitions (DIMET) [68, 69], many cycles of electronic transition of the adsorbate occur before vibrational excitation is quenched. In the other approach, the Friction model, electronic frictional coupling between an adsorbate and the thermalized substrate hot electrons is assumed [70-75]. Generally, the former is applicable for an

adsorbate resonance state high above the Fermi level and the latter is applied for low lying adsorbate resonances. In the first case, energy transfer happens in a few cycles of electronic transitions, each with large energy transfer: In the second, many small energy transfers occur. These are conceptually different coupling processes.

In this chapter, we present nonthermal photodesorption of NO adsorbed on Ag NPs (~ 8 nm) at ~ 75 K existing as $(NO)_2$ using fs laser pulses. It has been observed in Chapter 3 that the affinity levels of the $(NO)_2$ on Ag(111) and on Ag NPs are qualitatively similar and are located ~ 2 eV above E_F. In the case of NID, the desorption yield of NO on supported Ag NPs is enhanced by a factor of ~ 3 off the plasmon resonance and a factor of ~ 15 at the (1,0) mode of the plasmon resonance (3.5 eV in *p*-polarization), compared to Ag(111). When fs laser pulse irradiation was used, qualitatively similar PCS of NO from $(NO)_2$ on Ag(111) was observed below fs laser intensity ~ 2 mJ/cm^2/shot, whereas the PCS from $(NO)_2$ on Ag NPs was drastically enhanced compared to ns laser irradiation. The enhanced PCS will be discussed based on calculations of the number of hot electrons and reacted $(NO)_2$.

5.2. Experimental

NO gas was dosed to saturation at 75 K on Ag(111) or on 5 Å deposited Ag/ Al_2O_3/NiAl(110) which led to a mean particle diameter of ~ 8 nm and then the sample was cooled down to ~ 30 K. The femtosecond laser systems are described in Chapter 2. Here pulses with duration of ~ 110 fs at 3.1 eV in *p*-polarization at a repetition rate of 50 Hz were used. For NID, the laser beam was expanded threefold using a telescope, to irradiate uniformly over the sample surface, whereas the fs laser beam was used without expansion in order to achieve high fluences at the center of the beam. Since the irradiated spot sizes on the sample have to be larger than the QMS skimmer diameter (2 mm in our setup) for post-irradiation TPD measurements, beam diameters of 5 and 7 mm adjusted by an iris were used for fs and ns laser irradiation, respectively. In order to measure PID and mass-selected TOF, the sample surface normal was oriented into the QMS axis, and the beam incident angle was fixed to 45 degrees. For further experimental details see Chapter 2. The measurements have been done at various fs laser intensities up to ~ 2.1 mJ/cm^2/shot. The beam sizes for photodesorption measurements were 2 and 7 mm diameter for fs and ns laser irradiation, respectively.

5.3. Comparison between femto- and nanosecond laser induced photodesorption

Pre- and post-irradiation TPD results of mass number, m/e = 30 and 44 (inset), from Ag NPs measured after depletion of the photodesorbed NO signal are shown in Fig. 5.1. The fluences were ~ 1 mJ/cm^2 for the ns laser and ~ 0.5 mJ/cm^2 with a 5 mm beam diameter in the center for the fs laser. The latter corresponds to ~ 2 mJ/cm^2 measured for a 2 mm beam diameter in the center due to the Gaussian beam profile. In this chapter, we do not discuss the (photo)chemical reactions of $(NO)_2$ on Ag surfaces (the details can be found in Chapter 3) but stress the similarity of post-irradiation TPD between ns and fs laser irradiation. In both cases the NO peak from $(NO)_2$ located at 86 K was depleted by irradiation, and the broad desorption peak of NO monomers was partly reduced. The remaining NO monomers suggest that multi-photon processes are negligible; otherwise the NO monomers should be depleted because their affinity level is below 4.0 eV above the Fermi level (see Chapter 4). Note that the NO peak at ~ 100 K is due to cracking of N_2O in the QMS.

Post-irradiation TPD allows not only to probe the photoproducts and quantify the reduction of a photoreactive species on the surface, but also to inspect effects of laser heating if there exist photo-inert adsorbates with known desorption temperatures, which may serve as substrate temperature indicators. On Ag surfaces this is the N_2O species produced at photon energy $\leq$ 3.5 eV but barely photodesorbed itself. The areas of N_2O peaks before and after laser irradiation did not change, as shown in the inset. This indicates that the surface temperature of Ag NPs did not exceed their desorption temperature during ns and fs laser irradiation.

The normalized PID results of NO from Ag(111) by irradiating ns and fs laser are compared in Fig. 5.2 (a). The PCSs of NO on Ag(111) are ~ 3.9 and 3.5 × 10^{-18} cm^2 for ns and fs laser irradiation, respectively. Qualitatively similar PCSs were observed at various fs laser intensities up to ~ 2.1 mJ/cm^2/shot. By taking into account the effective absorbance, depending on the incident photon energy, the PCS for fs laser irradiation is slightly higher than that for ns laser irradiation. On the other hand, a remarkable enhancement of the PCS for NO on Ag NPs by fs laser irradiation was observed as shown in Fig. 5.2 (b). Note that the scale of the x-axis (number of irradiated photons) in Fig. 5.2 (a) is 10 times larger than that in Fig. 5.2 (b). Since 3.1 eV light from the ns laser was not available, the results of ns 3.5 eV irradiation in *p*- and *s*-polarization are shown for comparison. The signal decays almost 50 % by a single fs laser shot of ~ 0.2 mJ/cm^2, corresponding to a PCS of about 2000 × 10^{-18} cm^2. This decay is much faster than that for ns 3.5 eV in *s*-polarization irradiation with a PCS of 7.3 × 10^{-18} cm^2 (off plasmon

resonance), and even for 3.5 eV irradiation in *p*-polarization with a PCS of 59×10^{-18} cm^2 (on plasmon resonance). Increasing the fs laser intensity, the desorption signal ratio for the second/first laser shot was increased; however, the PCS was somewhat decreased. This may be due to too high a PCS because the simple PCS estimation is valid only when the change of adsorbate coverage per laser shot is small.

The very high PCS of NO from $(NO)_2$ on Ag NPs in FID manifests itself that the desorption is not due to laser induced thermal desorption. The fs laser intensity adopted in Fig. 5.2 (b) is ~ 1/10 of that used in the experiment on post-TPD, indicating that sample heating should be much lower than reported in ref [166]. Thus, if the desorption is mainly thermal, the signal decay would be slower than that in ref [166], which is not the case.

TOF spectra of NO from Ag NPs (inset) and Ag(111) at different fs laser fluences and the T_t of desorbates calculated by a sum of shifted Maxwell-Boltzmann distributions are shown in Fig. 5.3. The fast component in the TOF spectra is relevant to photodesorption of NO, whereas the slow component is attributable to secondary processes such as collisions among adsorbates/desorbates with the walls of the flight tube. Thus, only the fast component will be discussed. The T_t of NO photodesorbed from $(NO)_2$ reactions has been calculated from the data in the early stage of photoreactions (accumulated for ~ 4×10^{16} photons/cm^2) where the majority of photodesorbed NO stems from $(NO)_2$ (see Chapter 3 and 4), and that from NO monomers has been evaluated at a later stage (accumulated from 1×10^{19} photons/cm^2 to end) where NO dimers are almost depleted. The T_t's of NO from both the dimers and monomers on Ag(111) by fs laser irradiation show almost no fluence dependence and are similar to those by ns laser irradiation. This is consistent with the above PID results in terms of DIET. The same results were observed for NO from NO monomers on Ag NPs. In contrast, the T_t of NO from $(NO)_2$ on Ag NPs shows a strong fluence dependence. The TOF spectra are displayed in the inset of Fig. 5.3. At low intensity ($\leq$ 0.2 mJ/cm^2) the T_t is comparable to that by ns laser irradiation; however, it increases to ~ 1700 K at higher fluences.

5.4. Estimation of photodesorption probability on Ag NPs

Here we estimate the photodesorption probability per hot electron in FID and NID. This quantity will be used to compare the efficiency of photodesorption between ns and fs laser pulses and between Ag NPs and Ag(111), and also to elucidate the photodesorption mechanisms.

In the case of FID with ~ 0.2 mJ/cm^2 at incident angle of 45^o shown in Fig. 5.2 (b), the number of irradiated photons is ~ 3.7×10^{14}/cm^2/shot. Since the density of Ag NPs is ~

4×10^{11}/cm^2 and the Ag coverage is ~ 0.2 about 200 photons irradiate one NP in each shot. Note that this number would be higher in the presence of plasmon excitation because of the so-called antenna effect [183, 184]. However, all of the enhancement will be taken into account later. The absorbance of Ag NPs cannot be simply calculated because of plasmon excitation whose resonance and strength strongly depends not only on their size and shape but also on the supporting material. Thus, let us estimate the absorbance of NPs by multiplying with an enhancement factor, F, the absorbance of a thin film of corresponding mean thickness, expressed by

$$A_t = A_f + (1 - A_f) R_s A_f \qquad (5.\ 1)$$

where $A_f = F(1 - R_b)(1 - e^{-\alpha(E)d})$, $\alpha(E)$ is the photon energy dependent corresponding bulk absorption coefficient related to the refractive index n and extinction coefficient κ by $\sqrt{\varepsilon} = n + i\kappa$, R_b and R_s are the polarization and photon energy dependent reflectivity of the Ag bulk and NiAl, respectively, and d is the film thickness. Here, direct reflection from Ag film and absorption by the alumina film are neglected. The first and second terms denote absorbance of incident light and of light reflected from the NiAl substrate, respectively.

The 2 nm height of NPs at an incident angle of 45^o corresponds to ~ 2.2 nm of mean optical path length. By taking F = ~ 4 obtained from cathodoluminescence results [87], which is attributable to remnants of plasmon excitations, and the optical constants n and κ from ref. [48] and [185], we obtain A_t = ~ 0.15. The number of hot electrons produced per NP by one shot (N_e) is then ~ 30.

The number of desorbed or rather removed $(NO)_2$ per NP per laser shot (N_m) can be deduced from the PID results. The average number of Ag surface atoms per NP is found to be ~ 1000 for the Ag NP size (width) of 8 nm and aspect ratio of 0.5 (height/width). Since the number of $(NO)_2$ per Ag surface atom is assumed to be 0.25 at saturation coverage (due to the two tilted NO molecules consisting of $(NO)_2$ against the surface normal), there would be about 200 $(NO)_2$ molecules per NP. The NO desorption signal decays by about a factor 2 from first to second shot in FID shown in Fig. 5.2 (b) then corresponds to the removal of about 100 molecules in the first shot, i.e. for a total of about 30 hot electrons produced. Thus, the removal probability of $(NO)_2$ on Ag NPs per hot electrons induced by a (low fluence) fs laser pulse is more than 3. Note that the removal probabilities were also estimated for $(NO)_2$ on Ag NPs and Ag(111) in NID with 3.5 eV in *s*-polarization shown in Fig. 5.2 for comparison, then we obtained ~ 0.1 and ~ 0.03, respectively.

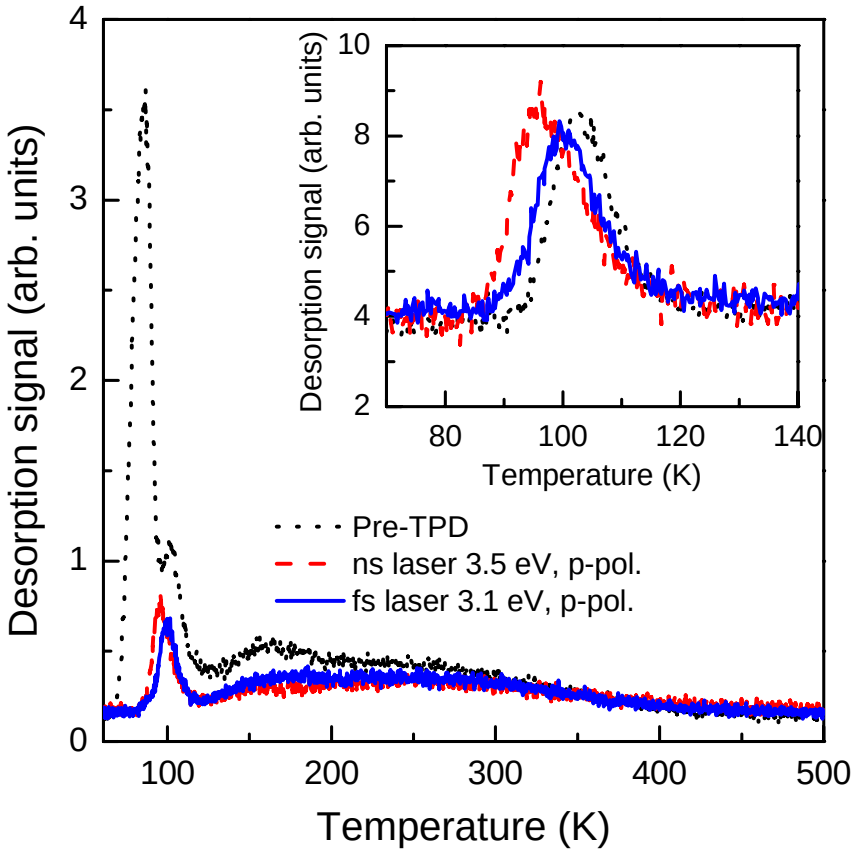

Fig. 5.1. Pre- and post irradiation TPD of NO on Ag NPs, measured at m/e = 30 and 44 (inset). No thermal desorption and multi-photon process.

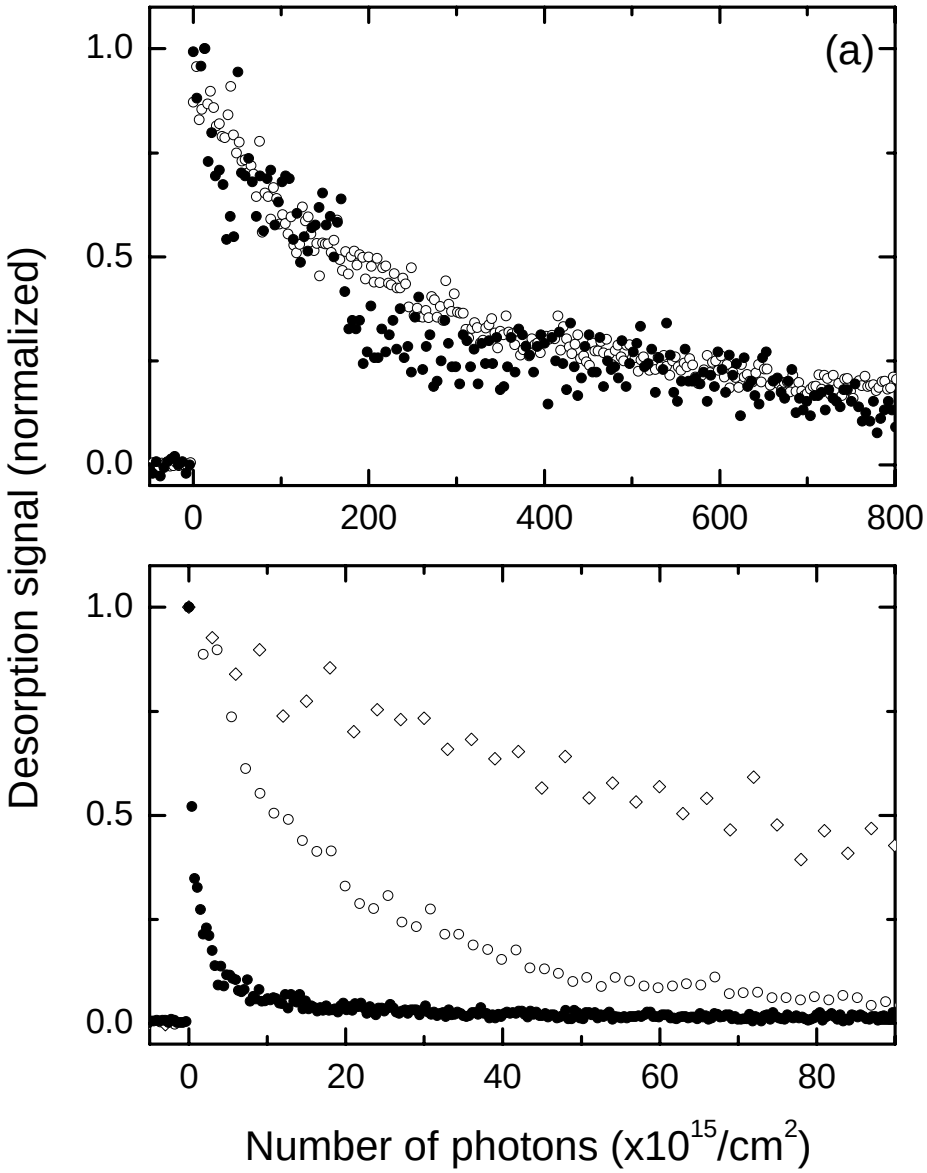

Fig. 5.2. PID results of NO from (a) Ag (111) and (b) Ag NPs with a saturation coverage of NO dosed at 75 K, and then subsequently cooled down to ~ 30 K by means of a ns laser (open symbols, 3.5 eV) and a fs laser (solid circles, 3.1 eV) in *p*-polarized irradiation. Open diamonds are for ns laser in *s*-polarization. The signals are normalized by maximum signal. Fs laser intensities are ~ 2.1 and 0.2 mJ/cm^2 for Ag(111) and Ag NPs, respectively.

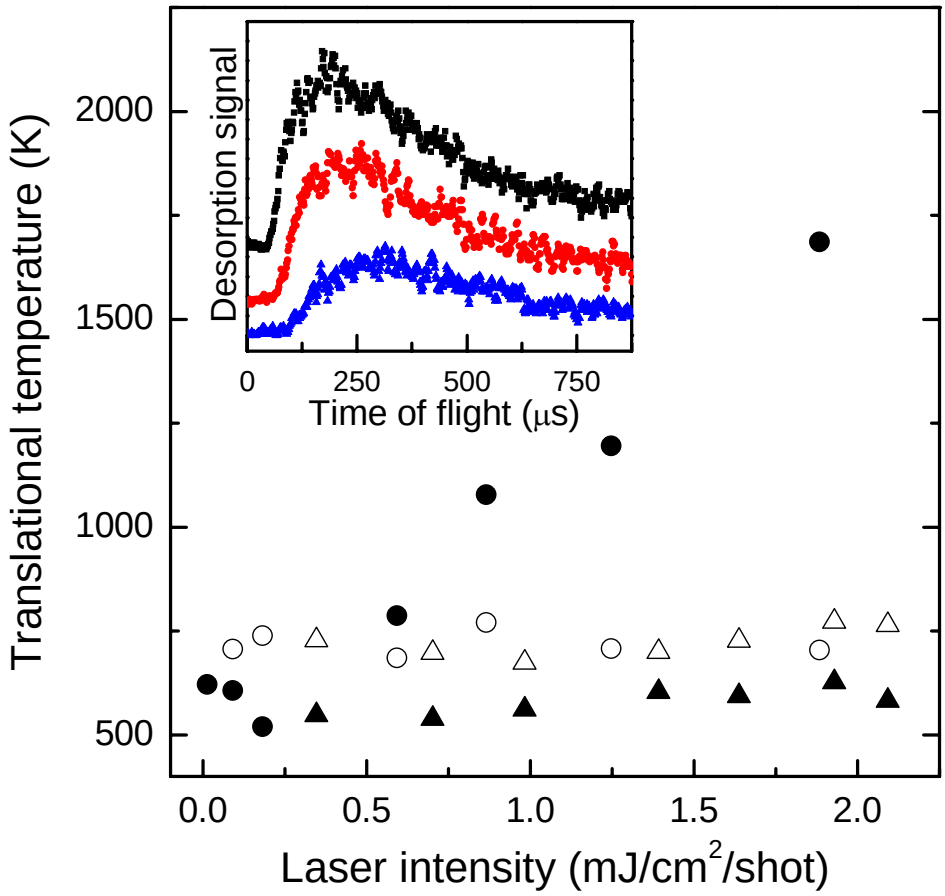

Fig. 5.3. The T_t of NO from $(NO)_2$ (closed symbols) and NO monomer (open symbols) on Ag(111) (triangles) and NPs (circles). TOF spectra of NO from Ag NPs by *p*-polarized 3.1 eV fs laser irradiation is shown in the inset. The desorption signals were accumulated for ~ 4× 10^{16} photons/cm^2. The laser fluences are 0.2, 0.9, and 1.9 mJ/cm^2 from the bottom.

5.5. Discussion and conclusions

Comparison with the H_2O/Ag NP/quartz system

Wolf and coworkers have studied the FID of water adsorbed on quartz supported Ag NPs and concluded from two-pulse correlation measurements that it is a purely thermal process [166]. This is in contrast to our observations in which NO photodesorbs nonthermally and the heating of the Ag NPs on Al_2O_3/NiAl(110) seemed to be negligible. The disagreement with our results is probably due to the very different thermal conductivity of their supporting material and the different absorbance of their Ag NPs. In order to obtain a narrower (1,1) resonance peak, located at 3.1 eV, the NPs were tailored in their experiment, whereas here the Ag NPs were not shaped, and the (1,1) mode of the plasmon is suppressed by image dipole interaction on the NiAl substrate. Therefore, although our fs laser intensity (Fig. 5.1) is comparable to their experimental condition for two-pulse correlation, ~ 1 μJ in 0.3 mm of beam diameter which corresponds to ~ 1.7 mJ/cm^2, the absorbed energy in our Ag NPs is much lower (~ 1/4, as discussed above). Furthermore, our Ag NPs are more efficiently cooled down through the Al_2O_3/NiAl support in our experiment. The surface temperature rise is inversely proportional to the square root of thermal conductivity [186] which depends on substrate temperature as well as material. The thermal conductivities of Ag and supporting materials in our experimental conditions and those in ref [166] are given in Table 5.1. This difference causes more than 1/10 of Ag NP temperature rise. Thus, our Ag NP temperature rise is lower than the desorption temperature of $(NO)_2$ on Ag NPs even though Wolf and coworkers obtained a surface temperature rise of ~ 700 K.

Table 5.1. Thermal conductivity (from ref. [172])

	Ag	Al_2O_3	Ni	Al	Quartz
Thermal conductivity (W cm^{-1} K^{-1})	19.3 [a] 4.60 [c]	60 [b]	9.56 [a]	49.5 [a]	0.2 [d]

The values are given at [a] 30 K, [b] 35 K, [c] 90 K, and [d] 194 K.

Photodesorption mechanism in FID

The estimates given above for FID of NO from $(NO)_2$ on Ag NPs show that a mechanism here cannot be the same as for NID. Obviously the increased desorption

effect must be a consequence of the temporal compression of excitations in the fs case. However, it appears that also a DIMET process is not possible if the single electronic transition process is the same as in NID. The N_e is obviously too small for multiple electronic transitions even if we make the most extreme assumptions. These would be: (1) all hot electrons stem from excitation of filled NP states between E_F and – 0.3 eV [88], (2) all hot electrons are equally effective for formation of a TNI leading to desorption, and (3) all hot electrons have an electron attachment probability close to unity. To be sure, the hot electrons are confined in the NP which means that they scatter inside and can visit the adsorbate layer several times. However an estimate of this effect shows that it is far from sufficient. The lifetime of a hot electron is ~ 5 fs for ~ 8 nm particle size [171], and the Fermi velocity is ~ 1.4×10^6 m/s [187], so that they can only scatter 2 - 4 times to the adsorbate before they decay to too low energy by electron-electron scattering.

The translational energies of desorbates shown in Fig. 5.3 further support the above argument. The T_t of NO from $(NO)_2$ on Ag(111) is independent of fs laser fluence until ≤ ~ 2 mJ/cm^2, suggesting that the desorption process is in the DIET regime. This agrees well with the absence of any significant difference in PID between ns and fs laser irradiation until ≤ ~ 2 mJ/cm^2. In contrast, the T_t of NO from $(NO)_2$ on Ag NPs strongly depends on fs laser fluence. At very low intensity (~ 0.01 mJ/cm^2) the T_t is the same as NID from $(NO)_2$ on Ag NPs (680 ± 50K, see Chapter 4) within experimental error, whereas it is somewhat decreased then increased to ~ 1700 K at ~ 2 mJ/cm^2. We stress that the T_t from $(NO)_2$ on Ag NPs in FID at ~ 0.2 mJ/cm^2 is slightly lower than that in NID even though the PCS is dramatically enhanced. Since the T_t by the DIMET process is expected to be higher than that by the DIET process, this clearly indicates that the DIMET process is not simply the iteration of the DIET process in NID. At ~ 0.2 mJ/cm^2 another desorption mechanism already contributes significantly, and this mechanism should explain the increasing T_t with increasing fs laser intensity.

The second mechanism based on multiple interactions at high excitation density is the friction mechanism. In it the pile-up of energy at the adsorbate occurs by frequent energy exchange of low energy hot electrons not far above the Fermi level, or even by corresponding dipole-dipole interactions. The attractive feature for our fs processes would be that the number of such low energy excited electrons is much larger than those with high energy. The problem is that such an interaction requires some adsorbate density of states at these low energies. While the main LUMO resonance of adsorbed $(NO)_2$ appears to lie around 2 eV above E_F, there could be a tail of excitations caused by coupling of adsorbate and substrate states at much lower energies. For adsorbed NO this is well accepted. Zimmermann and Ho proposed a molecular-orbital bonding scheme for NO/Pt by considering the interaction of the $2\pi^*$ orbitals of NO with the Pt valence bands [188] and found such states. Indeed state-resolved two-pulse correlation measurements [189] are compatible with this. If such an energy level splitting is applicable also for $(NO)_2$ on Ag NPs, it could be effective in our case. Thus, excitation of the high lying

energy state may be the main desorption channel for NID; however, desorption via multiple excitation of a low lying energy state can be opened when the number of thermalized electrons near the Fermi level is large enough, i.e., at high temporal densities of excitations, and more effective at higher fs laser intensity; this also can explain the slightly decreased then increased T_t from $(NO)_2$ on Ag NPs with increasing fs laser intensity shown in Fig. 5.3.

Then, why is FID from Ag NPs extremely high? It has been shown that non-thermalized electrons play a critical role in NID and thermalized electrons drive FID in terms of the Friction model. Fs laser irradiation leads to strong non-equilibrium of electron and phonon temperatures due to the small heat capacity of the electrons compared to the lattice (the so-called two-temperature model [78, 190, 191]). The T_{el} rises several thousand Kelvin, implying that the electron energy distribution is significantly spread above the Fermi level. Only when the T_{el} is high enough, the internal vibrational mode of the adsorbates which can be transferred to the translational energy [192] and/or the adsorbate-substrate bonding mode are highly excited. Since maximum T_{el} is significantly increased [193] and a hot electron gas cooling time is longer [194] for NPs compared to corresponding bulk material, the FID from Ag NPs is drastically enhanced. This indicates that the NP size is one of the parameters affects the ratio between DIET and DIMET/Friction processes, and therefore, the branching ratio in addition to the fs laser intensity. Finally, we emphasize that the fluence dependent dynamics is already dominant in the case of $(NO)_2$ on Ag NPs with a fs laser intensity of ~ 0.2 mJ/cm^2, whereas such processes are not seen for $(NO)_2$ on Ag(111) with ~ 2 mJ/cm^2 .

5.6. Summary

We have observed a drastic enhancement of nonthermal photodesorption of NO from $(NO)_2$ on Ag NPs by irradiation with fs laser pulses. A large PCS enhancement of NO from $(NO)_2$ on Ag NPs in FID has been observed at intensities as low as ~ 0.2 mJ/cm^2. However, the comparison between the N_e and N_m for FID from Ag NPs reveals that multiple electronic transitions of adsorbates in the DIMET sense is not possible if the single electronic transition process is the same as in NID. This led us to propose an additional resonance state near the Fermi level for $(NO)_2$ on Ag NPs with which thermalized electrons can interact in order to apply the Friction model to the FID results. The roles played by thermalized electrons are expected to be important in supported Ag NPs where electron confinement may cause a fast T_{el} rising and slower T_{el} cooling, compared to Ag(111).

Chapter 6. Photodesorption of Xe on Ag nanoparticles

This chapter presents the study of plasmon-induced photodesorption of Xe from Xe monolayers on Ag NPs. It is shown that photoexcitation of alumina supported Ag NPs covered with Xe monolayers by laser light in the (1,0) Mie plasmon resonance can lead to desorption of Xe atoms with hyperthermal energy and chaotic time structure. The chaotic behavior is most likely due to plasmonic coupling between silver NPs. To explain the results, it is argued that the desorption is induced by direct energy transfer to the adsorbate from the Pauli repulsion of the collectively oscillating electrons of the plasmon at the surface. A simple model calculation shows that this is possible. A connection between both effects appears likely.

6.1. Introduction

Metal NPs in the size range 1 to 20 nm have special properties not only in catalysis and other near ground state surface properties, but also with respect to electronic excitations and consequently to photon-induced surface reactions [1, 195]. Important factors are the confinement of electronic and phononic excitations in the particles, which may lead to quite strong changes of their lifetimes. For metal NPs containing quasi-free electrons the most drastic change in the excitation spectrum is the existence of the so-called Mie plasmon [20]. These two effects can concur, leading to special properties of metal NPs for photoreactions [1]. Drastic increases in photoreaction cross sections by excitation in the plasmon resonance, due to the concomitant field enhancement, have been observed [167, 196, 197] with the first work [198] reporting the nonthermal evaporation of Na atoms from Na NPs in their plasmon range. However, to the best of our knowledge no clear indication of a unique action of the plasmon itself has been seen. All cases reported, e.g., of photodesorption, may be understood in terms of cross section enhancement without change of the desorption mechanism, or by strongly enhanced

thermal effects [166]. In the energy range concerned (about 2 to 4 eV) the usual mechanism of nonthermal photodesorption of a chemisorbed adspecies proceeds via TNI mechanism: absorption of the light by the metal substrate creates hot electrons; the latter can form TNI of the adsorbed species with shifted potentials, leading to momentum transfer and ultimately – after backtransfer of the excited electron to the substrate – to desorption [2]. The events appear to be essentially the same in and off the plasmon resonance. The Mie plasmon is known to have a very short lifetime (of around 10 fs or less) [199] and partly decays into electron-hole pairs which can enter this mechanism. Besides these nonthermal processes, confinement of the large energy input into the metal NPs in the plasmon resonance can lead to strong thermal events (diffusion, shape changes, desorption), even in the metal NPs themselves [200, 201].

In this chapter, we report a case of nonthermal desorption where the plasmon is not just a means to drastically increase the energy input into the metal NPs, but where it appears to be desorption-active itself. The initial idea of our investigation was to select a case in which no desorption via TNI is possible, so that such a mechanism should be easy to discern. This is indeed the case. However, the situation turned out not to be that simple; we also found strange chaotic behaviour in desorption. As will be explained we believe that these two characteristics; direct plasmon-induced desorption and chaotic response, are intimately connected.

The selected metal NP system was the very well characterized case of Ag NPs supported on thin alumina films on NiAl(110) (see detail Chapter 2). In order to identify plasmon-induced desorption we studied monolayers of Xe physisorbed on the Ag NPs. The TNI mechanism will not work here because no affinity level is stable on Xe overlayers on metals [202], and desorption via direct excitation of the adatoms [4, 63] is not possible with UV photons due to the large HOMO-LUMO gap (~9 eV) of the Xe layer [203]. In fact, no nonthermal photodesorption of rare gas atoms from bulk metal surfaces has been reported in the UV range so far. Despite these facts, we did find nonthermal desorption. Its very peculiar behaviour points to novel effects.

6.2. Experimental

TPD, mass selected TOF, and PID measurements have been employed in the study presented here. Xe was dosed at ~ 30 K on Ag NPs/Al_2O_3/NiAl(110) and sequentially annealed to 61 K, resulting in a Xe monolayer on both Al_2O_3 and Ag NPs. Nanosecond laser pulses from the second and third harmonics of a Nd:YAG laser (2.3 and 3.5 eV, *p*- and *s*-polarized) and a XeCl excimer laser (4.0 eV, *non*-polarized) were used for

irradiation. The surface normal was oriented into the QMS axis, and the incident angle was ~ 45 degrees. Experimental details can be found in Chapter 2.

6.3. Adsorption of Xe on Ag NPs

TPD results from a bare alumina film and a Ag(111) surface dosed with Xe at ~ 30 K over saturation coverage is shown in Fig. 6.1 (a). The heating rate was set at 0.5 K/second. The desorption peak at ~ 61 K is attributed to the Xe multilayer. The desorption peak from the first monolayer of Xe on the alumina film and the Ag(111) surfaces were observed at ~ 66 and ~ 78 K, respectively.

Fig. 6.1 (b) shows TPD of Xe from Ag NPs of various sizes on alumina films. All the TPD spectra consist of three peaks. The peaks at the lowest, the medium, and the highest desorption temperatures are assigned to desorption of Xe from multilayers of Xe, the first monolayer on the alumina film, and the first monolayer on the Ag NPs, respectively, according to the peak assignments in Fig. 6.1 (a). The integrated desorption signal from the alumina film decreases with increasing Ag deposition time (NP size), indicating a diminished area of the bare alumina film, whereas that from Ag NPs increases. This is consistent with the fact that Ag does not wet on alumina film but forms 3D particles [18]. The Xe desorption peak temperature increases with increasing Ag deposition, indicating that the interaction between Xe and Ag NPs becomes stronger with increasing the particle size. [40].

For photodesorption experiments, the sample was annealed to ~ 61 K in order to remove Xe multilayers and form a monolayer of Xe as shown in Fig. 6.1 (c).

6.4. Hyperthermal chaotic photodesorption of Xe on Ag NPs

TOF spectra of desorbing Xe from 5Å deposited Ag on Al_2O_3, accumulated over 500 laser shots, for the parameters given in the caption, are shown in Fig. 6.2. Desorbing Xe atoms were detectable with fluences (I) above 0.9 mJ/cm^2, for p-polarized light in the resonance, and about five times higher fluences off-resonance and for s-polarized light. Trace (a), on-resonance ($h\nu$=3.5 eV, p-polarized, I=1.1 mJ/cm^2), can be represented well by the sum of two shifted Maxwell-Boltzmann distributions corresponding to mean

translational energies $\langle E_t \rangle = 2k_B T_t$ with T_t = 313 K for the main component and a smaller contribution with T_t = 44 K. For off resonance (e.g. for $h\nu$= 4.0 eV) unpolarized light a signal was barely detectable at I = 1 mJ/cm^2; at 5.7 mJ/cm^2 (Fig. 6.2 (b)) the leading component has T_t = 161 K with some 20 K background. Similar results were obtained at $h\nu$ = 2.3 eV (not shown). In Fig. 6.2 (c), Xe from the bare alumina without AgNPs proves that the much stronger signals from the Ag NP-covered surface indeed are induced by the particles. We estimate that the maximum temperature increase (ΔT) of the substrate surface at I = 5 mJ/cm^2 is about 60 K, based on a laser-induced thermal desorption (LITD) [204] measurement of Xe (T_t = 90 K) from a bare substrate at 30 K. Thus ΔT is estimated to be 12 K for I = 1 mJ/cm^2 as ΔT scales with I. Thermal heating of the Ag NPs may be higher than that of the substrate in principle, but here it was not above 100 K at 1 mJ/cm^2 as confirmed by the absence of photodesorption of physisorbed CO and N_2O, which thermally desorb from the Ag NPs at 60 K and 80 K, respectively. Then, the main conclusion is that on-resonance most of the desorption is nonthermal (termed hyperthermal subsequently), while off-resonance at necessarily higher fluences the probable mechanism is thermal.

Measurement of the evolution of the Xe signals with the number of shots exhibited very unexpected behaviour. Off-resonance at all fluences “normal” behavior was observed as shown in Fig. 6.3 (a): the Xe signal decreases roughly exponentially with the accumulated number of photons and is essentially gone after 300 shots. The noise on the signal is due to instabilities of laser and QMS. Drastically different behavior resulted on-resonance for low fluences (Fig. 6.3 (b), example shown: 1.8 mJ/cm^2. Groups of 500 shots were separated by pauses of ~ 1 min). As seen the signal does not decrease monotonically, but consists of a herd of spikes with strongly fluctuating intensities. When the laser beam is blocked during the pauses, the signal drops to the background level. A trend is seen that the heights of spikes seem to decrease by half after ~2000 shots, and the number of prominent spikes decreases with increasing number of shots. However, the height does not decrease monotonically and often even increases (e.g., in the case shown, see the second bunch of laser shots where three large spikes are observed). It is noticeable that there is an offset at the bottom of spikes which decays slowly. With higher laser fluences, this decaying offset became more significant, suggesting that this offset is due to LITD. It was confirmed in separate experiments that the chaotic behavior is not due to the fluctuation of the laser intensity nor the inhomogeneity of the beam profile. The chaotic behavior is not observed in the case of photodesorption of NO from the AgNPs, for example (there the TNI mechanism is operative) as shown in Chapter 4.

To characterize the chaotic behavior shown in Fig. 6.3 (b) we have calculated the Fourier transforms of the data. The insets in Fig. 6.3 show the resulting power spectra. In the “normal” case (Fig. 6.3 (a)) the power spectrum has a broad decaying distribution. In contrast, for Fig. 6.3 (b) only a flat spectrum is obtained. No peak, i.e., periodicity, can be recognized. Such a flat spectrum is a typical feature for chaotic systems [205].

Both the chaotic behavior and the hyperthermal energies of Xe were suppressed when multilayers of Xe were present, i.e., when the sample was not annealed to 61 K after dosing a thick Xe layer at low temperatures. This indicates that only Xe atoms in direct contact with the Ag NPs are responsible for the hyperthermal and chaotic desorption at resonance with the (1,0) mode of the Mie plasmon (which lies at $h\nu$ = 3.6 eV, *p*-polarization [206]) at low laser fluences. This suggests that the Mie plasmon plays a critical role in the hyperthermal chaotic desorption of Xe from Ag NPs.

Fig. 6.4 displays PID signals from 8, 6, and 4 Å deposited Ag NPs/Al_2O_3 from the bottom, respectively, using 3.5 eV, *p*-polarized light with 10 shots per second. No clear dependence on repetition ratio of input laser beam was observed (see Fig. 6.3 (b) and Fig. 6.4 (b)). However, the strongest desorption signal intensity observed within 2500 laser shots increases with increasing mean particle size. There might be two reasons. First, since photodesorption of Xe is related to plasmon excitation, the increased plasmon strength due to increased number of Ag atoms per NP may play a role. Second, the increased number of Xe atoms on Ag NP is responsible, although that on alumina film is decreased, because only Xe on Ag NPs is desorbed nonthermally. When the stronger laser beam (below 2 mJ/cm^2/shot) was introduced, the maximum desorption signal intensity also increased and the spikes appeared more frequently in earlier time, supporting that the desorption was induced by plasmons (compare Fig. 6.4 (a) and (b)).

In the case of high laser intensity ($\geq$ 2.5 mJ/cm^2/shot), the chaotic PID signals compete with an exponential decay due to LITD. Fig. 6.5 shows incident laser intensity dependence of the PID signal of Xe on 5 Å deposited Ag NPs/Al_2O_3/NiAl(110) using the (1,0) mode of Mie plasmon resonance. As laser intensity increases, the maximum desorption signal becomes stronger and decays more monotonically, which suggests that LITD becomes dominant at higher intensities. In 4.38 mJ/cm^2/shot laser irradiation, the PID signal decays almost exponentially with cross section ~ 2.5×10^{-17} cm^2. These results clearly indicate that the chaotic behaviour and the hyperthermal desorption cannot be explained by thermal heating of Ag NPs.

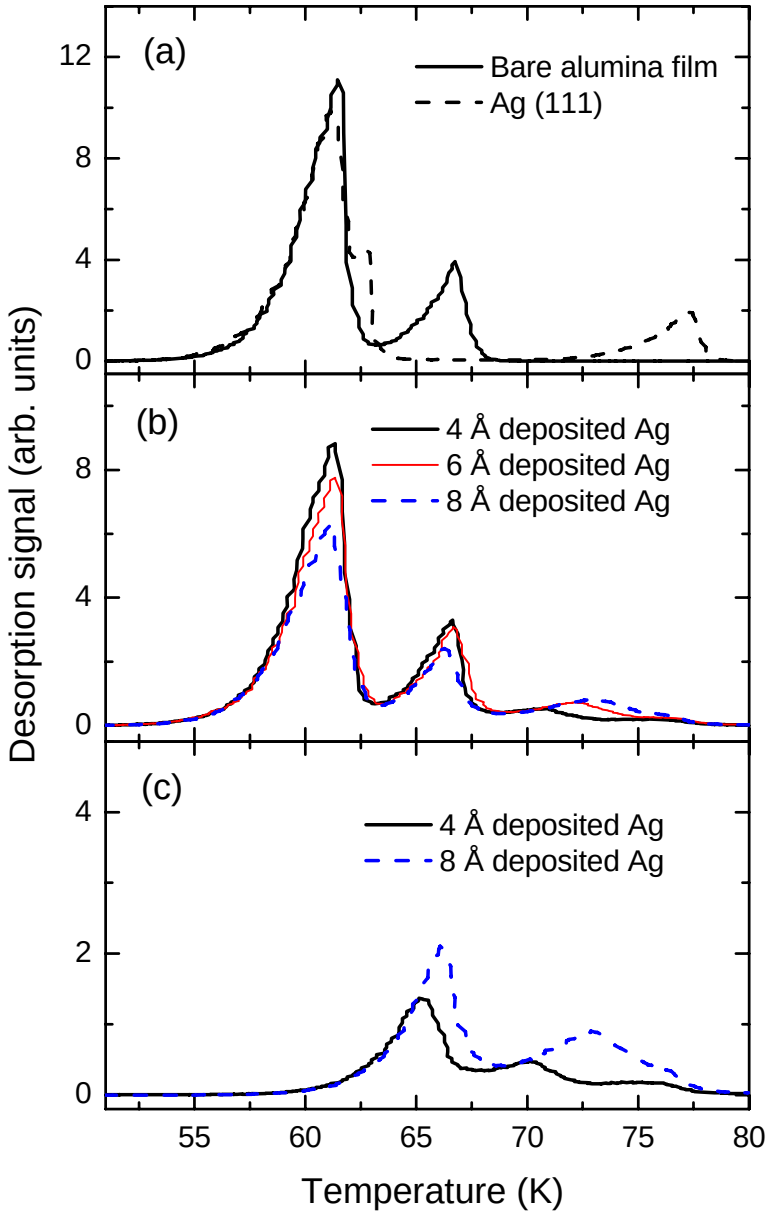

Fig. 6.1. TPD of Xe dosed at ~ 30 K to more than saturation coverage. (a) and (b) before annealing, and (c) after annealing to 61 K. The deposition of 4, 6, and 8 Å Ag correspond to NP size of ~ 8, 9, and 10 nm, respectively. The intensity of Xe signal from Ag(111) is divided by a factor of 2.

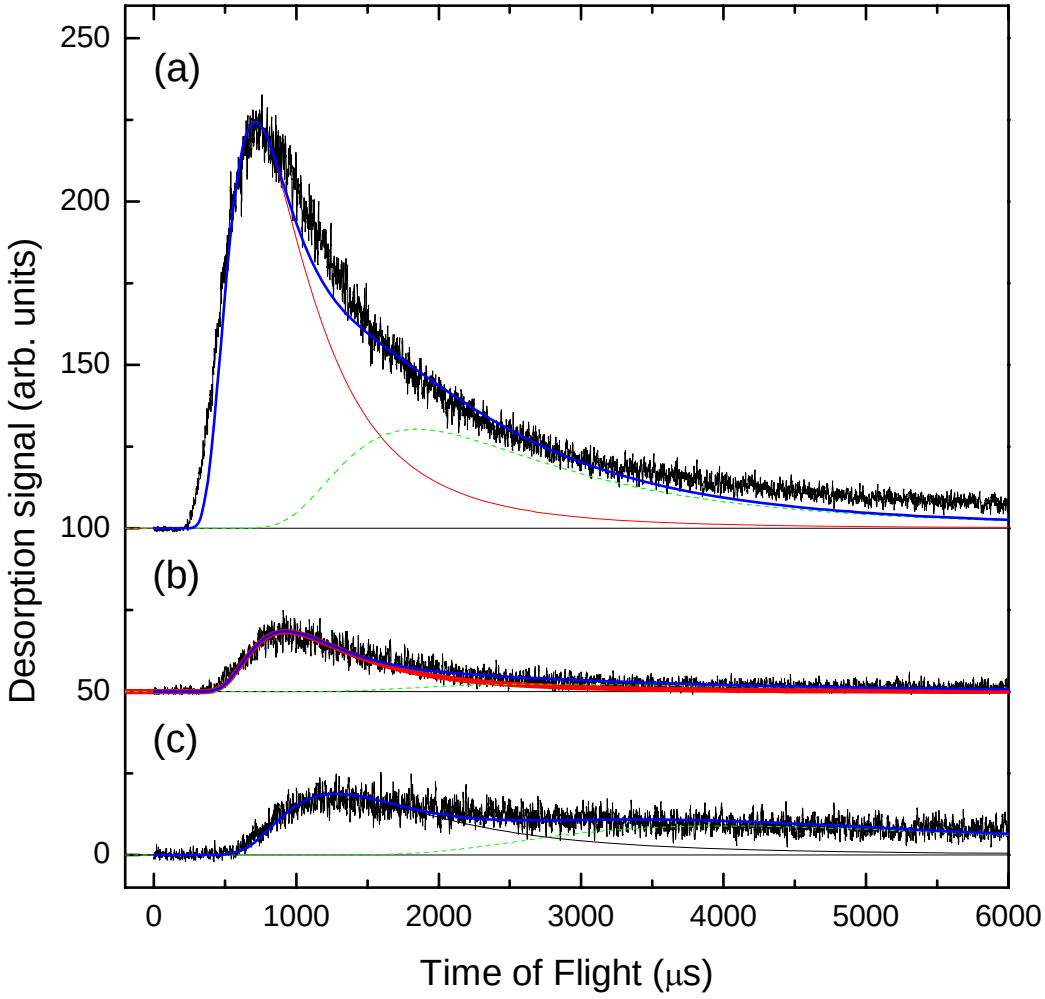

Fig. 6.2. Time-of-flight spectra of desorbing Xe atoms from (a) Xe/5Å deposited Ag NP by excitation in the (1,0) Mie resonance ($h\nu = 3.5$ eV, *p*-pol., 1.1 mJ/cm^2), (b) Xe/5Å deposited Ag NP by off-resonance excitation ($h\nu = 4.0$ eV, *non*-pol., 5.7 mJ/cm^2), and (c) the bare alumina surface (excitation with $h\nu = 3.5$ eV, *p*-pol., 4.9 mJ/cm^2). The results fit by two shifted Maxwell-Boltzmann distributions are shown as thick solid, thin solid, and dashed curves for the sum, the fast, and the slow components, respectively. Intensities of (b) and (c) are magnified by ×2.

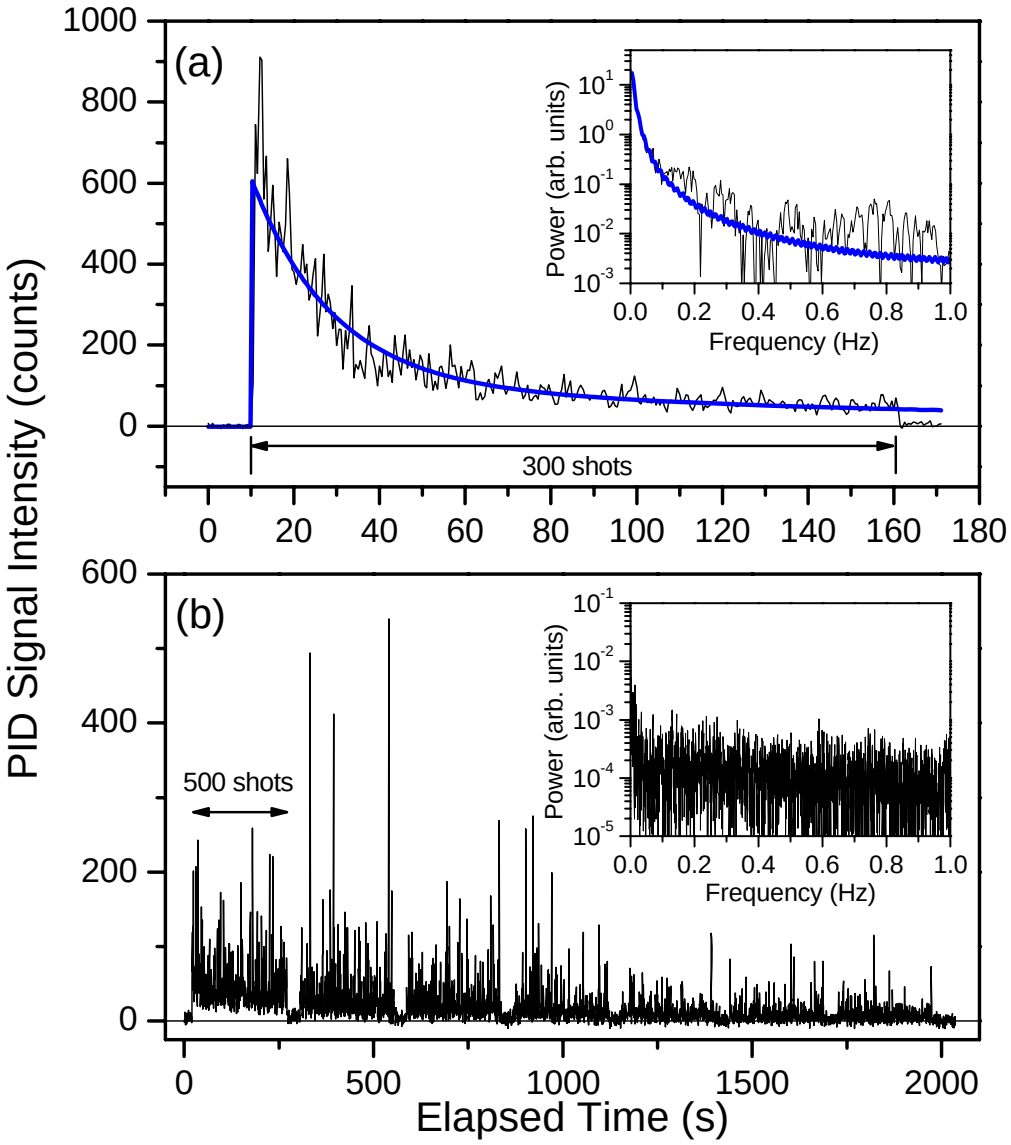

Fig. 6.3. Dependences of the Xe signal intensity on the total number of laser shots (2 shots per second), given as the time after starting the irradiation, for (a) excitation by $h\nu = 2.3$ eV, *p*-pol., 5.7 mJ/cm^2 for 300 continuous shots and (b) excitation by $h\nu = 3.5$ eV, *p*-pol., 1.8 mJ/cm^2, with 1-minute pauses after each 500 shots. The numbers of laser shots are shown by arrows as guide. The insets show the power spectra of the data obtained by Fourier transformation.

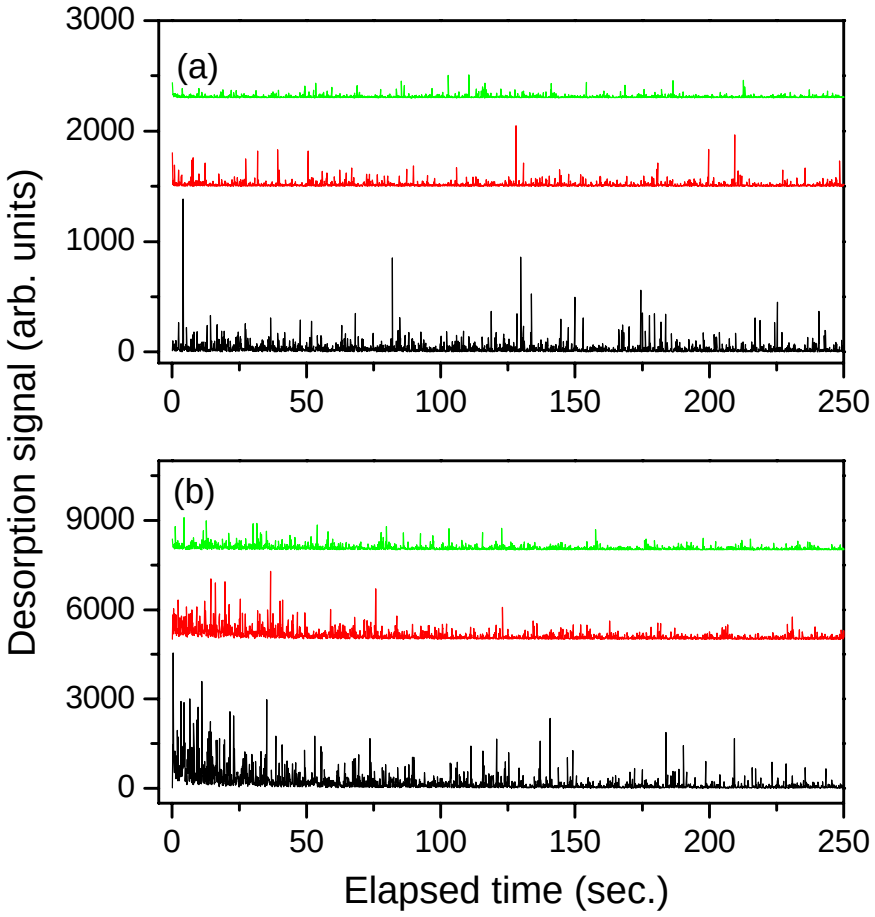

Fig. 6.4. Dependencies of the Xe signal intensity on the total number of laser shots (3.5 eV, *p*-polarized, 10 shots per second) from 8, 6, and 4 Å deposited Ag NPs/Al_2O_3 from the bottom, respectively. (a) 0.8 mJ/cm^2/shot(b) 1.4 mJ/cm^2/shot

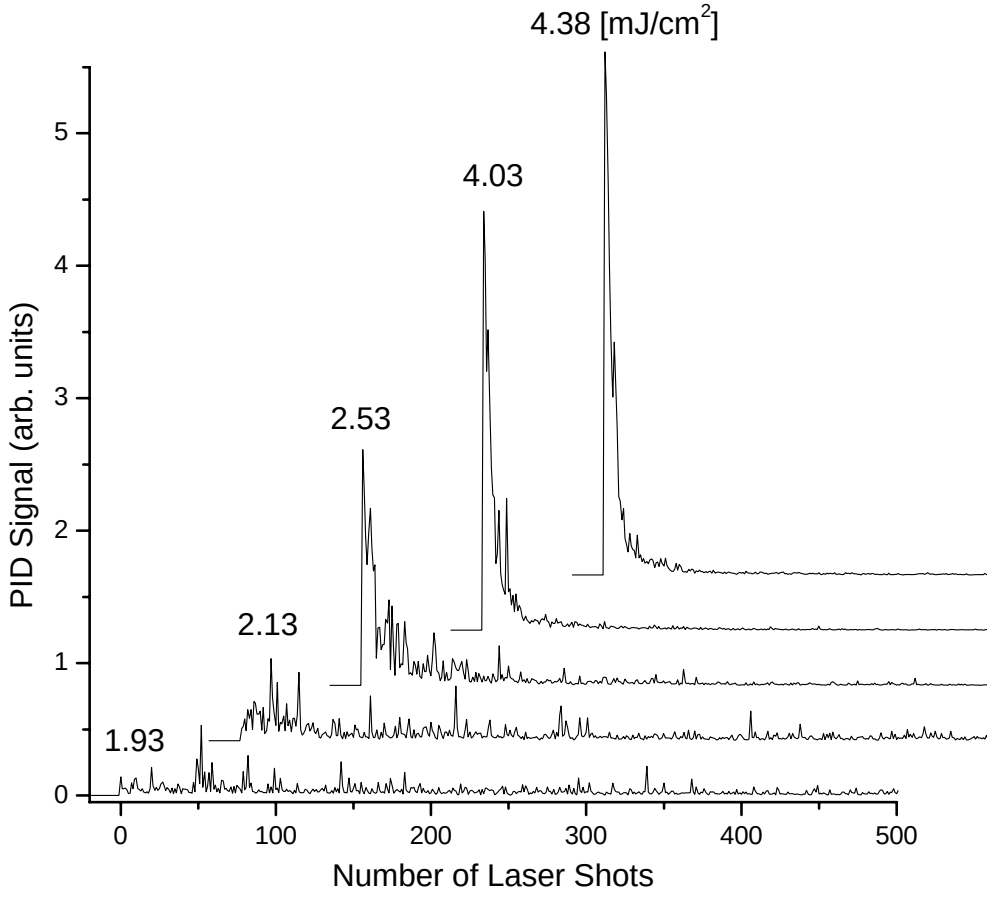

Fig. 6.5. Input laser intensity dependence of PID signal from Xe on 5 Å deposited Ag NPs/Al_2O_3/NiAl(110) using 3.5 eV, *p*-polarized laser beam.

6.5. Photodesorption mechanism

The two outstanding and at least concurring (if not connected) features which should be explained are the hyperthermal desorption under resonant plasmon excitation and its chaotic behavior. The latter property suggests that we have a case of plasmon coupling as derived by Stockman from calculations [27, 207-211]. He has shown that the interaction of the plasmon fields of neighboring particles can lead to strong localization of excitation on a small number of particles ("hotspots"), which also leads to a drastic increase of the plasmon lifetime. While this effect is most obvious for fs excitation and fractal particle distributions, it does exist also for continuous wave excitation. If a small part of our Ag NP ensembles has the fitting properties, then such a strong but erratic removal of Xe for a comparatively small part of the total coverage is understandable. Fluctuations of the coupled fields then may introduce the chaotic behavior.

However, if we maintain that this type of desorption is hyperthermal, i.e., does not result from thermal heating of AgNPs but from an electronic action of the plasmon itself, a new mechanism of plasmon-induced desorption is needed as the usual mechanisms do not work here (see above). We propose that this is due to the modulation of the Pauli repulsion which defines the adsorption potential of Xe together with the van der Waals (vdW) attraction. To first approximation, the vdW attraction, which is established by the long-range dispersion force integrated over all Ag atoms of the AgNP, stays constant, whereas the Pauli repulsion, which stems from the short-range interaction between electrons of Xe and s-electrons spilling out from the AgNP surface, oscillates at the plasmon frequency. Under the plasmon excitation, the induced Pauli exclusion exerts a strong repulsive force on Xe towards the vacuum at the frequency of the plasmon (~1 fs) which is much higher than the natural frequency of the ground state Xe (some ps). Although the impulse per plasmon cycle is small, Xe can be desorbed if it accumulates a sufficient momentum. A similar picture in terms of integrating over many small energy transfers has been used in the frictional or DIMET model [76, 77] of electronically induced desorption; our model is very different in terms of the physical nature of the acting forces, however. Also, it is very different from the mechanism proposed [212] for the plasmon-mediated acceleration of (thermally evaporated) Ag^+ ions from Ag [213] by inverse bremsstrahlung.

In order to check the above mechanism, molecular dynamics simulations were performed. A potential in the Born-Mayer form is given by

$$V(z) = A\exp(-Kz) - \frac{C_3}{(z - z_0)^3} \tag{6.1}$$

where z is the Xe-surface distance, A and K are parameters of Pauli repulsion, C_3 the dispersion coefficient, and z_0 is the vdW reference plane position with the values for Xe on Ag(111) [214]. The first term is a short-ranged repulsive potential arising from the overlap of the electronic clouds of the atom and of the surface. The second term is a long-ranged attractive polarization potential. The C_3 and z_0 are obtained from ref [214], 3277 meV·Å^3, and 1.455 Å, respectively. The depth of the Ag surface-Xe potential and equilibrium position of Xe on Ag are known (211 meV [124], 3.55 Å [215, 216]), which allow us to estimate A and K parameters in the ground state.

The plasmon-modulated Pauli repulsion is implemented as a time-dependent displacement

$$\delta(t) = \delta_0 \sin\left(\frac{2\pi t}{T}\right) \tag{6.2}$$

where δ_0 (> 0) is the amplitude and T is the oscillation period. Then, the displacement can be included in the Pauli repulsion term as

$$V(z,t) = A\exp(-K(z-\delta(t))) - \frac{C_3}{(z-z_0)^3} \tag{6.3}$$

The steeply repulsive part of the potential (we call it the "Pauli wall" because of its spatial coherence over the NP) moves back and forth by δ with time t, and largely coherently in space. The oscillating potentials with δ are presented in Fig. 6.6. The equilibrium position of Xe atom is 3.54 Å. At this equilibrium position the potential energy with δ_0 = 0.4 Å at t/T = 0, 0.125, 0.25, -0.125, and -0.25 are -210, 40, 240, -304, and -324 meV, respectively. The potential energy at t/T = 0.25 is smaller than the absolute value of the lowest potential energy (at t/T = -0.25), indicating that Xe cannot gain energy during oscillation. However, the potential energies at the equilibrium position at t/T = 0.25 are rapidly increased with increasing δ_0, whereas the lowest potential energies are almost constant. The former are 240, 488, 837, 1330 meV, and the latter are -323, -335, -343, -348 meV for δ_0 = 0.4, 0.5, 0.6, 0.7 Å, respectively. This indicates that a Xe atom gains energy from an oscillating PES at $\delta_0 \geq 0.5$, and the gaining of kinetic energy is drastically increased with the increasing δ_0.

The Pauli repulsion exerted on Xe strongly depends on the Xe-Ag distances as shown in Fig. 6.6. The zero point energy motion was considered for the Born-Mayer potential shown in Fig. 6.6 at t/T = 0. The PES near the equilibrium position of Xe on the surface can be approximated to a harmonic potential as shown in Fig. 6.7, and the zero point energy for simple harmonic oscillator is given by

$$E_{zero} = \frac{\hbar\omega}{2} \tag{6.4}$$

where $\hbar$ is the reduced Planck constant and ω is the angular frequency. From the best fitting, the zero point energy is calculated to be ~ 2.4 meV, which is comparable to the value in ref [215, 217], and the closest and farthest position of a Xe atom on the Ag surface are ~3.47 and 3.63 Å, respectively.

The motion of a Xe atom on 1-dimensional potential is simulated by the velocity verlet method with T = 1.14 fs (plasmon frequency at 3.6 eV), and the results are shown in Fig. 6.8. It is found that Xe can be desorbed ($E_t > 0$) when $\delta_0 > 0.6$ Å at the M point in Fig. 6.7, which seems realistic for the plasmon-induced spread of electrons at silver surfaces [40] and $E_t/2k_B$ strongly depends on δ_0; with δ_0 = 0.68 Å and 0.78 Å, $E_t/2k_B$ reaches 300 K and 1000 K, respectively.

It is worth noting that a Xe atom at M point in Fig. 6.7 can gain kinetic energy when $\delta_0 \geq 0.5$ as shown above; however, it can be desorbed only when $\delta_0 > 0.6$ Å. This difference is due to a movement of Xe atoms in the oscillating PES, taken into account in our simulation. The gaining kinetic energy of a Xe atom strongly depends on the Xe-Ag distance (see Fig. 6.6). In the case of δ_0 = 0.5 Å in Fig. 6.6, the Xe atom gains the energy at the equilibrium position, resulting in acceleration of Xe to further the Xe-Ag distance direction. However, at a Xe-Ag distance of ~ 3.7 Å the sum of potential energy when t/T = 0.25 and -0.25 is negative, implying no more energy gain. Therefore, the Xe atom should obtain enough energy before the Xe-Ag distance is ~ 3.7 Å to be desorbed, which is not the case for δ_0 = 0.5 Å.

The simulation results in Fig. 6.8 show that the Xe atom must collide with the "Pauli wall" 250 - 300 times before desorption. If the plasmon lifetime is only 10 fs or less [199], giving only of the order of 10 cycles, then the accumulated energy should not suffice for most realistic parameter sets.

This last conclusion may establish a connection between the plasmonic coupling and the plasmon-induced desorption, via the required plasmon lifetime. Plasmonic coupling should lead to enhanced plasmon lifetimes [210], so the selective conditions of hotspot formation by coupling may enable the plasmon-induced desorption mechanism at the same time.

We realize that there are many rather strong approximations in this rough model and that many refinements are needed. For instance, the real process occurring is most likely not the desorption of individual Xe atoms. Rather, because of the lateral vdW attraction between the Xe atoms, which is not much smaller than that between Ag NP and Xe, patches of Xe are more likely to desorb. This is compensated by the fact that the collective electron motion in the plasmon is in phase over the NP also. In fact, such a

picture may give an additional explanation of the strong irregular bursts. Furthermore, the high field enhancements expected in the hotspots may lead to nonlinear effects which at present we cannot disentangle because of the chaotic behavior but which might be necessary to provide enough energy. On the experimental side, experiments with fs laser pulses, which should make it possible to obtain the time scale of the relevant processes directly, are clearly needed. The suggested model is compared with Friction model in Table 6.1.

Finally, we propose another plausible desorption model. In the presence of the plasmon excitation a Xe atom on Ag NP is highly polarized. Since an electron cloud in the Xe atom asymmetrically oscillates with respect to the surface normal at the plasmon frequency, the polarized Xe can be also accelerated. It might be interesting to simulate molecular dynamics under this mechanism as well for further discussion.

Table 6.1. Comparison between the electronic friction and plasmon induced desorption models presented in this chapter.

	Electronic friction	**Plasmon-induced desorption**
Photon energy dependence	low: friction / high: DIMET	plasmon resonance
Laser pulse width	< 100 fs	~5 ns
Electronic temperature	up to 5000 K	up to ~100 K (8-nm NP)
Energy carrier	hot electrons from bulk	plasmonic *s*-electrons at surface
Coherence	thermalized, incoherent (Friction) / coherent (DIMET)	coherent
Driving force	Langevin noise	Pauli repulsion
Motion of adsobates	Brownian motion, stochastic	Oscillation at plasmon frequency

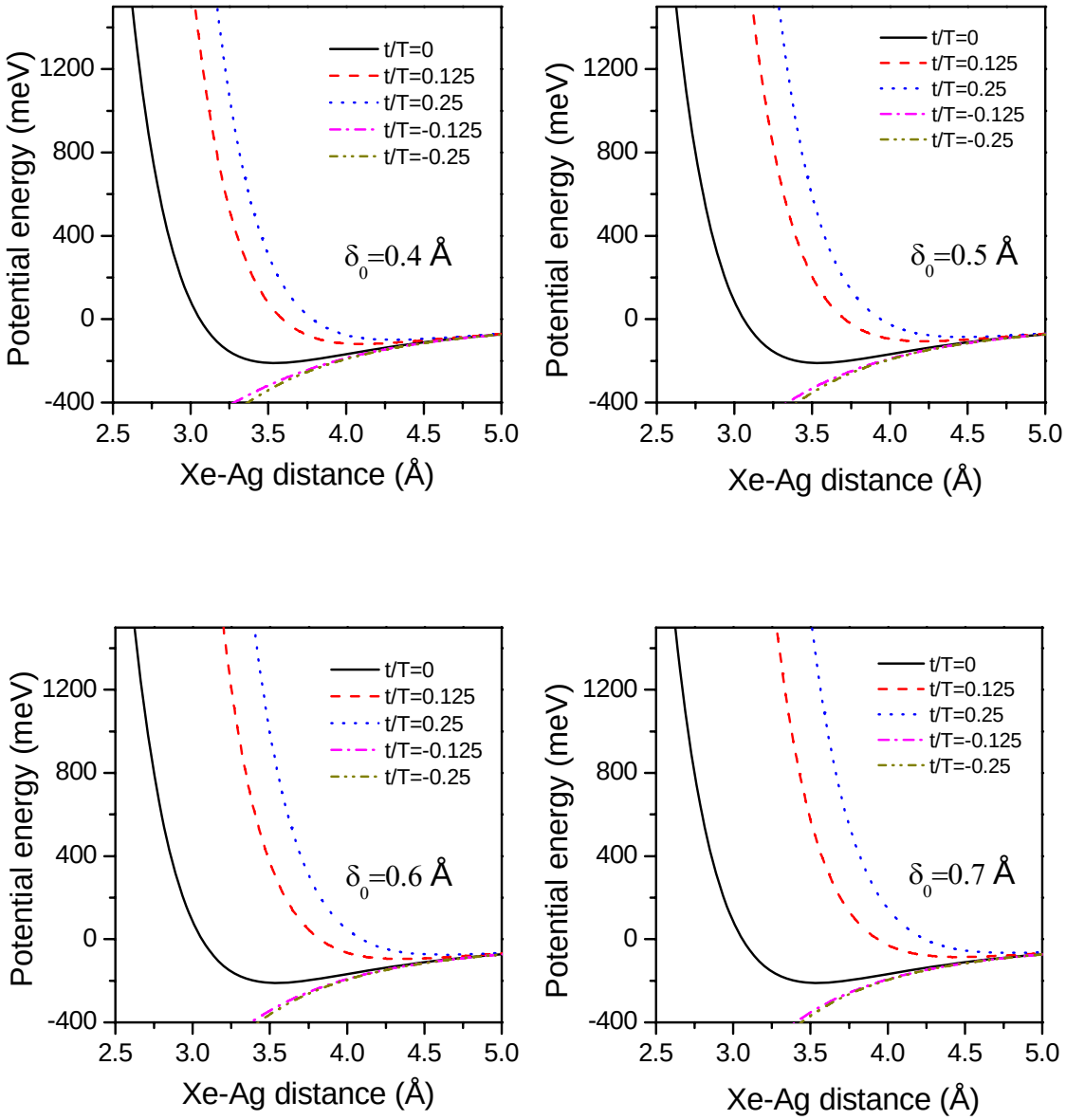

Fig. 6.6. Time dependent oscillating potential energy surfaces for different displacement in equation (6.3). In order to calculate the potential energy surface at t/T = 0, the parameters A = 29958995.75 meV, K = 3.4441 / Å, C_3 = 3277 meV·Å^3, and z = 1.455 Å are used.

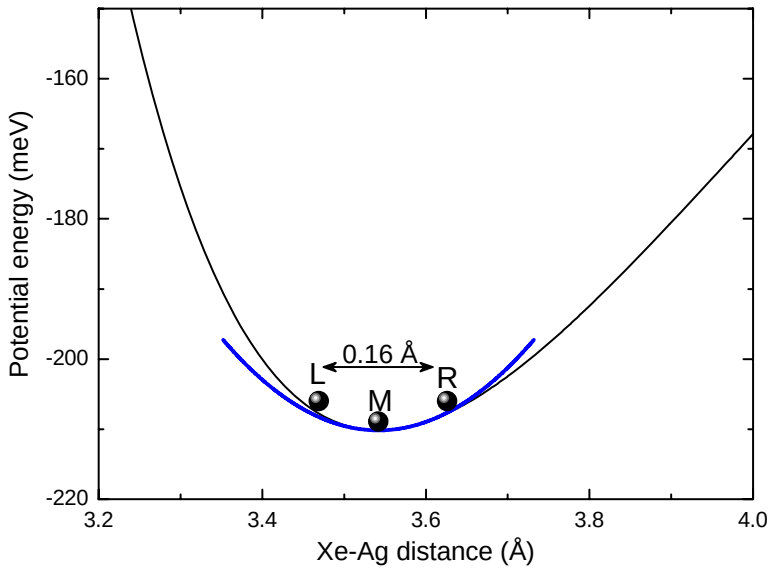

Fig. 6.7. Approximated harmonic potential at the equilibrium position of Xe on the surface. Zero point energy is estimated to be ~ 2.4 meV from the best fitting. L and R represent Xe atom positions, the closest and farthest from the surface due to zero point energy, respectively, and M is for middle position.

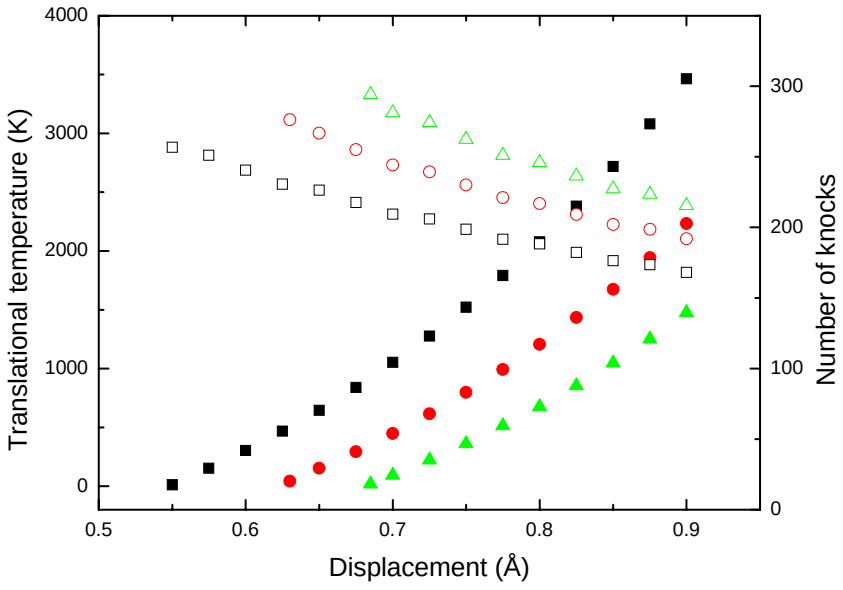

Fig. 6.8. Simulation results of translational temperatures (open symbols) and the number of knocks (closed symbols) for different Xe initial positions at L (squares), M (circles), and R (trangles) as a function of displacement.

6.6. Conclusions

We have observed hyperthermal, chaotic desorption of Xe from Xe monolayers on alumina deposited Ag NPs by resonant excitation of the (1,0) Mie plasmon with ns lasers. The chaotic behavior is observed at low laser fluences which do not cause thermal effects. It is most likely due to plasmonic coupling leading to hotspots of the electric field. Both unexpected characteristics are observed only for Xe monolayers and are quenched in multilayers; this shows that the hyperthermal energy of the desorbing Xe cannot be due to thermal heating of Ag NPs, but must be connected to an electronic mechanism. Since Xe cannot desorb via TNI, we suggest a new mechanism of plasmonic desorption by the accumulated momentum transfer of the repetitive Pauli repulsions between the collective motion of surface electrons and the Xe atom in its shallow physisorption well. A simple model calculation suggests that this mechanism can lead to sufficient energy transfer, but requires an interaction time longer than the plasmon lifetime of a single AgNP. As plasmonic coupling leads to an enhancement of plasmon lifetime, the two effects might well be intimately connected.

Chapter 7. Summary and conclusions

The effects of plasmon excitation and electron confinement on the photoreactions of molecules adsorbed on Ag NPs/Al_2O_3/NiAl(110) have been investigated by a combination of TPD, PID, and mass selected-TOF measurements, and their results are compared with Ag(111). The main findings and conclusions in this thesis are the following.

New photoreaction

The measurements were performed on Ag(111) dosed with NO at 75 K to saturation, leading to NO dimers formation, in order to be served as a reference for the comparisons. Interestingly, however, N_2 in addition to N_2O signals have been observed from NO dimers on Ag(111) by irradiating with 2.3 to 4.7 eV nanosecond laser pulses. Direct photochemical formations of N_2 and N_2O from NO dimers are found by their similar PID signal decay with NO from the NO dimers. A contribution of N_2 (T_t = ~ 2200 K and 600 K) from N_2O on Ag(111) as an intermediate state to the photochemical formation of N_2 (T_t = ~ 5700 K) from NO dimers is excluded by comparing their TOF spectra. For the mechanism of the N_2 formation from NO dimers on Ag(111), we proposed simultaneous splitting of the two N-O bonds in the NO dimers followed by the two nitrogen atoms abstracting each other to form N_2.

Plasmon effect

The PCS of NO from NO dimers on Ag NPs (~ 8 nm width) showed a resonant feature at 3.5 eV in *p*-polarization, at which the Mie plasmon resonance of the (1,0) mode of Ag was located, whereas that from NO dimers on Ag(111) agreed well with the absorbance of Ag(111), indicating a substrate-mediated excitation mechanism. Qualitatively similar TOF spectra of NO from NO dimers on Ag NPs were observed, regardless of on or off the plasmon resonance. Thus, we concluded that the enhancements of the surface electric field and of electron-hole pair creation by plasmon decay increase the PCS of NO from the NO dimers on Ag NPs; however, the photodesorption dynamics are the same. In contrast, the plasmon induced photodesorption of Xe with hyperthermal energy and chaotic time structure was observed from the monolayer of Xe on Ag NPs by nanosecond laser pulses in the (1,0) Mie plasmon resonance. We propose a new

mechanism of plasmon-induced desorption by the accumulated momentum transfer of the repetitive Pauli repulsions between the collective motion of surface electrons and the Xe atom in its shallow physisorption well. A simple model calculation shows that this mechanism can lead to sufficient energy transfer, but requires an interaction time longer than the plasmon lifetime of a single AgNP. As plasmonic coupling leads to an enhancement of plasmon lifetime, the hyperthermal photodesorption of Xe and chaotic behavior might well be intimately connected.

Confinement effect in alumina supported Ag NP on photodesorption

The PCS of NO from NO dimers on Ag NPs (~ 8nm width) was enhanced by a factor of ~ 3 for off-plasmon resonant photon energies in a nanosecond laser excitation, compared to that from NO dimers on Ag(111). This is ascribed to the hot electron confinement effect due to a NP diameter shorter than the electron mean free path and the isolation by the thin alumina film. Moreover, the PCS enhancement of the NO from the NO dimers on Ag NPs compared to that on Ag(111) was a factor of ~ 500 at 3.1 eV in *p*-polarization in the case of femtosecond laser irradiation at intensity as low as ~ 0.2 mJ/cm^2. We suggested that the Friction process already played a role at an intensity of ~ 0.2 mJ/cm^2 for the Ag NPs due to the thermalized electron confinemet, whereas such processes were not observed for the NO dimers on Ag(111) at ~ 2 mJ/cm^2.

Bibliography

1. K. Watanabe, D. Menzel, N. Nilius, and H.J. Freund, *Photochemistry on metal nanoparticles*, Chem. Rev., **106** (2006) 4301.
2. F.M. Zimmermann and W. Ho, *State-Resolved Studies of Photochemical Dynamics at Surfaces*, Surf. Sci. Rep., **22** (1995) 127.
3. X.L. Zhou, X.Y. Zhu, and J.M. White, *Photochemistry at Adsorbate Metal Interfaces*, Surf. Sci. Rep., **13** (1991) 73.
4. D. Menzel and R. Gomer, *Desorption from Metal Surfaces by Low-Energy Electrons*, J. Chem. Phys., **41** (1964) 3311.
5. T. Matsushima, *Angle-resolved measurements of product desorption and reaction dynamics on individual sites*, Surf. Sci. Rep., **52** (2003) 1.
6. P. Avouris and R.E. Walkup, *Fundamental Mechanisms of Desorption and Fragmentation Induced by Electronic-Transitions at Surfaces*, Annu. Rev. Phys. Chem., **40** (1989) 173.
7. H. Nienhaus, *Electronic excitations by chemical reactions on metal surfaces*, Surf. Sci. Rep., **45** (2002) 3.
8. R. Franchy, *Surface and bulk photochemistry of solids*, Rep. Prog. Phys., **61** (1998) 691.
9. P.R. Antoniewicz, *Model for Electron-Stimulated and Photon-Stimulated Desorption*, Phys. Rev. B, **21** (1980) 3811.
10. D.L. Feldheim and C.A. Foss, *Metal nanoparticles: synthesis, characterization, and applications*, 2002, New York: Dekker.
11. T. Wenzel, J. Bosbach, A. Goldmann, F. Stietz, and F. Trager, *Shaping nanoparticles and their optical spectra with photons*, Appl. Phys. B, **69** (1999) 513.
12. G. Seifert, M. Kaempfe, K.J. Berg, and H. Graener, *Femtosecond pump-probe investigation of ultrafast silver nanoparticle deformation in a glass matrix*, Appl. Phys. B, **71** (2000) 795.
13. C. Binns, *Nanoclusters deposited on surfaces*, Surf. Sci. Rep., **44** (2001) 1.
14. M. Baumer and H.J. Freund, *Metal deposits on well-ordered oxide films*, Prog. Surf. Sci., **61** (1999) 127.
15. M. Valden, X. Lai, and D.W. Goodman, *Onset of catalytic activity of gold clusters on titania with the appearance of nonmetallic properties*, Science, **281** (1998) 1647.
16. A. Sanchez, S. Abbet, U. Heiz, W.D. Schneider, H. Hakkinen, R.N. Barnett, and U. Landman, *When gold is not noble: Nanoscale gold catalysts*, J. Phys. Chem. A, **103** (1999) 9573.
17. G.K. Wertheim, S.B. Dicenzo, and D.N.E. Buchanan, *Noble-Metal and Transition-Metal Clusters - the D-Bands of Silver and Palladium*, Phys. Rev. B, **33** (1986) 5384.

18. N. Nilius, N. Ernst, and H.J. Freund, *Photon emission spectroscopy of individual oxide-supported sliver clusters in a scanning tunneling microscope*, Phys. Rev. Lett., **84** (2000) 3994.
19. N. Nilius, A. Corper, G. Bozdech, N. Ernst, and H.J. Freund, *Experiments on individual alumina-supported adatoms and clusters*, Prog. Surf. Sci., **67** (2001) 99.
20. U. Kreibig and M. Vollmer, *Optical properties of metal clusters*, 1994, Berlin; New York: Springer-Verlag.
21. S. Berciaud, L. Cognet, P. Tamarat, and B. Lounis, *Observation of intrinsic size effects in the optical response of individual gold nanoparticles*, Nano Letters, **5** (2005) 515.
22. C.F.A. Negre and C.G. Sancheza, *Atomistic structure dependence of the collective excitation in metal nanoparticles*, J. Chem. Phys., **129** (2008) 034710.
23. C. Sonnichsen, T. Franzl, T. Wilk, G. von Plessen, J. Feldmann, O. Wilson, and P. Mulvaney, *Drastic reduction of plasmon damping in gold nanorods*, Phys. Rev. Lett., **88** (2002) 077402.
24. J.J. Mock, M. Barbic, D.R. Smith, D.A. Schultz, and S. Schultz, *Shape effects in plasmon resonance of individual colloidal silver nanoparticles*, J. Chem. Phys., **116** (2002) 6755.
25. J. Le Perchec, P. Quemerais, A. Barbara, and T. Lopez-Rios, *Why metallic surfaces with grooves a few nanometers deep and wide may strongly absorb visible light*, Phys. Rev. Lett., **100** (2008) 066408.
26. F. Hubenthal, N. Borg, and F. Trager, *Optical properties and ultrafast electron dynamics in gold-silver alloy and core-shell nanoparticles*, Appl. Phys. B, **93** (2008) 39.
27. M.I. Stockman, *Chaos and spatial correlations for dipolar eigenproblems*, Phys. Rev. Lett., **79** (1997) 4562.
28. H.M. Benia, N. Nilius, and H.J. Freund, *Effect of electromagnetic interactions on plasmon excitations in silver particle ensembles*, Surf. Sci., **600** (2006) L128.
29. Yamaguch.T, S. Yoshida, and A. Kinbara, *Effect of Dipole Interaction between Island Particles on Optical Properties of an Aggregated Silver Film*, Thin Solid Films, **13** (1972) 261.
30. P. Royer, J.P. Goudonnet, R.J. Warmack, and T.L. Ferrell, *Substrate Effects on Surface-Plasmon Spectra in Metal-Island Films*, Phys. Rev. B, **35** (1987) 3753.
31. K.P. Charle, L. Konig, S. Nepijko, I. Rabin, and W. Schulze, *The surface plasmon resonance of free and embedded Ag-clusters in the size range 1,5 nm < D < 30 nm*, Crystal Research and Technology, **33** (1998) 1085.
32. R.M. Jaeger, J. Libuda, M. Baumer, K. Homann, H. Kuhlenbeck, and H.J. Freund, *Vibrational Structure of Excited States of Molecules on Oxide Surfaces*, J. Electron Spectrosc. Relat. Phenom., **64-5** (1993) 217.
33. O. Kajimoto, K. Honma, and T. Kobayashi, *Formation of Electronically Excited No and Energy Partitioning in the 193-Nm Photolysis of the No Dimer*, J. Phys. Chem., **89** (1985) 2725.
34. K. Mase, S. Mizuno, Y. Achiba, and Y. Murata, *Photostimulated Desorption of No on Pt(001) Studied with a Multiphoton Ionization Technique*, Surf. Sci., **242** (1991) 444.

35. G. Eichhorn, M. Richter, K. AlShamery, and H. Zacharias, *Vibrational population in femtosecond UV laser desorption of NO from NiO(100)*, Surf. Sci., **368** (1996) 67.
36. K. Wandelt, *The local work function: Concept and implications*, Appl. Surf. Sci., **111** (1997) 1.
37. G.K. Wertheim, *Core-Electron Binding-Energies in Free and Supported Metal-Clusters*, Z. Phys. B, **66** (1987) 53.
38. C. Voisin, N. Del Fatti, D. Christofilos, and F. Vallee, *Ultrafast electron dynamics and optical nonlinearities in metal nanoparticles*, J. Phys. Chem. B, **105** (2001) 2264.
39. C. Voisin, D. Christofilos, N.D. Fatti, F. Vallee, B. Prevel, E. Cottancin, J. Lerme, M. Pellarin, and M. Broyer, *Size-dependent electron-electron interactions in metal nanoparticles*, Phys. Rev. Lett., **85** (2000) 2200.
40. A. Liebsch, *Surface-Plasmon Dispersion and Size Dependence of Mie Resonance: Silver Versus Simple Metals*, Phys. Rev. B, **48** (1993) 11317.
41. F. Evers, C. Rakete, K. Watanabe, D. Menzel, and H.J. Freund, *Two-photon photoemission from silver nanoparticles on thin alumina films: Role of plasmon excitation*, Surf. Sci., **593** (2005) 43.
42. S.K. So and W. Ho, *Resonant Photodissociation of Mo(Co)6 Adsorbed on Graphite and Ag(111)*, J. Chem. Phys., **95** (1991) 656.
43. A. Peremans, K. Fukutani, K. Mase, and Y. Murata, *UV Photodesorption of CO from Pt(001) at 193 nm Investigated by State-Selective Detection*, Surf. Sci., **283** (1993) 189.
44. K. Watanabe, K. Sawabe, and Y. Matsumoto, *Adsorbate-localized excitation in surface photochemistry: Methane on Pt(111)*, Phys. Rev. Lett., **76** (1996) 1751.
45. K. Watanabe, *Laser-induced Reactions of Methane Adsorbed on Transition Metal surfaces*, PhD thesis, The Graduate University for Advanced Studies in Japan (1998)
46. X.Y. Zhu, J.M. White, M. Wolf, E. Hasselbrink, and G. Ertl, *Polarization Probe of Excitation Mechanisms in Surface Photochemistry*, Chem. Phys. Lett., **176** (1991) 459.
47. L.J. Richter, S.A. Buntin, D.S. King, and R.R. Cavanagh, *Constraints on the Use of Polarization and Angle-of-Incidence to Characterize Surface Photoreactions*, Chem. Phys. Lett., **186** (1991) 423.
48. E.D. Palik, *Handbook of optical constants of solids*, 1985, Orlando: Academic Press.
49. R.T. Kidd, D. Lennon, and S.R. Meech, *Comparative study of the primary photochemical mechanisms of nitric oxide and carbonyl sulfide on Ag(111)*, J. Phys. Chem. B, **103** (1999) 7480.
50. S.A. Buntin, L.J. Richter, R.R. Cavanagh, and D.S. King, *Optically Driven Surface-Reactions: Evidence for the Role of Hot-Electrons*, Phys. Rev. Lett., **61** (1988) 1321.
51. L.J. Richter, S.A. Buntin, R.R. Cavanagh, and D.S. King, *Non-Boltzmann Rotational and Inverted Spin Orbit State Distributions for Laser-Induced Desorption of No from Pt(111)*, J. Chem. Phys., **89** (1988) 5344.

52. K. Fukutani, A. Peremans, K. Mase, and Y. Murata, *Photodesorption of No from Pt(001) at Lambda = 193, 248, and 352-Nm*, Phys. Rev. B, **47** (1993) 4007.
53. K. Fukutani, A. Peremans, K. Mase, and Y. Murata, *Photo-Stimulated Desorption of NO from a Pt(001) Surface*, Surf. Sci., **283** (1993) 158.
54. F. Weik, A. Demeijere, and E. Hasselbrink, *Wavelength Dependence of the Photochemistry of O_2 on Pd(111) and the Role of Hot-Electron Cascades*, J. Chem. Phys., **99** (1993) 682.
55. B. Hellsing and V.P. Zhdanov, *Photoinduced Substrate-Mediated Dissociation of O_2 on Pd(111): Evaluation of the Survival Probability*, Chem. Phys. Lett., **226** (1994) 331.
56. R.W. Schoenlein, W.Z. Lin, J.G. Fujimoto, and G.L. Eesley, *Femtosecond Studies of Nonequilibrium Electronic Processes in Metals*, Phys. Rev. Lett., **58** (1987) 1680.
57. E. Knoesel, A. Hotzel, and M. Wolf, *Ultrafast dynamics of hot electrons and holes in copper: Excitation, energy relaxation, and transport effects*, Phys. Rev. B, **57** (1998) 12812.
58. S. Ogawa, H. Nagano, and H. Petek, *Hot-electron dynamics at Cu(100), Cu(110), and Cu(111) surfaces: Comparison of experiment with Fermi-liquid theory*, Phys. Rev. B, **55** (1997) 10869.
59. M. Bonn, D.N. Denzler, S. Funk, M. Wolf, S.S. Wellershoff, and J. Hohlfeld, *Ultrafast electron dynamics at metal surfaces: Competition between electron-phonon coupling and hot-electron transport*, Phys. Rev. B, **61** (2000) 1101.
60. J.A. Stratton, *Electromagnetic theory*, 1941, New York, London: McGraw-Hill.
61. Z. Ying and W. Ho, *Photogenerated-Charge-Carrier-Induced Surface-Reaction: NO on Si(111)7X7*, Phys. Rev. Lett., **60** (1988) 57.
62. S.K. So, R. Franchy, and W. Ho, *Photodesorption of NO from Ag(111) and Cu(111)*, J. Chem. Phys., **95** (1991) 1385.
63. P.A. Redhead, *Interaction of Slow Electrons with Chemisorbed Oxygen*, Can. J. Phys., **42** (1964) 886.
64. F.J. Kao, D.G. Busch, D.G. Dacosta, and W. Ho, *Femtosecond Versus Nanosecond Surface Photochemistry: O_2+CO on Pt(111) at 80 K*, Phys. Rev. Lett., **70** (1993) 4098.
65. J.A. Prybyla, T.F. Heinz, J.A. Misewich, M.M.T. Loy, and J.H. Glownia, *Desorption Induced by Femtosecond Laser-Pulses*, Phys. Rev. Lett., **64** (1990) 1537.
66. L.M. Struck, L.J. Richter, S.A. Buntin, R.R. Cavanagh, and J.C. Stephenson, *Femtosecond laser-induced desorption of CO from Cu(100): Comparison of theory and experiment*, Phys. Rev. Lett., **77** (1996) 4576.
67. S. Wagner, C. Frischkorn, M. Wolf, M. Rutkowski, H. Zacharias, and A.C. Luntz, *Energy partitioning in the femtosecond-laser-induced associative D_2 desorption from Ru(0001)*, Phys. Rev. B, **72** (2005) 205404.
68. J.A. Misewich, T.F. Heinz, and D.M. Newns, *Desorption Induced by Multiple Electronic-Transitions*, Phys. Rev. Lett., **68** (1992) 3737.
69. P. Saalfrank, *Open-system quantum dynamics for laser-induced DIET and DIMET*, Surf. Sci., **390** (1997) 1.

70. D.M. Newns, T.F. Heinz, and J.A. Misewich, *Desorption by Femtosecond Laser-Pulses: An Electron-Hole Effect?* Progress of Theoretical Physics Supplement, **106** (1991) 411.
71. C. Springer, M. Headgordon, and J.C. Tully, *Simulations of Femtosecond Laser-Induced Desorption of Co from Cu(100)*, Surf. Sci., **320** (1994) L57.
72. F. Budde, T.F. Heinz, A. Kalamarides, M.M.T. Loy, and J.A. Misewich, *Vibrational Distributions in Desorption Induced by Femtosecond Laser-Pulses - Coupling of Adsorbate Vibration to Substrate Electronic Excitation*, Surf. Sci., **283** (1993) 143.
73. D.M. Newns, *Electron-Hole Pair Mechanism for Excitation of Intramolecular Vibrations in Molecule Surface Scattering*, Surf. Sci., **171** (1986) 600.
74. H. Kasai and A. Okiji, *Electron-Hole Pair Mechanism for Excitation of Intramolecular Vibrations in Molecule Surface Scattering*, Surf Sci, **225** (1990) L33.
75. P. Avouris and B.N.J. Persson, *Excited-States at Metal-Surfaces and Their Nonradiative Relaxation*, J. Phys. Chem., **88** (1984) 837.
76. M. Brandbyge, P. Hedegard, T.F. Heinz, J.A. Misewich, and D.M. Newns, *Electronically Driven Adsorbate Excitation Mechanism in Femtosecond-Pulse Laser-Desorption*, Phys. Rev. B, **52** (1995) 6042.
77. C. Frischkorn and M. Wolf, *Femtochemistry at metal surfaces: Nonadiabatic reaction dynamics*, Chem. Rev., **106** (2006) 4207.
78. S.I. Anisimov, Kapeliov.Bl, and T.L. Perelman, *Electron-Emission from Surface of Metals Induced by Ultrashort Laser Pulses*, Zh. Exp. Theor. Fiz., **66** (1974) 776.
79. R.H.M. Groeneveld, R. Sprik, and A. Lagendijk, *Femtosecond Spectroscopy of Electron-Electron and Electron-Phonon Energy Relaxation in Ag and An*, Phys. Rev. B, **51** (1995) 11433.
80. C. Rakete, *Photoemission und Photodesorption von NO auf NiO und Silberclustern mit Femtosekunden-Laserpulsen*, PhD thesis, Freien Universitat (2003)
81. J. Libuda, F. Winkelmann, M. Baumer, H.J. Freund, T. Bertrams, H. Neddermeyer, and K. Muller, *Structure and Defects of an Ordered Alumina Film on Nial(110)*, Surf. Sci., **318** (1994) 61.
82. H. Isern and G.R. Castro, *The Initial Interaction of Oxygen with a NiAl(110) Single Crystal: A LEED and AES Study*, Surf. Sci., **211** (1989) 865.
83. R.M. Jaeger, H. Kuhlenbeck, H.J. Freund, M. Wuttig, W. Hoffmann, R. Franchy, and H. Ibach, *Formation of a Well-Ordered Aluminum Oxide Overlayer by Oxidation of NiAl(110)*, Surf. Sci., **259** (1991) 235.
84. X.P. Xu and D.W. Goodman, *Metal Deposition onto Oxides: An Unusual Low Initial Sticking Probability for Copper on SiO_2*, Appl. Phys. Lett., **61** (1992) 1799.
85. J.B. Zhou, H.C. Lu, T. Gustafsson, and E. Garfunkel, *Anomalously Weak Adsorption of Cu on SiO_2 and MgO Surfaces*, Surf. Sci., **293** (1993) L887.
86. D.G. Vancampen and J. Hrbek, *Silver on Alumina: Adsorption and Desorption Study of Model Catalysts*, J. Phys. Chem., **99** (1995) 16389.

87. W. Drachsel, M. Adelt, N. Nilius, and H.J. Freund, *Cathodoluminescence of small silver particles on Al_2O_3/NiAl (110)*, J. Electron Spectrosc. Relat. Phenom., **122** (2002) 239.
88. F. Evers, *Comparative study of silver nanoparticles and silver(111) by means of femtosecond laser pulses*, PhD thesis, Technische Universitat (2006)
89. C.T. Campbell, *Ultrathin metal films and particles on oxide surfaces: Structural, electronic and chemisorptive properties*, Surf. Sci. Rep., **27** (1997) 1.
90. N. Nilius, *http://www.fhi-berlin.mpg.de/cp/sps/*.
91. K. Christmann, *Introduction to surface physical chemistry*, 1991, Darmstadt: Steinkopff Verlag.
92. J.T. Yates, *Experimental innovations in surface science: a guide to practical laboratory methods and instruments*, 1998, New York: AIP Press: Springer.
93. P.A. Redhead, *Thermal desorption of gases*, Vacuum, **12** (1962) 203.
94. H. Schlichting and D. Menzel, *Techniques for Attainment, Control, and Calibration of Cryogenic Temperatures at Small Single-Crystal Samples under Ultrahigh-Vacuum*, Rev. Sci. Instrum., **64** (1993) 2013.
95. G. Cosma and R. David, *Dynamical Parameters of Desorbing Molecules*, Surf. Sci. Rep., **5** (1985) 145.
96. W.A. Brown and D.A. King, *NO chemisorption and reactions on metal surfaces: A new perspective*, J. Phys. Chem. B, **104** (2000) 2578.
97. Y. Arikawa, T. Asayama, Y. Moriguchi, S. Agari, and M. Onishi, *Reversible N-N coupling of NO Ligands on dinuclear ruthenium complexes and subsequent N2O evolution: Relevance to nitric oxide reductase*, J. Am. Chem. Soc., **129** (2007) 14160.
98. A. Bogicevic and K.C. Hass, *NO pairing and transformation to N_2O on Cu(111) and Pt(111) from first principles*, Surf. Sci., **506** (2002) L237.
99. J.S. Stamler, D.J. Singel, and J. Loscalzo, *Biochemistry of Nitric-Oxide and Its Redox-Activated Forms*, Science, **258** (1992) 1898.
100. P. Saalfrank, G. Boendgen, K. Finger, and L. Pesce, *Photodesorption of NO from a metal surface: quantum dynamical implications of a two-mode model*, Chem. Phys., **251** (2000) 51.
101. M. Menges, B. Baumeister, K. Alshamery, H.J. Freund, C. Fischer, and P. Andresen, *Dynamical Studies of UV-Laser-Induced NO-Desorption from the Polar NiO(111) Versus the Nonpolar NiO(100) Surfaces*, J. Chem. Phys., **101** (1994) 3318.
102. T. Mull, M. Menges, B. Baumeister, G. Odorfer, H. Geisler, G. Illing, R.M. Jaeger, H. Kuhlenbeck, H.J. Freund, D. Weide, U. Schuller, P. Andresen, F. Budde, P. Ferm, V. Hamza, and G. Ertl, *UV-Laserphotochemistry of Molecules on Solid-Surfaces - NO/Ni(100)-O*, Physica Scripta, **41** (1990) 134.
103. T. Mull, B. Baumeister, M. Menges, H.J. Freund, D. Weide, C. Fischer, and P. Andresen, *Bimodal Velocity Distributions after Ultraviolet-Laser-Induced Desorption of NO from Oxide Surfaces - Experiments and Results of Model-Calculations*, J. Chem. Phys., **96** (1992) 7108.
104. H. Kuhlenbeck, G. Odorfer, R. Jaeger, C. Xu, T. Mull, B. Baumeister, G. Illing, M. Menges, H.J. Freund, D. Weide, P. Andresen, G. Watson, and E.W. Plummer,

Adsorption, Thermal and Photochemical-Reactions of NO on Clean and Oxygen Precovered Ni(100) Surfaces, Vacuum, **41** (1990) 34.

105. J.A. Prybyla, T.F. Heinz, J.A. Misewich, and M.M.T. Loy, *Direct Observation of Rotational Cooling in Thermal-Desorption - NO/Pd(111)*, Surf. Sci., **230** (1990) L173.
106. Z.C. Ying and W. Ho, *Thermoinduced and Photoinduced Reactions of NO on Si(111)7X7.3. Photoreaction Mechanisms*, J. Chem. Phys., **93** (1990) 9089.
107. L.J. Richter, S.A. Buntin, D.S. King, and R.R. Cavanagh, *State Resolved Studies of the Laser-Induced Desorption of NO from Si(111) 7X7 - Low Coverage Results*, J. Chem. Phys., **96** (1992) 2324.
108. M. Carbone, K. Bobrov, G. Comtet, G. Dujardin, and L. Hellner, *Initial stage of NO adsorption on Si(100)-(2 x 1) studied by synchrotron radiation photoemission and photodesorption*, Surf. Sci., **467** (2000) 49.
109. L. Hellner, G. Comtet, M.J. Ramage, K. Bobrov, M. Carbone, and G. Dujardin, *Selective ion photodesorption from NO adsorbed on Si(111)7 x 7 following core excitation*, J. Chem. Phys., **119** (2003) 515.
110. R. Burch, S.T. Daniells, and P. Hu, *The mechanism of N_2O formation via the $(NO)_2$ dimer: A density functional theory study*, J. Chem. Phys., **121** (2004) 2737.
111. W.A. Brown, P. Gardner, and D.A. King, *Very Low Temperature Surface Reaction: N_2O Formation from NO Dimers at 70 to 90 K on Ag(111)*, J. Phys. Chem., **99** (1995) 7065.
112. C.I. Carlisle and D.A. King, *Direct molecular imaging of NO monomers and dimers and a surface reaction on Ag{111}*, J. Phys. Chem. B, **105** (2001) 3886.
113. T. Vondrak, D.J. Burke, and S.R. Meech, *The dynamics and origin of NO photodesorbed from NO/Ag(111)*, Chem. Phys. Lett., **327** (2000) 137.
114. R.J. Behm and C.R. Brundle, *Decomposition of NO on Ag(111) at Low Temperatures*, J. Vac. Sci. Technol. A, **2** (1984) 1040.
115. H.J. Jansch, C. Huang, A. Ludviksson, G. Rocker, J.D. Redding, H. Metiu, and R.M. Martin, *Formation of N_2O from NO Adsorbed on Silver Layers on Ruthenium, Studied by MQS and TDS*, Surf. Sci., **214** (1989) 377.
116. A. Ludviksson, C. Huang, H.J. Jansch, and R.M. Martin, *Isotopic Studies of the Reaction of No on Silver Surfaces*, Surf. Sci., **284** (1993) 328.
117. W.C. Natzle, D. Padowitz, and S.J. Sibener, *Ultraviolet Laser Photodesorption of NO from Condensed Films: Translational and Internal Energy-Distributions*, J. Chem. Phys., **88** (1988) 7975.
118. H. Nakamura and K. Yamashita, *Theoretical study of the photodesorption mechanism of nitric oxide on a Ag(111) surface: A nonequilibrium Green's function approach to hot-electron tunneling*, J. Chem. Phys., **125** (2006) 084708.
119. S.M. Harris, S. Holloway, and G.R. Darling, *Hot Electron Mediated Photodesorption: A Time-Dependent Approach Applied to NO/Pt(111)*, J. Chem. Phys., **102** (1995) 8235.
120. E.A. Wade, J.I. Cline, K.T. Lorenz, C. Hayden, and D.W. Chandler, *Direct measurement of the binding energy of the NO dimer*, J. Chem. Phys., **116** (2002) 4755.
121. J.R. Hetzler, M.P. Casassa, and D.S. King, *Product Energy Correlations in the Dissociation of Overtone Excited No Dimer*, J. Phys. Chem., **95** (1991) 8086.

122. A.B. Potter, V. Dribinski, A.V. Demyanenko, and H. Reisler, *Exit channel dynamics in the ultraviolet photodissociation of the NO dimer: (NO)(2)-> NO(A(2)Sigma(+))+NO(X-2 Pi)*, J. Chem. Phys., **119** (2003) 7197.
123. A.R.W. Mckellar, J.K.G. Watson, and B.J. Howard, *The No Dimer - N-15 Isotopic Infrared-Spectra, Line-Widths, and Force-Field*, Molec. Phys., **86** (1995) 273.
124. G. Vidali, G. Ihm, H.Y. Kim, and M.W. Cole, *Potentials of Physical Adsorption*, Surf. Sci. Rep., **12** (1991) 133.
125. H. Horino, S.W. Liu, A. Hiratsuka, Y. Ohno, and T. Matsushima, *Two directional N_2 desorption in thermal dissociation of N_2O on Pd(110) at low temperatures*, Chem. Phys. Lett., **341** (2001) 419.
126. Y. Ohno, K. Kimura, M. Bi, and T. Matsushima, *The translational energy of desorbing products in NO and N2O decomposition on Pd (110)*, J. Chem. Phys., **110** (1999) 8221.
127. Y.X. Li and M. Bowker, *The adsorption and decomposition of nitrous oxide on Rh(110) and Rh(111)*, Surf. Sci., **348** (1996) 67.
128. M.A. Henderson, J. Szanyi, and C.H.F. Peden, *Conversion of N_2O to N_2 on $TiO_2(110)$*, Catalysis Today, **85** (2003) 251.
129. K. Sawabe and Y. Matsumoto, *Structure of Adsorbed N_2O on a Pt(111) Surface and Photodissociation at 193nm: Effective Formation of Oxygen Adatoms*, Chem. Phys. Lett., **194** (1992) 45.
130. A.L. Schwaner, W. Mahmood, and J.M. White, *The thermal and electron-induced chemistry of N2O/Ag(111)*, Surf. Sci., **351** (1996) 228.
131. J. Kiss, D. Lennon, S.K. Jo, and J.M. White, *Photoinduced Dissociation and Desorption of N_2O on a Pt(111) Surface*, J. Phys. Chem., **95** (1991) 8054.
132. K. Sawabe and Y. Matsumoto, *Laser Induced Photochemistry of Nitrous Oxide on a Pt(111) Surface*, Surf. Sci., **283** (1993) 126.
133. Y. Matsumoto, J.W. Lee, H. Kato, and K. Sawabe, *Dynamics of Photochemical Processes of N_2O Adsorbed on Metal and Semiconductor Surfaces*, Laser Techniques for Surface Science, **2125** (1994) 303.
134. H. Kato, J. Lee, K. Sawabe, and Y. Matsumoto, *Photochemistry of N2O on Si(100), surface photo-oxidation*, Surf. Sci., **445** (2000) 209.
135. H. Kato, J. Lee, K. Sawabe, and Y. Matsumoto, *Adsorption-state specific photodissociation dynamics of N2O on Si(100)*, Surf. Sci., **386** (1997) 93.
136. H. Kato, K. Sawabe, and Y. Matsumoto, *Adsorbed states and thermal reactions of N2O on Si(100) below room temperature: Desorption induced by dissociation*, Surf. Sci., **351** (1996) 43.
137. J. Lee, H. Kato, K. Sawabe, and Y. Matsumoto, *Angular-Distributions of N-2 in the Photodissociation of N2O Adsorbed on a Partially Oxidized Si(100) Surface at 95 K*, Chem. Phys. Lett., **240** (1995) 417.
138. H. Horino, S.W. Liu, M. Sano, S. Wako, A. Hiratsuka, Y. Ohno, I. Kobal, and T. Matsushima, *Ad-molecule orientation and thermo- and photo-induced surface-aligned desorption*, Topics in Catalysis, **18** (2002) 21.
139. M. Zelikoff, K. Watanabe, and E.C.Y. Inn, *Absorption Coefficients of Gases in the Vacuum Ultraviolet.2. Nitrous Oxide*, J. Chem. Phys., **21** (1953) 1643.

140. Y. Matsumoto, *Photochemistry and photo-induced ultrafast dynamics at metal surfaces*, Bulletin of the Chemical Society of Japan, **80** (2007) 842.
141. A. Brown, P. Jimeno, and G.G. Balint-Kurti, *Photodissociation of N_2O. I. Ab initio potential energy-surfaces for the low-lying electronic states $X^1 A'$, $2\,^1A'$, and $1\,^1A''$*, J. Phys. Chem. A, **103** (1999) 11089.
142. S.D. Peyerimhoff and R.J. Buenker, *Theoretical Study of the Geometry and Spectrum of Nitrous Oxide*, J. Chem. Phys., **49** (1968) 2473.
143. M.N. Daud, G.G. Balint-Kurti, and A. Brown, *Ab initio potential energy surfaces, total absorption cross sections, and product quantum state distributions for the low-lying electronic states of N2O*, J. Chem. Phys., **122** (2005) 054305.
144. A. Demeijere, H. Hirayama, and E. Hasselbrink, *Adsorbate Structure and Angular-Dependence of Desorption Dynamics - O2 Photodesorbed from Pd(111)*, Phys. Rev. Lett., **70** (1993) 1147.
145. D.P. Masson, E.J. Lanzendorf, and A.C. Kummel, *Photoinduced Ejection of Ballistic Oxygen-Atoms from N_2O Adsorbed on Pt(111)*, Phys. Rev. Lett., **74** (1995) 1799.
146. N.R. Avery, *An Eels Study of N2O Adsorption on Pt(111)*, Surf. Sci., **131** (1983) 501.
147. M. Dehghani, M. Afshari, Z. Abusara, N. Moazzen-Ahmadi, and A.R.W. McKellar, *Nitrous oxide dimer: Observation of a new polar isomer*, J. Chem. Phys., **126** (2007) 164310.
148. K. Watanabe, A. Kokalj, Y. Inokuchi, I. Rzeznicka, K. Ohshimo, N. Nishi, and T. Matsushima, *Orientation of nitrous oxide on palladium(110) by STM*, Chem. Phys. Lett., **406** (2005) 474.
149. K. Watanabe, A. Kokalj, H. Horino, I.I. Rzeznicka, K. Takahashi, N. Nishi, and T. Matsushima, *Scanning-tunneling microscopy, near-edge X-ray-absorption fine structure, and density-functional theory studies of N_2O orientation on Pd(110)*, Japanese Journal of Applied Physics Part 1-Regular Papers Brief Communications & Review Papers, **45** (2006) 2290.
150. Y. Matsumoto, K. Sawabe, and J. Lee, *Photochemistry and Photodissociation Dynamics of N_2O on Metal-Surfaces*, Laser Techniques for State-Selected and State-to-State Chemistry, **1858** (1993) 378.
151. R.M. Rao, R.J. Beuhler, and M.G. White, *Nonthermal photodesorption of N_2 from Ag(111)*, J. Chem. Phys., **109** (1998) 8016.
152. J.E. Demuth, D. Schmeisser, and P. Avouris, *Resonance Scattering of Electrons from N_2, CO, O_2, and H_2 Adsorbed on a Silver Surface*, Phys. Rev. Lett., **47** (1981) 1166.
153. P.J. Rous, *Negative-Ion Formation in Adsorbed Molecules - the Role of Surface-States*, Phys. Rev. Lett., **74** (1995) 1835.
154. A.D. McFarland and R.P. Van Duyne, *Single silver nanoparticles as real-time optical sensors with zeptomole sensitivity*, Nano Letters, **3** (2003) 1057.
155. A. Wokaun, J.P. Gordon, and P.F. Liao, *Radiation Damping in Surface-Enhanced Raman-Scattering*, Phys. Rev. Lett., **48** (1982) 957.
156. A. Wokaun, P.F. Liao, and J.P. Gordon, *Particle Dipolar Interactions in Surface-Enhanced Electromagnetic Effects*, Journal of the Optical Society of America, **71** (1981) 1552.

157. P.F. Liao, J.G. Bergman, D.S. Chemla, A. Wokaun, J. Melngailis, A.M. Hawryluk, and N.P. Economou, *Surface-Enhanced Raman-Scattering from Microlithographic Silver Particle Surfaces*, Chem. Phys. Lett., **82** (1981) 355.
158. K. Kneipp, Y. Wang, H. Kneipp, L.T. Perelman, I. Itzkan, R. Dasari, and M.S. Feld, *Single molecule detection using surface-enhanced Raman scattering (SERS)*, Phys. Rev. Lett., **78** (1997) 1667.
159. N. Felidj, J. Aubard, G. Levi, J.R. Krenn, A. Hohenau, G. Schider, A. Leitner, and F.R. Aussenegg, *Optimized surface-enhanced Raman scattering on gold nanoparticle arrays*, Appl. Phys. Lett., **82** (2003) 3095.
160. N. Felidj, J. Grand, G. Laurent, J. Aubard, G. Levi, A. Hohenau, N. Galler, F.R. Aussenegg, and J.R. Krenn, *Multipolar surface plasmon peaks on gold nanotriangles*, J. Chem. Phys., **128** (2008).
161. N. Felidj, S.L. Truong, J. Aubard, G. Levi, J.R. Krenn, A. Hohenau, A. Leitner, and F.R. Aussenegg, *Gold particle interaction in regular arrays probed by surface enhanced Raman scattering*, J. Chem. Phys., **120** (2004) 7141.
162. G. Laurent, N. Felidj, J. Aubard, G. Levi, J.R. Krenn, A. Hohenau, G. Schider, A. Leitner, and F.R. Aussenegg, *Surface enhanced Raman scattering arising from multipolar plasmon excitation*, J. Chem. Phys., **122** (2005).
163. J.B. Jackson, S.L. Westcott, L.R. Hirsch, J.L. West, and N.J. Halas, *Controlling the surface enhanced Raman effect via the nanoshell geometry*, Appl. Phys. Lett., **82** (2003) 257.
164. I.H. El-Sayed, X.H. Huang, and M.A. El-Sayed, *Surface plasmon resonance scattering and absorption of anti-EGFR antibody conjugated gold nanoparticles in cancer diagnostics: Applications in oral cancer*, Nano Letters, **5** (2005) 829.
165. H. Ditlbacher, A. Hohenau, D. Wagner, U. Kreibig, M. Rogers, F. Hofer, F.R. Aussenegg, and J.R. Krenn, *Silver nanowires as surface plasmon resonators*, Phys. Rev. Lett., **95** (2005) 257403.
166. S. Kwiet, D.E. Starr, A. Grujic, M. Wolf, and A. Hotzel, *Femtosecond laser induced desorption of water from silver nanoparticles*, Appl. Phys. B, **80** (2005) 115.
167. R.T. Kidd, D. Lennon, and S.R. Meech, *Surface plasmon enhanced substrate mediated photochemistry on roughened silver*, J. Chem. Phys., **113** (2000) 8276.
168. D.J. Burke, T. Vondrak, and S.R. Meech, *Photodesorption and photochemical dynamics on roughened silver: Sulphur dioxide and carbonyl sulphide*, Surf. Sci., **585** (2005) 123.
169. Z.J. Sun, S. Gravelle, R.S. Mackay, X.Y. Zhu, and J.M. White, *Hot Carrier Induced Photodesorption Dynamics of SO_2 from Ag(111)*, J. Chem. Phys., **99** (1993) 10021.
170. D. Mulugeta, K.H. Kim, K. Watanabe, D. Menzel, and H.J. Freund, *Size effects in thermal and photochemistry of $(NO)_2$ on Ag nanoparticles*, Phys. Rev. Lett., **101** (2008) 146103.
171. M. Bauer and M. Aeschlimann, *Dynamics of excited electrons in metals, thin films and nanostructures*, J. Electron Spectrosc. Relat. Phenom., **124** (2002) 225.
172. D.R. Lide, *CRC handbook of chemistry and physics*, 2008, Boca Raton; London; New York: Taylor and Francis Group.

173. R. Monreal and S.P. Apell, *Electromagnetic-Field-Enhanced Desorption of Atoms*, Phys. Rev. B, **41** (1990) 7852.
174. F. Budde, T.F. Heinz, M.M.T. Loy, J.A. Misewich, F. Derougemont, and H. Zacharias, *Femtosecond Time-Resolved Measurement of Desorption*, Phys. Rev. Lett., **66** (1991) 3024.
175. F.J. Kao, D.G. Busch, D. Cohen, D.G. Dacosta, and W. Ho, *Femtosecond Laser-Desorption of Molecularly Adsorbed Oxygen from Pt(111)*, Phys. Rev. Lett., **71** (1993) 2094.
176. D.G. Busch, S.W. Gao, R.A. Pelak, M.F. Booth, and W. Ho, *Femtosecond Desorption Dynamics Probed by Time-Resolved Velocity-Measurements*, Phys. Rev. Lett., **75** (1995) 673.
177. L. Cai, X.D. Xiao, and M.M.T. Loy, *Femtosecond laser desorption of CO from the Pt(111) surface*, Surf. Sci., **464** (2000) L727.
178. D.N. Denzler, C. Frischkorn, M. Wolf, and G. Ertl, *Surface femtochemistry: Associative desorption of hydrogen from Ru(001) induced by electronic excitations*, J. Phys. Chem. B, **108** (2004) 14503.
179. P. Szymanski, A.L. Harris, and N. Camillone, *Adsorption-state-dependent subpicosecond photoinduced desorption dynamics*, J. Chem. Phys., **126** (2007) 214709.
180. M. Bonn, S. Funk, C. Hess, D.N. Denzler, C. Stampfl, M. Scheffler, M. Wolf, and G. Ertl, *Phonon- versus electron-mediated desorption and oxidation of CO on Ru(0001)*, Science, **285** (1999) 1042.
181. S. Funk, M. Bonn, D.N. Denzler, C. Hess, M. Wolf, and G. Ertl, *Desorption of CO from Ru(001) induced by near-infrared femtosecond laser pulses*, J. Chem. Phys., **112** (2000) 9888.
182. M. Nest and P. Saalfrank, *Enhancement of femtosecond-laser-induced molecular desorption by thin metal films*, Phys. Rev. B, **69** (2004) 235405.
183. P. Muhlschlegel, H.J. Eisler, O.J.F. Martin, B. Hecht, and D.W. Pohl, *Resonant optical antennas*, Science, **308** (2005) 1607.
184. E. Cubukcu, E.A. Kort, K.B. Crozier, and F. Capasso, *Plasmonic laser antenna*, Appl. Phys. Lett., **89** (2006) 093120.
185. http://www.angstec.com.
186. B. Bourguignon, S. Carrez, M. Buchner, and C.R. Henry, *Laser desorption of C-contaminated Pd clusters grown on MgO(100)*, Chem. Phys. Lett., **287** (1998) 40.
187. A. Gloskovskii, D.A. Valdaitsev, M. Cinchetti, S.A. Nepijko, J. Lange, M. Aeschlimann, M. Bauer, M. Klimenkov, L.V. Viduta, P.M. Tomchuk, and G. Schonhense, *Electron emission from films of Ag and Au nanoparticles excited by a femtosecond pump-probe laser*, Phys. Rev. B, **77** (2008) 195427.
188. F.M. Zimmermann and W. Ho, *Rotational and Spin-Orbit Distributions of Photochemically Desorbed Molecules*, Phys. Rev. Lett., **72** (1994) 1295.
189. T. Yamanaka, A. Hellman, S.W. Gao, and W. Ho, *State-resolved femtosecond two-pulse correlation measurements of NO photodesorption from Pt(111)*, Surf. Sci., **514** (2002) 404.
190. M. Lisowski, P.A. Loukakos, U. Bovensiepen, J. Stahler, C. Gahl, and M. Wolf, *Ultra-fast dynamics of electron thermalization, cooling and transport effects in Ru(001)*, Appl. Phys. A, **78** (2004) 165.

191. B. Rethfeld, A. Kaiser, M. Vicanek, and G. Simon, *Ultrafast dynamics of nonequilibrium electrons in metals under femtosecond laser irradiation*, Phys. Rev. B, **65** (2002) 214303.
192. W. Brenig, Y. Chiba, and R. Brako, *Molecular Vibration Dynamics in Scattering of NO/Ag*, Langmuir, **7** (1991) 2504.
193. J. Hohlfeld, S.S. Wellershoff, J. Gudde, U. Conrad, V. Jahnke, and E. Matthias, *Electron and lattice dynamics following optical excitation of metals*, Chem. Phys., **251** (2000) 237.
194. M. Merschdorf, W. Pfeiffer, S. Voll, and G. Gerber, *Electron gas cooling in Ag nanoparticles on graphite*, Phys. Rev. B, **68** (2003) 155416.
195. V.P. Zhdanov and B. Kasemo, *Specifics of substrate-mediated photo-induced chemical processes on supported nm-sized metal particles*, Journal of Physics-Condensed Matter, **16** (2004) 7131.
196. R.T. Kidd, S.R. Meech, and D. Lennon, *Enhanced photodesorption of NO on roughened silver surfaces*, Chem. Phys. Lett., **262** (1996) 142.
197. K. Wettergren, B. Kasemo, and D. Chakarov, *Photodesorption of NO from graphite(0001) surface mediated by silver clusters*, Surf. Sci., **593** (2005) 235.
198. W. Hoheisel, K. Jungmann, M. Vollmer, R. Weidenauer, and F. Trager, *Desorption Stimulated by Laser-Induced Surface-Plasmon Excitation*, Phys. Rev. Lett., **60** (1988) 1649.
199. J. Bosbach, C. Hendrich, F. Stietz, T. Vartanyan, and F. Trager, *Ultrafast dephasing of surface plasmon excitation in silver nanoparticles: Influence of particle size, shape, and chemical surrounding*, Phys. Rev. Lett., **89** (2002) 257404.
200. F. Stietz, *Laser manipulation of the size and shape of supported nanoparticles*, Appl. Phys. A, **72** (2001) 381.
201. J. Bosbach, D. Martin, F. Stietz, T. Wenzel, and F. Trager, *Laser-based method for fabricating monodisperse metallic nanoparticles*, Appl. Phys. Lett., **74** (1999) 2605.
202. C.M. Wong, J.D. McNeill, K.J. Gaffney, N.H. Ge, A.D. Miller, S.H. Liu, and C.B. Harris, *Femtosecond studies of electron dynamics at dielectric-metal interfaces*, J. Phys. Chem. B, **103** (1999) 282.
203. N. Schwentner, F.J. Himpsel, V. Saile, M. Skibowski, W. Steinmann, and E.E. Koch, *Photoemission from Rare-Gas Solids - Electron-Energy Distributions from Valence Bands*, Phys. Rev. Lett., **34** (1975) 528.
204. R.B. Hall, *Pulsed-Laser-Induced Desorption Studies of the Kinetics of Surface-Reactions*, J. Phys. Chem., **91** (1987) 1007.
205. H.G. Schuster, *Deterministic chaos: an introduction*, 1984, Weinheim: Physik-Verlag.
206. N.U. Zhanpeisov, G. Martra, W.S. Ju, M. Matsuoka, S. Coluccia, and M. Anpo, *Interaction of N2O with Ag^+ ion-exchanged zeolites: an FT-IR spectroscopy and quantum chemical ab initio and DFT studies*, J. Mol. Catal. a-Chem., **201** (2003) 237.
207. M.I. Stockman, L.N. Pandey, L.S. Muratov, and T.F. George, *Giant Fluctuations of Local Optical-Fields in Fractal Clusters*, Phys. Rev. Lett., **72** (1994) 2486.

208. M.I. Stockman, S.V. Faleev, and D.J. Bergman, *Localization versus delocalization of surface plasmons in nanosystems: Can one state have both characteristics?* Phys. Rev. Lett., **87** (2001) 167401.
209. M.I. Stockman, S.V. Faleev, and D.J. Bergman, *Coherent control of femtosecond energy localization in nanosystems*, Phys. Rev. Lett., **88** (2002) 067402.
210. M.I. Stockman, *Femtosecond optical responses of disordered clusters, composites, and rough surfaces: "The ninth wave" effect*, Phys. Rev. Lett., **84** (2000) 1011.
211. D.J. Bergman and M.I. Stockman, *Surface plasmon amplification by stimulated emission of radiation: Quantum generation of coherent surface plasmons in nanosystems*, Phys. Rev. Lett., **90** (2003) 027402.
212. R.H. Ritchie, J.R. Manson, and P.M. Echenique, *Surface-Plasmon-Ion Interaction in Laser-Ablation of Ions from a Surface*, Phys. Rev. B, **49** (1994) 2963.
213. M.J. Shea and R.N. Compton, *Surface-Plasmon Ejection of Ag^+ Ions from Laser Irradiation of a Roughened Silver Surface*, Phys. Rev. B, **47** (1993) 9967.
214. E. Zaremba and W. Kohn, *Vanderwaals Interaction between an Atom and a Solid-Surface*, Phys. Rev. B, **13** (1976) 2270.
215. G.G. Cardini, S.F. Oshea, M. Marchese, and M.L. Klein, *Dispersion of Surface Phonons in Xenon Overlayers Physisorbed on the Ag(111) Surface*, Phys. Rev. B, **32** (1985) 4261.
216. G. Ihm, M.W. Cole, F. Toigo, and G. Scoles, *Systematic Trends in Vanderwaals Interactions - Atom Atom and Atom Surface Cases*, J. Chem. Phys., **87** (1987) 3995.
217. B.N.J. Persson, *Sliding friction: physical principles and applications*, 2000, Berlin; New York: Springer.

Deutsche Kurzfassung

In dieser Arbeit wurden durch Nano- und Femtosekunden-Laserpulse hervorgerufene thermische und photo-induzierte Prozesse auf Ag(111) und geträgerten Ag-Nanopartikeln (NPs) mit Hilfe von thermischer Desorptionsspektroskopie (TPD), Masse-selektierter photoinduzierter Desorption (PID) und Flugzeit-Messungen (TOF) untersucht. Die geträgerten Ag NPs wurden durch Deponierung von Ag-Atomen auf einem Al_2O_3/NiAl(110)-Substrat gebildet.

Die photoinduzierte Reaktions- und Desorptionsdynamik von einzelnen NO-Spezies wurde durch Kontrolle der jeweiligen Adsorptionszustände selektiv untersucht. In dieser Arbeit wurde zum ersten Mal die direkte photochemische Bildung von N_2 und N_2O aus NO-Dimeren auf Ag(111) bei Photonenenergien $\geq$ 2.3 eV beobachtet. Das gebildete N_2 weist eine hohe Translationsenergie auf welche durch starke Abstoßung von der Oberfläche verursacht wird. Um den Bildungsmechanismus von N_2 aufzuklären wurde die Abhängigkeit des Adsorptionszustands von N_2O auf Ag(111) in Bezug auf Einfallswinkel, Polarisation und Photonenenergie untersucht. Es zeigte sich, daß N_2O selbst eine besondere Photodesorptionsdynamik aufweist. Diese Ergebnisse führen zur Schlußfolgerung, daß N_2 durch das gleichzeitige Brechen von zwei N-O – Bindungen gefolgt von der Bildung einer N-N – Dreifachbindung erzeugt wird. Dies kann als gleichzeitige Abstraktion des N-Atoms der Nitrosyl-Gruppen eines $(NO)_2$-Dimers aufgefaßt werden.

Die für Ag(111) erhaltenen Ergebnisse wurden mit den thermischen und photoinduzierten Reaktionen von NO auf Ag NPs verglichen, wobei der gleiche experimentelle Aufbau sowie die gleichen Methoden eingesetzt wurden. Bei Bestrahlung mit Nanosekunden-Laserpulsen konnte eine Erhöhung der Photodesorptionsausbeute für NO auf Ag NPs bei verschiedenen Energien, einschließlich der Resonanzenergie des (1,0)-Plasmons, festgestellt werden. Eine weitere starke Erhöhung der Photodesorptionsausbeute von Ag NPs tritt bei Verwendung von Femtosekunden-Laserpulsen auf. Im Gegensatz dazu bleibt die Photodesorptionsausbeute von Ag(111) nahzu unverändert. Die beobachtete Erhöhung wird im Rahmen von räumlichen Beschränkungseffekten, Plasmonenanregung, und Desorptionsmodellen, wobei die berechnete Anzahl von heißen Elektronen und Desorbaten einbezogen wurde, diskutiert.

Eine einzigartige, mit hyperthermaler Energie und chaotischer Zeitabhängigkeit auftretende Photodesorption von auf Ag NPs adsorbierten Xe-Schichten wurde bei Bestrahlung mit Nanosekunden-Laserpulsen im Resonanzenergiebereichs des (1,0) Mie-Plasmons beobachtet. Das chaotische Verhalten kommt vermutlich durch die Kopplung der Plasmonenfelder von geeignet verteilten Ag NPs zustande. Um diese Ergebnisse zu

erklären wurde angenommen, daß die Desorption durch direkte Energieübertragung auf das Adsorbat aufgrund der Pauli-Abstoßung der kollektiv oszillierenden Oberflächenplasmonen hervorgerufen wird. Eine einfache Modellrechnung zeigt, daß dies möglich sein kann.

Curriculum Vitae

The curriculum vitae is omitted in this online version due to data privacy.

Publications

- Ki Hyun Kim, Kazuo Watanabe, Dietrich Menzel, Hans-Joachim Freund, *Photoinduced Abstraction Resctions within NO Dimers on Ag(111)*, J. Am. Chem. Soc., **131**, (2009) 1660.
- Daniel Mulugeta, Ki Hyun Kim, Kazuo Watanabe, Dietrich Menzel, Hans-Joachim Freund, *Size Effects in Thermal and Photochemistry of $(NO)_2$ on Ag Nanoparticles*, Phys. Rev. Lett. **101**, (2008) 146103.
- Kazuo Watanabe, Ki Hyun Kim, Dietrich Menzel, Hans-Joachim Freund, *Hyperthermal Chaotic Photodesorption of Xenon from Alumina Supported Silver Nanoparticles: Plasmonic Coupling and Plasmon-Induced Desorption*, Phys. Rev. Lett. **99**, (2007) 225501.

In Preparation

- Ki Hyun Kim, Kazuo Watanabe, Dietrich Menzel, Hans-Joachim Freund, *Thermal- and photoreactions of NO on Ag(111).*
- Ki Hyun Kim, Kazuo Watanabe, Dietrich Menzel, Hans-Joachim Freund, *Dynamics and excitation mechanisms of N_2O and N_2 photodesorbed from N_2O on Ag(111).*
- Ki Hyun Kim, Kazuo Watanabe, Dietrich Menzel, Hans-Joachim Freund, *Enhancement of photoreactions of NO on supported Ag nanoparticles compared to Ag(111).*
- Ki Hyun Kim, Kazuo Watanabe, Dietrich Menzel, Hans-Joachim Freund, *Femtosecond laser induced desorption of NO on supported Ag nanoparticles.*

Earlier Publications

- Ki Hyun Kim, Eun Ju Kim, Sang Jo Lee, Jung Hoon Lee, Chong Hoon Kwak, Jeong Eun Kim, *Effects of applied electric field on orientational photorefraction in porphyrin:Zn-doped nematic liquid crystals*, Appl. Phys. Lett., **85**, (2004) 366.
- Jung Hoon Lee, Gee Young Sung, Sang Jo Lee, Ki Hyun Kim, Young Gul Joh, Chong Hoon Kwak, Jae Bong Song, and Yun Woo Lee, *Fabrication of bifocal holographic lenses by holographic polymer dispersed liquid crystal film*, J. Opt. Soc. Korea (Korean edition), **14**, (2003) 109.
- Mi Ra Kim, Phan Seok Kim, Gee Young Sung, Ki Hyun Kim, Chong Hoon Kwak, Chang Sik Ha, Jin Kook Lee, *Effects of chemical structure of diisocyanate in*

polyurethanes on the diffraction efficiency, Optical Materials **21**, (2002) 385.

- Mi Ra Kim, Phan Seok Kim, Hooi Sung Kim, Gee Young Sung, Ki Hyun Kim, Chang Sik Ha, Chong Hoon Kwak, and Jin-Kook Lee, *Syntheses and Optical Properties of Polyesters with Disperse Red 19 by the Polycondensation Reaction*, Mol. Cryst. Liq. Cryst., **377**, (2002) 293.
- Phan Seok Kim, Mi-Ra Kim, Gee Young Sung, Ki Hyun Kim, Chang Sik Ha, Chong Hoon Kwak, and Jin Kook Lee, *Synthesis and Photorefractive Property of a Polymer Containing Azobenzene Group in the Side Chain*, Mol. Cryst. Liq. Cryst., **377**, (2002) 277.

Acknowledgements

It is my utmost pleasure to acknowledge the people who have supported, encouraged, and helped me in my journey toward my PhD. Special thanks are given to the following:

- Prof. Dr. Hans-Joachim Freund, for providing the guidance and opportunity to join his group. I would like to express my great respect and esteem for his wide knowledge, wisdom, and kindness.
- Dr. Kazuo Watanabe, for giving his advice and guidance to achieve this thesis work. The invaluable support of his experience, very important comments and suggestions, and kindness will never be forgotten.
- Prof. Dr. Dietrich Menzel, for his guidance, enlightening discussions, many inspiring ideas. I deeply express my great respect and esteem for his wide scientific knowledge and wisdom, and also kindness.
- Prof. Dr. Martin Wolf, for co-supervising this thesis and for supporting and encouraging me. Also I am grateful to his former and present group members for fruitful discussions and providing their theoretical code for two temperature model, especially Dr. Uwe Bovensiepen, Dr. Christian Frischkorn, Dr. Anne Julia Stähler, Dr. Patrick Kirchmann, Juraj Bdzoch.
- International Max Planck Research School (IMPRS) for the financial support. And all its former and present members, particularly, Dr. Thomas Risse and Mrs. Bettina Menzel, for organizing helpful block courses and soft skill seminars.
- Walter Wachsmann and Klaus Peter Vogelgesang, for his kindness and technical support.
- Dr. Niklas Nilius, for providing his excellent STM results. Also one of his former group members, Dr. Hadj Mohamed Benia, for extensive discussion about plasmon.
- Dr. Martin Sterrer, for fruitful discussions and comments as well as translating my English abstract to German.
- Daniel Mulugeta, for productive collaboration.
- Mrs. Gabriele Mehnert and Mrs. Manuela Misch, for their kindness and help.
- Dr. Nicola Scott and Dr. Heather Abbott, for their helpful comments.
- Dr. Esther Carrasco Burgos, Dr. Zhihui Qin, and Andreas Aumer for their friendliness.

Lastly, I would like to express my gratitude to my wife and sons, to my friends, especially, Helmut Brungsbach, and to my parents.